Neotectonics and Paleoseismology of the North Frontal Thrust System, southern California

Kevin B. Anderson
Master's Thesis – Defended August 8, 2002
Dept. of Geological Sciences, Virginia Tech
Advisor: Dr. James Spotila
Committee Members: Dr. Martin Chapman, Dr. John Hole, Dr. Richard Law

Neotectonics and Paleoseismology of the North Frontal Thrust System, southern California

Kevin B. Anderson

Abstract

Seismic hazard assessment of intersecting fault systems, such as the strike-slip and reverse faults of the Los Angeles basin, is hindered by complex patterns of rupture that are currently difficult to predict. To improve this understanding, constraints on the previous rupture patterns of such systems are needed. The junction between the Transverse Ranges and the Eastern California shear zone in southern California provides a natural analog to the seismic setting of the Los Angeles basin. Along the northern flank of the San Bernardino Mountains, the east-west trending North Frontal thrust system is intersected by several northwest trending dextral faults of known Holocene and historical rupture activity. This structural setting, along with an apparent decay in uplift rate along the thrust (from a 3-Myr average of 0.5 mm/yr to a late Pleistocene rate estimated as slow as 0.05 mm/yr), suggests the thrust system may have been rendered inactive by the shear zone that dissects it. However, a clear cross-cutting relationship does not exist, raising the possibility that the two systems are coactive.

To test this, we have constrained the recent rupture history of one thrust fault segment with paleoseismic investigations. We have excavated an apparently young thrust fault scarp along the central portion of the thrust system, chosen as the most likely

to have ruptured in the recent past. At this location, just west of the intersection of the Helendale fault, a 7-m-high thrust scarp in older fanglomerate is dissected and replaced by younger alluvium with a 1.5-m-high scarp. An excavation across the smaller scarp revealed a 3-m-thick sequence of coarse alluvium cut by a shallow, south-dipping thrust fault with 1.65 m of throw. The simple, smooth trace of the fault plane and the lack of evidence for repeated deformation suggest the offset was produced by one event. A maximum age for this event is provided by disagregated detrital charcoal sampled from a sand lens in the lowermost gravel of the hangingwall, which yielded a calibrated radiocarbon age of 9220 BC (11220 yr BP). Subsequent to this inferred depositional age, an additional 2-m of gravel was deposited prior to fault rupture. Although a minimum age is not constrained, the event may thus have been as young as mid- to late-Holocene, consistent with the poor degree of soil development in several buried soil horizons in the alluvium. This indicates that at least part of the thrust system is coactive with the strike-slip strands that intersect it and implies that such intersections do not require either fault system to be extinct.

However, it is crucial to obtain a minimum age in order to constrain the recent rupture history. This is inherently difficult because where the required onlapping relationships are present, scarps associated with the most recent event have been buried or eroded. A second site does occur several km from our original site, yet without knowing the exact location or depth of the fault an excavation would be risky. To increase the likelihood of finding the fault with an excavation, we employed geophysical exploration techniques to image the fault at depth. Ground Penetrating Radar (GPR) is a technique that can be used for shallow high-resolution imaging by recording the

propagation of radio waves. To calibrate this technique to locating a shallow fault in the conditions of the study area, we returned to the site of our original excavation. We observed reflections from subhorizontal strata and the fault plane extending to a depth ~10 meters. This was identical to our initial trench observations. Using the same technique at our candidate minimum-age site, we resolved the exact location of a dipping fault plane covered by several meters of young alluvium. Now that the fault has been located, excavation of the site can be undertaken with a good chance of success. This result shows the value of GPR being used as an innovative predictive tool in paleoseismology.

Acknowledgments

Foremost, I wish to thank my wife for unlimited support during my college career and beyond. I also wish to thank my family for years of love and support. I wish to thank Dr. James Spotila for advisement and friendship throughout this project. I wish to thank Dr. John Hole for his invaluable knowledge and field assistance with ground-penetrating radar. I would like to express my appreciation to Jamie Buscher for field assistance and I would like to thank the entire active tectonics and geomorphology group (Greg Bank, Rebecca Kavage, Jamie Buscher, and Jim Spotila) for friendship, support, and invaluable discussions. Thanks also go to Dr. Richard Law of Virginia Tech and Dr. Martin Chapman of Virginia Tech for advisement. I also express my appreciation to Mitsubishi Cement Corporation, Specialty Minerals, and Harry Abdul for access and local knowledge pertaining to the study area.

Funding

This project was funded by a National Earthquake Hazards Reduction Program Grant from the United States Geological Survey.

Table of Contents

Chapter 1: Introduction

1.1 The Problem

Complexly associated faults represent a major hindrance in our ability to assess seismic hazards. Faults of different orientations and/or slip mechanisms often occur in close proximity or even intersect, particularly within deforming continents (Jackson, 1999; England and Jackson, 1989). In some cases, faults intersect and join in manners that fit the criteria of Anderson (1951) faulting. For example, conjugate faults or tear faults may be produced by localized motion on an adjacent fault strand. Yet, in rare cases, fault systems are spatially related in a way that appears to violate basic rules of Coulomb faulting. For example, non-conjugate fault systems of different slip mechanisms that are driven by far-field plate motions and which require different stress regimes can intersect (Barka and Kadinsky-Cade, 1988). This may lead to an interpretation in which one fault system preceded the other and has been rendered inactive as the other system developed. Polyphase deformation is even invoked in the absence of geologic data. Such ambiguity can lead to an inability to understand and forecast rupture patterns. In such cases, the rupture history and magnitude of activity must be constrained for both fault systems, before the mechanisms of fault interaction can be understood.

To illustrate the potential seismic hazard associated with the interaction of two intersecting fault systems, it is useful to explore possible scenarios of rupture. Segment boundaries including discontinuities in surficial traces and intersecting fault systems have been studied extensively to determine their role in association with earthquake magnitude (Rubin, 1996; Barka and Kadinsky-Cade, 1988). Figure 1 demonstrates four hypothetical

end-member rupture scenarios. First, strike-slip faults may behave as segment boundaries, effectively limiting the length (and hence the magnitude) of a thrust event. Another possible scenario is mechanical coupling of the systems. Rupture of one fault may trigger the rupture of an adjacent or connected strand of the other fault system, making short-term prediction of rupture patterns dependent on the faults' interaction. A third scenario involves rupture of one entire fault, independent of the other (i.e. decoupled). Finally, one fault system could be extinct and predate the other, cross cutting the fault system. Earthquake size is thus linked to how faults interact, but previous examples are insufficient to guide adequate earthquake forecasts. We cannot know the future rupture patterns based on mapped fault patterns alone. Complete and accurate histories of the opposing systems and all segments must be constrained and compared to determine the intersecting relationship. A combination of the idealized scenarios or a transition from one scenario to another may be observed, for although the first three scenarios are all possible, they are metastable and will rapidly evolve into last scenario. Through detailed study of active fault systems, we may further determine how complex fault systems interact and what rupture pattern scenarios may be possible.

The Los Angeles Basin provides an example of how it is difficult to forecast rupture patterns of intersecting fault complexes. Dolan et al. (1995) explored hypothetical rupture scenarios for well known faults, to assess the relative possibilities of large, rare events versus more frequent earthquakes on smaller rupture segments (Figure 2). Major thrust faults, such as the Sierra Madre-Cucamonga fault, are intersected or abutted by strike-slip faults including the Newport-Inglewood, the Palos Verdes, and the Whittier-Elsinore fault systems. However, the Los Angeles Basin is unfortunately not

ideal for a study of intersecting faults. The empirical history of fault rupture activity that is required to determine how intersecting fault systems interact is too elusive there. Many faults are blind, such that sedimentary layers with datable material young enough to constrain rupture events are not offset (Shaw and Shearer, 1999). Much of the geomorphic record of recent faulting has also been anthropogenically altered. An analog for this structural setting is thus required to better understand intersecting faults. The confluence of the Eastern California shear zone (ECSZ) and the North Frontal Thrust system (NFTS) of the Transverse Ranges to the east of the San Andreas fault (SAF) is tectonically similar and represents a valuable source of information for understanding fault behavior (Figure 3). The NFTS is segmented by individual dextral strands of the shear zone, but its rupture history is unknown (Figure 4). We focus on this structure to develop an improved understanding of the hazard associated with such complex fault systems.

1.2 Geologic Setting

The union of the ECSZ and the Transverse Ranges in the San Bernardino Mountains is an excellent setting to explore the problem of intersecting faults. The NFTS and dextral faults intersect in a seemingly non-intuitive way with both systems remaining intact the full extent their traces with no apparent crosscutting relationships. This promises that they will provide an important lesson for fault behavior if both are active. The NFTS is represented at the surface by morphologically sharp scarps with little anthropogenic alteration, yet there is no historical or paleoseismic record of activity.

Constraining the rupture history on the NFTS could thus provide a unique opportunity to quantify the relationship between two independent intersecting fault systems.

The ECSZ is a broad series of discontinuous en echelon dextral faults that run nearly parallel to the relative motion vector between the Pacific and North America plates (Dokka and Travis, 1990; Savage et al., 1990). It consists of a dozen or so faults in parallel series that extend across ~100 km width of the central and western Mojave Desert (Figure 5). The shear zone stretches from the restraining bend in the SAF at San Gorgonio Pass, through the Mojave Desert along the Big Bend in the SAF, and northwards through the Owens Valley along the western Basin and Range for >1000 km. It has sustained as much as 65-80 km of total slip since its initiation in the middle Miocene (Dokka and Travis, 1990). This accounts for 9-14% of the total right-lateral shear (635 $\pm$ 70 km) accommodated between the North American and Pacific plate boundary in this period (Stock and Molnar, 1988; Dokka and Travis, 1990). Geologic and geodetic estimates of recent slip rates for the ECSZ range from 8 to 12 mm/yr (Savage et al., 1990; Sauber et al., 1994; WGCEP, 1995). Paleoseismic investigations on individual fault strands, such as Johnson Valley, Kickapoo, and Homestead Valley faults, have indicated that typical recurrence intervals are on the order of 5-15 Ka (Rockwell et al., 2000; Rubin and Sieh, 1997). This is consistent with the subdued geomorphic expression of these faults. These observations, along with recent seismic activity and its more northerly orientation, have been cited as evidence of the relative youth of the ECSZ relative to the SAF (Nur et al., 1993; Du and Aydin, 1996). Du and Aydin (1996) hypothesized the tectonic origins for the ECSZ are the obliquity of the Big Bend in the San Andreas Fault to plate motion (~30°) and the construction of the structural knot

resulting from a 15-km-wide left-step in the SAF at San Gorgonio Pass. They envision these geometric complexities as asperities, which hinder through-going rupture of the San Andreas Fault and result in strain build-up to the east that produces the shear zone.

The NFTS is a complex structure that is a part of the Transverse Ranges structural province. The central Transverse Ranges lie to the east of the SAF and trend obliquely to the general tectonic grain of the plate margin (Meisling and Weldon, 1989). They consist mainly of the San Bernardino Mountains, which are an isolated, high range separated from adjacent mountain blocks by the NFTS, SAF, and Pinto Mountain fault (Figure 3) (Spotila et al., 1998). The primary sources of convergence responsible for this range are the Big Bend of the SAF and the small stepover at San Gorgonio Pass (Figure 3). Budgeting plate motion onto structures near the Big Bend reveals ~13 mm/yr of residual convergent motion relative to the SAF with an orientation of N38°E that cannot be partitioned onto any known structure (Figure 6) (Spotila et al., 2001). The northern two thirds of the San Bernardino Mountains is comprised of the Big Bear fault block, which has a steep northern escarpment in crystalline bedrock that is separated from the Mojave Desert to the north by the NFTS (Figure 4)(Spotila et al., 1998; Meisling and Weldon, 1989; Bull, 1977; Dibblee, 1975). The NFTS is a broad, ~1-km-wide, complex zone of discontinuous reverse fault segments and folds (Bryant, 1986; Miller, 1987; Meisling, 1984; Spotila and Sieh, 2000). The segmented and overlapping faults and folds define an overall horizontal length of 80 km, trending approximately N80°W. It is believed the NFTS integrates into a main thrust fault at depth beneath the Big Bear block (Li et al., 1992; Spotila and Sieh, 2000). An impressive escarpment, prominent Pleistocene scarps, and offset alluvial fans suggest the NFTS has been active recently (Bull, 1977; Rzonca

and Clark, 1982; Meisling and Weldon, 1989; Bryant, 1986; Meisling, 1984). However, its most recent displacement history is not known, and previous studies have postulated that it has become extinct (Sadler, 1982: Meisling and Weldon, 1989).

No clear cross cutting relationships can be established between the ECSZ and NFTS. The traces of both fault systems appear to be disturbed at their intersection (Figure 7). If the ECSZ is more active or postdates the NFTS, the trace of the thrust would be offset right laterally. The deflection in its trace at the Helendale Fault could be consistent with this (Figure 4). The Helendale Fault can also be traced in both the hangingwall and footwall of the NFTS, although the hangingwall trace (Helendale #1 and Helendale #2; Spotila and Sieh, 2000) appears to diverge into a graben (Figure 4). This change in character makes the fault geometry also consistent with offset of the Helendale Fault by the NFTS. Northward motion of the upper plate could offset the hangingwall Helendale Fault from its original position to the Pipes Canyon Fault (Figure 4). Adding to this ambiguity, there is no geomorphic evidence in young alluvium where the NFTS and the Helendale Fault should intersect to suggest one fault offsets the other (Bryant, 1986). It is thus not possible to identify short or long term displacement of either fault trace. Although the ECSZ has been recently active and the geologic and seismic records fail to show when the NFTS last ruptured, the NFTS cannot be labeled extinct on the basis of a cross-cutting relationship.

If active, the NFTS may represent a significant seismogenic source to the surrounding region. In the worst hazard scenarios (Figure 1), the NFTS could rupture entirely, with or without coupling to the ECSZ. The resulting rupture length of up to 80 km, gentle fault dip, and depth to the brittle-ductile transition (~15 km) (Spotila and Sieh,

2000), would result in an event of M>7 (Wells and Coppersmith, 1994). Based on the 1992 Big Bear earthquake (M6.5), such an event would be very damaging to the surrounding population of the San Bernardino Valley. It is thus crucial to know whether the NFTS is active. To assess the seismic hazard it may represent, it is also necessary to quantify previous rupture patterns and the relationship to events on the ECSZ.

The possible strain accumulation on the NFTS may also be important to the cycle of the SAF. Neither the 1857 nor 1812 events along the SAF ruptured as far south as the San Bernardino Mountains (Figure 3) (Grant and Sieh, 1994; Fumal et al., 1993; Sieh et al., 1989; Jacoby et al., 1988; Weldon and Sieh, 1985). Yet, paleoseismic studies suggest this section of the SAF has a short recurrence interval of several hundred years (Weldon and Sieh, 1985; Sieh et al., 1989). This segment was also brought closer to failure by the 1992 Landers earthquake. Dextral motion in this event relieved a small portion of the normal stress on the SAF to the southwest (Figure 4), thus increasing its Coulomb failure stress by 6-12 bars and decreasing the recurrence interval for major rupture by ~14-20 years (Stein et al., 1992; Harris and Simpson, 1992; Jaume and Sykes, 1992). The San Bernardino segment of the SAF is thus a dangerous seismic source poised to fail. The mechanical effect of the strain accumulation or release on the NFTS could in turn affect the timing of the incipient SAF rupture. The close proximity, oblique orientation, and motion associated with the NFTS would have an effect on the SAF similar to the Landers event. North-south convergent strain accumulating on the NFTS exerts a normal stress on the SAF, such that an event on the NFTS would increase the SAF's Coulomb failure stress and bring it closer to failure. It is thus critical to know whether the NFTS is active and where it may be in its seismic cycle.

1.3 Recent Activity of the ECSZ and the NFTS

The ECSZ has a well documented historical and paleoseismic record of seismicity. The 1992 Landers event (Sieh et al., 1993) sparked interest in the activity of the shear zone and led to paleoseismic investigations along several individual fault strands. Rupture histories have been documented for numerous faults to the east of the NFTS, including the northern and southern Johnson Valley Fault and Emerson Fault. These show multiple ruptures in the Holocene with typical repeat times of ~5-10 Ka (Rockwell et al., 2000; Rubin and Sieh 1997; Bryan and Rockwell, 1995; Hecker et al, 1993). Constraints also exist for faults that intersect the NFTS. Hecker et al. (1993) documented three events over the past 15 Ka along the Homestead Valley fault, yielding a recurrence interval of 5-8 Ka. Bryan and Rockwell (1995) documented two events on the Helendale fault at 1 Ka and 9 Ka. The Lenwood fault has a comparable earthquake history, with events at 0.1 Ka, 5.5 Ka, and 9 Ka yielding a recurrence interval of 3.5-5 Ka (Padgett and Rockwell, 1995). The ECSZ, including strands that intersect the NFTS, has thus been seismically active repeatedly during the Holocene.

The total bedrock uplift along the impressive escarpment of the San Bernardino Mountains is ~1.6 km (Spotila and Sieh, 2000). Stratigraphic evidence from the Old Woman Sandstone formation constrains initiation of this uplift to post 2-3 Ma (May and Repenning, 1982). This suggests a long-term uplift rate $\geq$0.53 mm/yr. Numerous morphologically sharp, late-Pleistocene scarps suggest recent activity, based on field and airphoto observations (Spotila and Anderson, 2000) (Figures 8, 9). Entrenched alluvial fans at the base of the range also become more incised towards the range front,

suggesting recent tectonic tilting. Yet, according to some studies, evidence for very late-Pleistocene or Holocene activity along the NFTS is weak. Ages of several scarps within the alluvial surface along the range front have been constrained based on correlation with older alluvial surfaces, soil profile development, weathering surfaces of boulders, and the degree of preservation of constructional surface morphology (Meisling and Weldon, 1989; Bryant, 1986). These ages and the heights of scarps suggest uplift rates that are more than an order of magnitude lower than the long-term rate (0.05-0.30 mm/yr, based on Meisling, 1984 (0.4 Ma, 36-70 m-high); Meisling and Weldon, 1989 (0.5 Ma, 25 m-high); Bryant, 1986 (130 Ka, 40 m-high)). There has also been a lack of historical seismic activity along the thrust. One moderate (M 5.4) earthquake did occur on the NFTS in 1992 (Feigl et al, 1995). However, this event was located within the region affected by the Landers earthquake and was considered an aftershock that did not necessarily result from primary tectonic strain. Another large event in the area was the 28 June 1992 (Mw 6.5) Big Bear event (Figure 4), also an aftershock of Landers. This was located on a vertical fault with dominantly strike-slip motion and no evidence of surface deformation (Sieh et al., 1993). The area surrounding the NFTS has also not shown any accumulation of convergent strain over the eight years (1992-2000), unlike dextral shear along the northern ECSZ (Peltzer et al, 2001). Despite geomorphic indicators of late-Pleistocene activity, previous geologic and seismologic studies have thus failed to demonstrate a recent major rupture of the NFTS. The apparent decrease in uplift rate and lack of disturbed Holocene alluvium could indicate that the NFTS is no longer active or that it is strongly hindered by its intersection with the ECSZ.

There is some evidence that the ECSZ has affected the previous activity on the NFTS. The NFTS can be delineated into three segments based on varying tectonic expression across the range front (Figure 10). The Helendale fault serves as a boundary between the western and central segments that separates an area with clearly defined evidence of thrust faulting from a zone where the predominant faulting mechanism is not apparent. The boundary between the eastern and central segments corresponds to the Old Woman Springs fault and is less well defined. The eastern segment has the most poorly developed features. The bedrock escarpment tapers to zero eastward and there are very few mapable thrust scarps with sharp, relatively-young morphologies (Spotila and Anderson, 2000) (Figures 10, 11). The lack of evidence for thrust motion on this segment could indicate that dextral faults of the ECSZ in the footwall have replaced thrusting. The central segment contains traces of the ECSZ within the footwall and hanging wall of the NFTS, but it is not clear which fault system dominates. Large folds and isolated scarps can be mapped within the footwall and suggest a different deformational regime than elsewhere, but this may also result from the influence of carbonate versus granitic bedrock on soil development and preservation of landforms with resistant petrocalcic horizons (Eppes et al, 2002) (Figures 10, 12). Absence of dextral faults and a dominance of thrusting mark the western segment. Bedrock relief is greatest and there are numerous discontinuous thrust scarps breaking late-Pleistocene fanglomerate with moderate soil development (Figures 8. 10). Pleistocene fault scarps occur along greater than 2/3 of the range front west of the Helendale Fault, whereas less than 1/3 of the range front contains scarps along segments to the east of the Helendale Fault. Of the entire NFTS, the easternmost section of the western segment shows the

youngest tectonic geomorphology (Spotila and Anderson, 2000). This attests to the ongoing activity and dominance of thrust motion within the western segment. Based on the fact that these segments with different tectonic morphologies correspond to intersections with strands of the ECSZ, it seems possible the strike-slip faults mechanically influence the NFTS. It thus appears as though the strike-slip strands parcel the NFTS into segments that have a different structural style or deformation history.

1.4 Investigations

In an effort to understand how intersecting faults interact, it is important to quantify their previous rupture behavior. In the case of the ECSZ and the NFTS, the historical record of seismicity is not sufficient. By excavating a trench perpendicular to a fault plane, we can observe coseismically-offset layers and overlying undisturbed layers that record subsequent deposition. Radiocarbon dating of detrital charcoal or other organics from the youngest offset layer and the oldest undisturbed layer constrain the maximum and minimum ages of a rupture event. By utilizing this method, the historical seismic record can be extended thousands of years into the past.

The first step in determining how the ECSZ and NFTS interact is to determine if the NFTS is active, by constraining its most recent rupture history with paleoseismology. A careful screening of the entire thrust system was completed in order to identify the youngest fault scarps. Two sites along the western segment (Furnace Canyon and Marble Canyon) (Figure 10) were chosen for paleoseismic investigation. At both sites, surface exposure of stratigraphy within canyons reveal flat–lying nearly horizontal layers, even within the large thrust scarps. The layers are preserved except in the region where the

material has slumped forming a colluvial wedge, related to tectonic activity. This indicates the observed features are not folds. At the Furnace Canyon site, Stage IV petrocalcic horizons are also found that may indicate a scarp age of up to 100 Ka. Therefore, multiple seismic events may be preserved in the young alluvium proximal to this scarp. By constraining the age of the most recent rupture event at these locations, we may show whether the NFTS has been recently active and, in turn, whether the NFTS and ECSZ have been coactive. If so, we can then begin to explore scenarios for how they interact.

Examination of these field sites illustrated the geomorphic complexity of deformation in an alluvial fan setting and pointed to the value of pre-excavation subsurface imaging. We thus explored the application of ground penetrating radar (GPR) to characterize the shallow structure of candidate paleoseismic sites. GPR is a geophysical technique used for high-resolution imagery of the shallow subsurface (Davis and Annan, 1989). It uses high frequency waves to image the reflective responses of subsurface features and may thus be useful for imaging alluvial layers that are offset or juxtaposed along faults and fault plane reflectors. This would be useful information prior to excavation of an ambiguous paleoseismic site. We thus used GPR at both sites. It was applied first at the Marble Canyon site, where previous trenching had determined the subsurface structure (Figure 10). This proved GPR to be useful towards imaging fault traces as precharacterization to paleoseismic excavation. It was then applied at the furnace Canyon site, to better define fault geometry and the necessary excavation dimensions.

In summary, a better understanding of intersecting fault systems can lead to a breakthrough in our ability to assess seismic hazards. If we are able to understand the interactions of complex intersecting fault systems, it may be possible to predict scenarios of rupture. The paleoseismic histories of the NFTS and the ECSZ may hold important clues for determining their previous behavior and interactions. We may also learn more about thrust fault segmentation and the role of cross structures as segment boundaries. For these reasons and the other issues related to regional seismic hazard, the NFTS-ECSZ intersection is an ideal location to study.

Chapter 1: Figure Captions

Figure 1–Diagrams illustrating possible rupture patterns and segmentation scenarios that may be associated with complex intersecting faults. (A) Strike-slip faults may behave as segment boundaries, effectively limiting the rupture length and magnitude of a thrust event. Individual segments may exhibit different slip rate or deformation style. Sustained alignment of the thrust segments is unlikely. (B) The fault systems may be mechanically coupled such that rupture of one fault triggers the rupture of an adjacent strand of the opposing fault system. For example, a thrust earthquake may trigger a strike-slip earthquake (green arrows). (C) The opposing fault systems may rupture independent of one another (decoupled). In this case, either fault may rupture the entire length of its trace. This geometry is inherently unstable. (D) One fault system may be inactive, such that their spatial association represents a cross cutting relationship. Note that A, B, and C are all possible, but are metastable and will rapidly evolve into scenario D.

Figure 2–Historical earthquake ruptures and proposed large earthquake sources within the Los Angeles metropolitan area (from Dolan et al., 1995). Black areas denote surface projections of thrust rupture planes of historic earthquakes, date (19xx) and magnitude (Mw). Historic ruptures on vertical strike-slip faults are shown as heavy black lines. Colored polygons represent projections of thrust fault planes (solid barbs denote thrust faults that break the surface and open barbs represent blind thrust faults). Thin lines denote near-vertical strike-slip faults. Thrust fault patches are grouped by color into possible rupture extent of future

large earthquakes, with the resulting magnitude and recurrence interval shown (Mw 7.2-7.6, 500-1010 yrs). Strike-slip faults mark the boundary of many of these hypothetical ruptures, and smaller ruptures are possible if strike-slip faults within the shaded regions act as segment boundaries. This illustrates the importance of understanding fault interactions for quantifying seismic hazards of complexly associated faults.

Figure 3–Tectonic map of southern California, showing location of the San Bernardino Mountains (SBMs) and their relationship to the major fault systems of the region (from Spotila and Sieh, 2000). Box shows location of Figure 4. The relative motion of the Pacific plate in reference to a fixed North American plate is 50 mm/yr in the northwest direction. ECsz = Eastern California shear zone, eTR = eastern Transverse Ranges, GF = Garlock Fault, NI-F = Newport Inglewood fault, PMF = Pinto Mountain Fault, SAFcv = Coachella Valley segment of San Andreas fault, SAFm = Mojave segment of San Andreas fault, SAF-SB = San Bernardino segment of the San Andreas fault, SJF = San Jacinto fault, SM-CF Sierra Madre-Cucamonga fault, W-EF = Whittier-Elsinore fault, wTR = western Transverse Ranges.

Figure 4–The major faults and blocks of the San Bernardino Mountains (from Spotila and Sieh, 2000). Note the complexity of the NFTS, which consists of multiple fault strands and folds. Northwest trending dextral faults occur north and south of the NFTS, but none clearly offsets the trace of the thrust. Part of the NFTS, however, consists of NW trending dextral fault strands (Blackhawk fault, Sky High Ranch fault). Recent seismicity (>M5) is plotted as focal mechanisms.

The Landers event (Mw 7.3) was located on the Johnson Valley fault and resulted in two aftershocks on the NFTS (Mw 6.5 on 6/28/92 and Mw 5.4 on 12/04/92). SAT = Santa Anna Thrust, BFFZ = Barton Flats fault zone.

Figure 5–Fault map of the Mojave Desert highlighting the location of late Cenozoic faults and associated features of the ECSZ (from Dokka and Travis, 1990). The ECSZ is a complex system of faults with several major strands with documented ruptures within the past 10,000 yrs intersecting or proximal to the NFTS (i.e. Helendale, Old Woman Springs, Lenwood, and Johnson Valley faults). AM, Alvord Mountains; AW, Avawatz Mountains; BM, Bristol Mountains; CM, Calico Mountains; CdM, Cady Mountains; CP, Cajon Pass; GM, Granite Mountains; MH, Mud Hills; MM, Marble Mountains; NM, Newberry Mountains; OM, Ord Mountain; PR, Paradise Range; RM, Rodman Mountains; SBM San Bernardino Mountains.

Figure 6-Velocity diagram for Pacific-North America plate motion at the latitude of the San Bernardino Mountains (from Spotila et al., 2001). All slip rates are based on the data summarized by the Working Group for California Earthquake Probabilities (1995). SAF, San Andreas fault (25 mm/yr); SJF, San Jacinto fault (10 mm/yr); ECSZ, Eastern California Shear Zone (8 mm/yr); WEF, Whittier-Elsinore fault (2.5 mm/yr); NIF, Newport-Inglewood fault (1.5 mm/yr); SCF, San Clemente fault (3 mm/yr). The total North American-Pacific relative plate motion is ~50 mm/yr (Stock and Molnar, 1988). When the motion vectors and plate motion vector are connected, the remaining vector

must connect to the plate motion vector (DeMets, 1995). The residual vector of convergence is equivalent to 12.6 mm/yr @ S38°W.

Figure 7–Diagram illustrating possible cross cutting relationships between the NFTS and ECSZ. (A) Scenario in which the NFTS is extinct and the ECSZ is more recently active. In this case, the trace of the NFTS is offset dextrally. This could be reflected by the bend in the thrust trace in the vicinity of the Helendale fault. (B) Scenario in which the ECSZ is extinct and the NFTS is active. In this case, northward motion of the upper plate could offset the hangingwall trace of the Helendale fault from its original position to the Pipes Canyon fault. Either offset scenario may be possible, even if both fault systems are coactive.

Figure 8-Airphoto of the western segment of the NFTS adapted from 1:30000 airphotos. This photo is located at the intersection of the Helendale fault and the NFTS (Figure 4). Sharp, morphologically young-looking thrust scarps within Pleistocene alluvium are common. In areas where folding is dominant, the geomorphology is complex. Relief is highest within this segment reaching ~1 km. These geomorphic features suggest more recent and more rapid thrust deformation than the other segments. The linear trace of the Helendale fault can be clearly delineated, defining the boundary between the central and western segments. The white areas in the photo are areas of anthropogenic disturbance, such as roads and quarries.

Figure 9–Photo of Pleistocene scarp and thrust plane exposed in road cut along the western segment (Figure 8). The low angle trace of the North Frontal Thrust

can be seen in this photo with light brown alluvium in the hangingwall and brown to red alluvium in the footwall. The alluvium appears warped due to a component of folding within the hangingwall. This scarp within the Pleistocene alluvium is nearly 4 meters-high. Scarps such as this have been cited as evidence for recent activity of the thrust.

Figure 10–Neotectonic map of the North Frontal thrust system based on airphoto mapping and field observations (Spotila and Anderson, 2000). The eastern segment has the most poorly developed features with very few mapable thrust scarps with sharp, relatively-young morphologies. The boundary between the eastern and central segments corresponds to the Old Woman Springs fault and is less well defined. The central segment contains traces of the ECSZ within the footwall and hanging wall of the NFTS, but it is not clear which fault system dominates. Large folds and isolated scarps can be mapped within the footwall and suggest a different deformational regime than elsewhere. The Helendale fault serves as a boundary between the western and central segments. Absence of dextral faults and the presence of numerous discontinuous thrust scarps breaking late-Pleistocene fanglomerate dominates the western segment. Pleistocene fault scarps occur along greater than 2/3 of the range front west of the Helendale Fault, whereas less than 1/3 of the range front contains scarps along segments to the east of the Helendale Fault. The strike-slip faults of the ECSZ may mechanically influence the activity of the NFTS, segmenting the thrust into sections of varying tectonic morphologies.

Figure 11-Airphoto of the eastern segment of the NFTS adapted from 1:30000 airphotos. This photo is located south of the Silver Reef fault along the NFTS (Figure 4). Note the lack of folds and prominent thrust scarps. The bedrock escarpment has a smooth and subdued morphology that is more sinuous due to onlapping alluvium covering the basement rock. The relief is much lower in this area, tapering to zero at the eastern extremity of the segment. There is no apparent evidence of activity associated with the NFTS in this area, however recorded seismicity associated with the ECSZ has been common.

Figure 12-Airphoto of the central segment of the NFTS adapted from 1:30000 airphotos. This photo is located at east of the intersection between the Helendale fault and the NFTS (Figure 4). The Helendale fault (the segment boundary between the central and western segments) is located to in the western section of the photo. Very few prominent scarps are seen within the Pleistocene alluvium. However, there is a prominent fold in the north-central portion of the figure. The white areas in the photo are areas of anthropogenic disturbance, such as roads and quarries. Thrust scarps and folds are evidence of activity associated with the NFTS, yet prominent strands of the ECSZ are also present. It is not understood if one fault system dominates or if they are coactive.

Figure 1

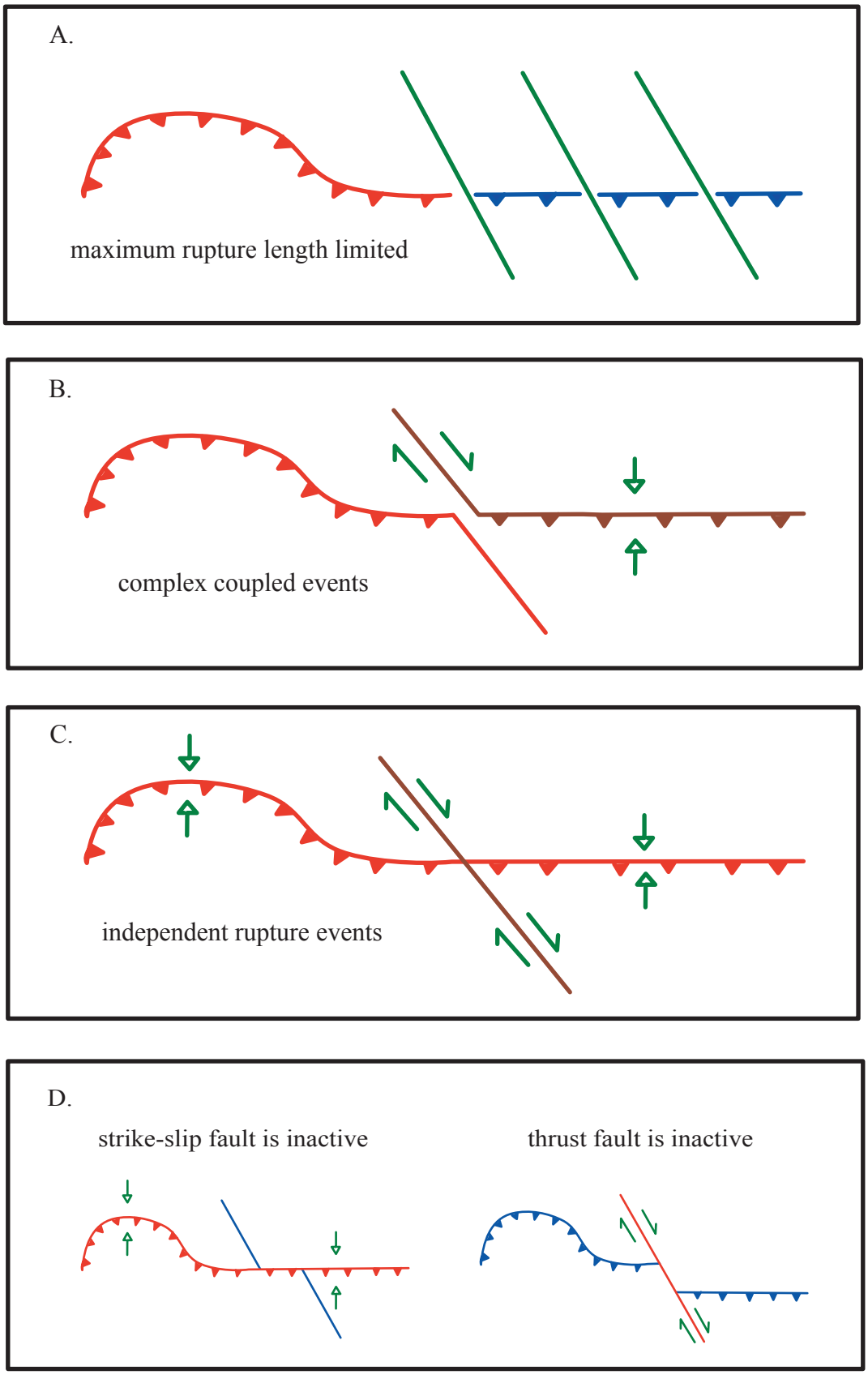
A.
maximum rupture length limited
B.
complex coupled events
C.
independent rupture events
D.
strike-slip fault is inactive
thrust fault is inactive

Figure 2

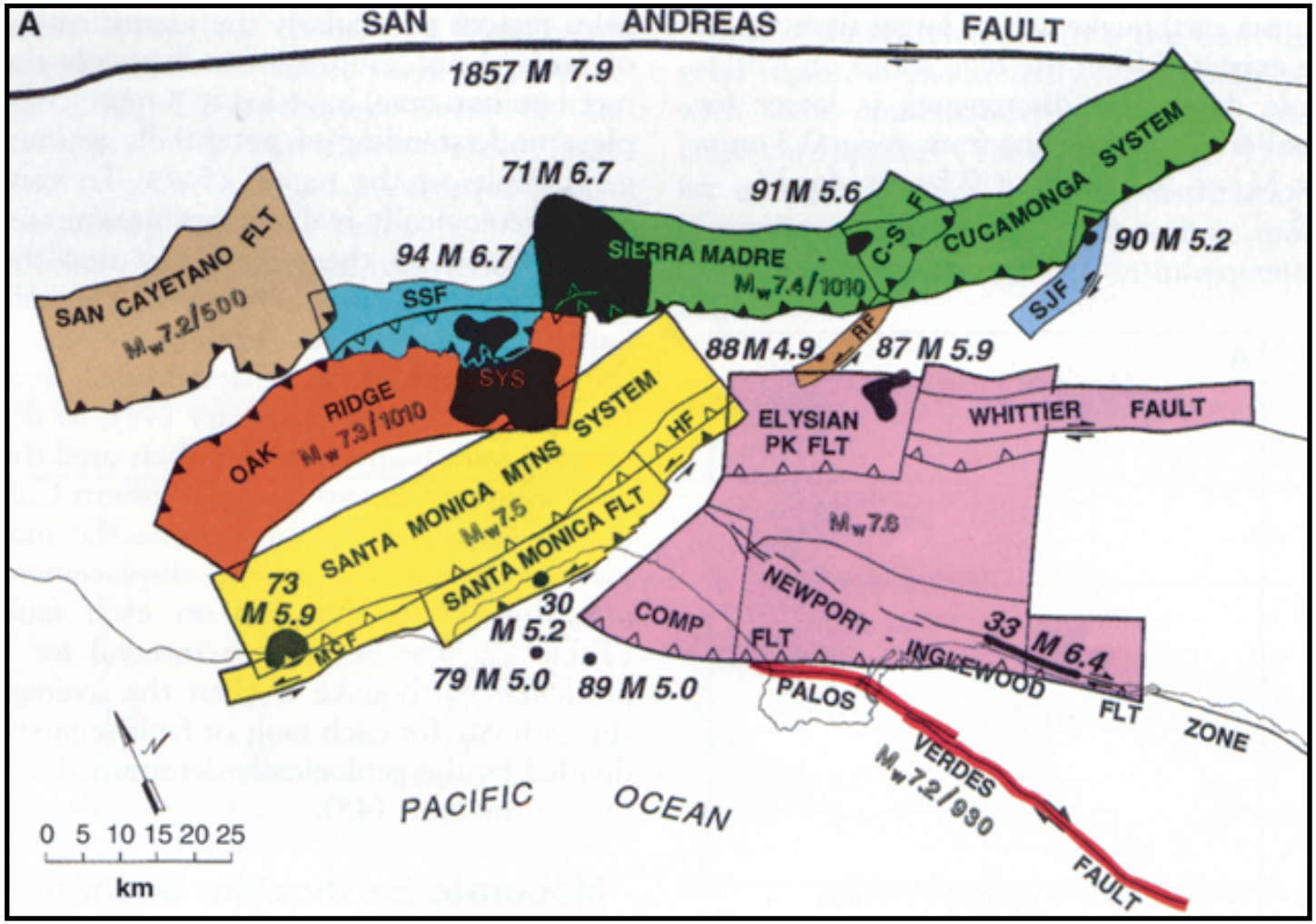
A
SAN ANDREAS FAULT
1857 M 7.9
71 M 6.7
91 M 5.6
94 M 6.7
90 M 5.2
88 M 4.9
87 M 5.9
SAN CAYETANO FLT
Mw7.2/500
SSF
SIERRA MADRE
Mw7.4/1010
C-S
CUCAMONGA SYSTEM
SJF
RF
SYS
OAK RIDGE
Mw7.3/1010
SANTA MONICA MTNS SYSTEM
Mw7.5
HF
ELYSIAN PK FLT
WHITTIER FAULT
Mw7.8
73 M 5.9
SANTA MONICA FLT
30 M 5.2
MCF
COMP
NEWPORT - INGLEWOOD FLT
33 M 6.4
79 M 5.0
89 M 5.0
PALOS VERDES
Mw7.2/930
FAULT ZONE
PACIFIC OCEAN
0 5 10 15 20 25
km

Figure 3

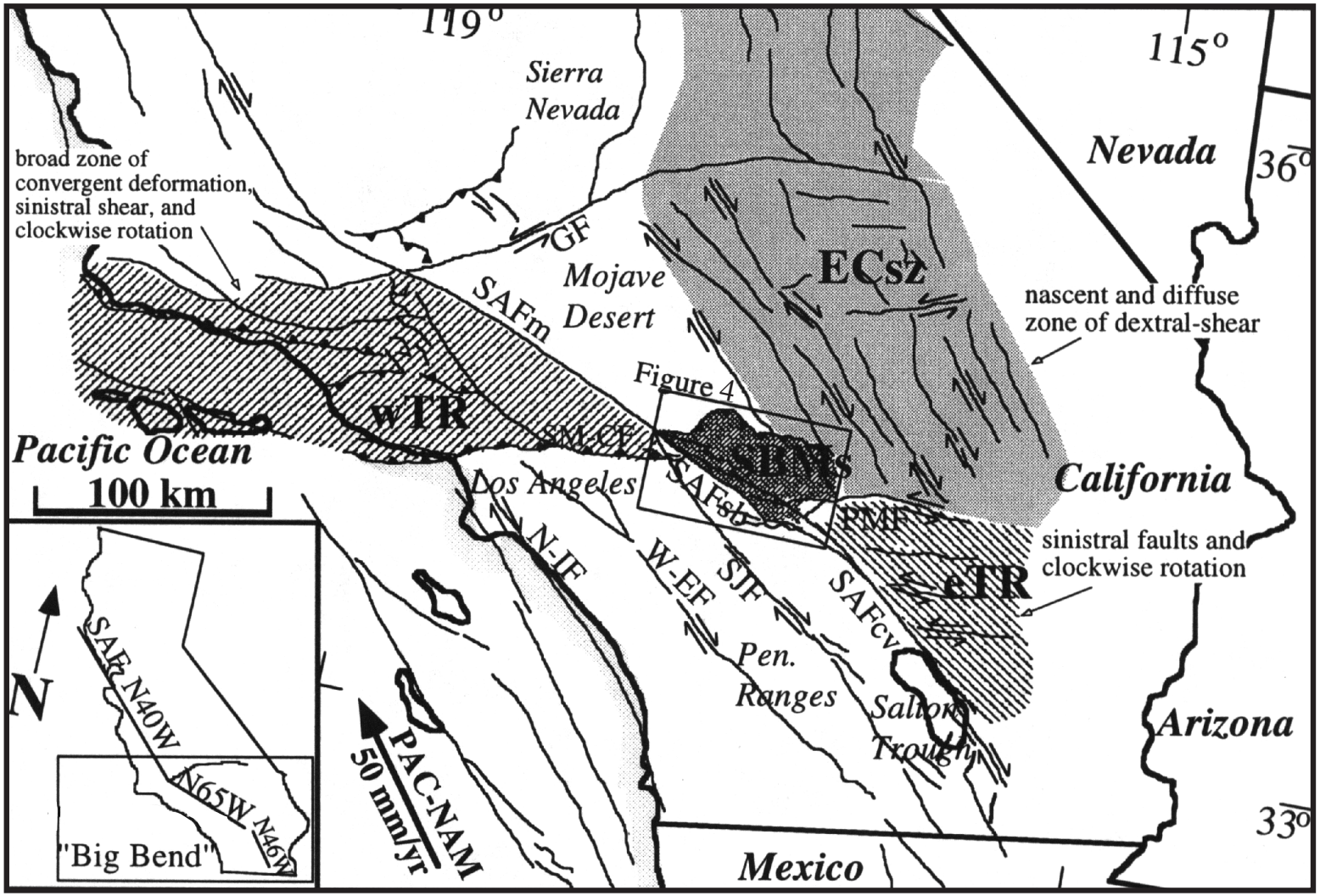
119°
115°
Sierra
Nevada
Nevada
36°
broad zone of
convergent deformation,
sinistral shear, and
clockwise rotation
GF
Mojave
Desert
ECsz
nascent and diffuse
zone of dextral-shear
SAFm
Figure 4
wTR
SNAF
LTMs
Pacific Ocean
100 km
Los Angeles
SAFsb
PMF
California
sinistral faults and
clockwise rotation
N-IF
W-EF
SJF
SAFcv
eTR
Pen.
Ranges
Salton
Trough
Arizona
N
SAF N40W
N65W
N46W
"Big Bend"
PAC-NAM
50 mm/yr
33°
Mexico

Figure 4

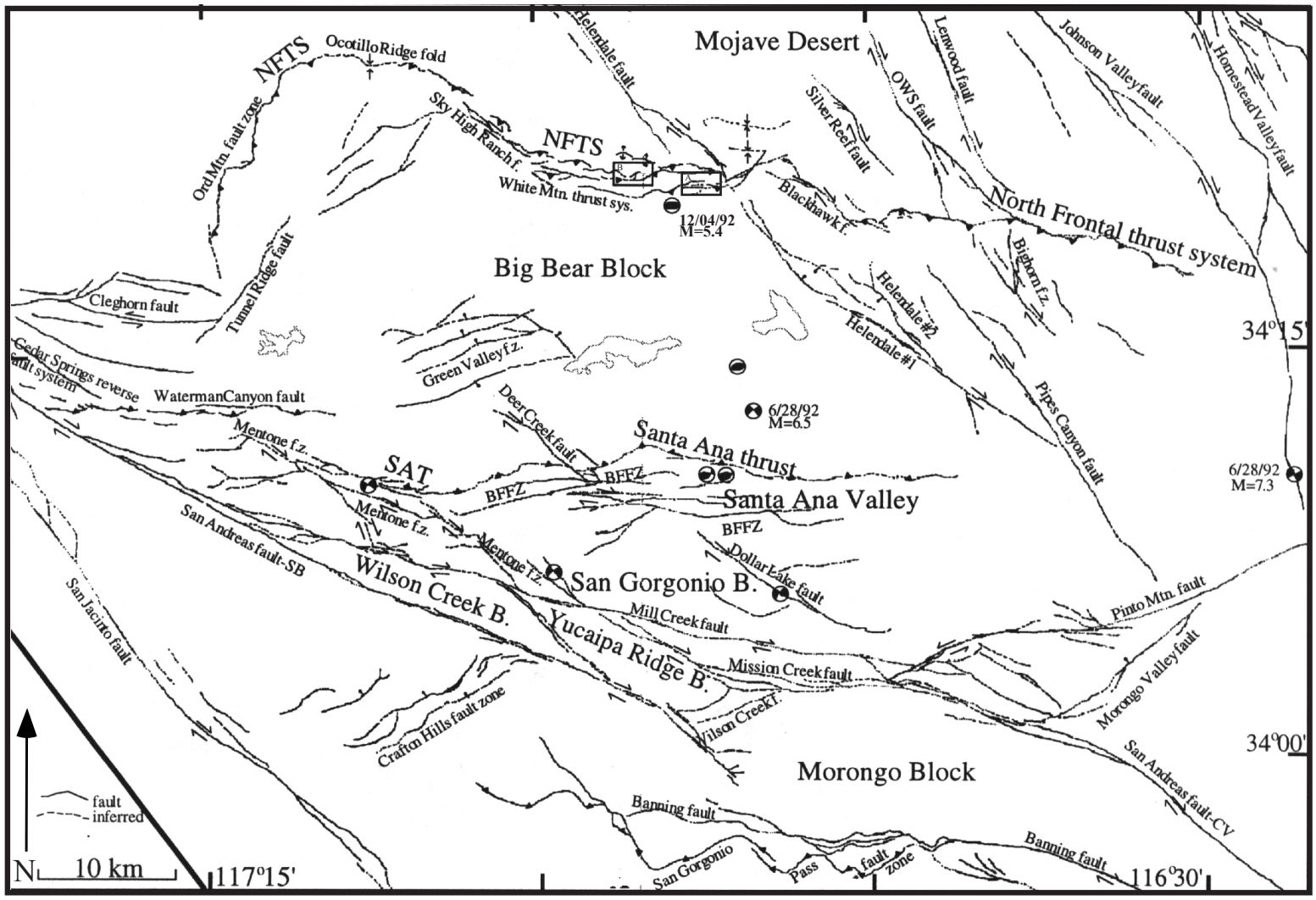
Mojave Desert
NFTS
Ocotillo Ridge fold
Ord Mtn. fault zone
Sky High Ranch f.
NFTS
White Mtn. thrust sys.
12/04/92
M=5.4
Helendale fault
Lenwood fault
OWS fault
Silver Reef fault
Johnson Valley fault
Homestead Valley fault
Blackhawk f.
North Frontal thrust system
Bighorn f.z.
Big Bear Block
Tunnel Ridge fault
Cleghorn fault
Helendale #2
Helendale #1
34°15'
Cedar Springs reverse fault system
Waterman Canyon fault
Green Valley f.z.
Deer Creek fault
6/28/92
M=6.5
Pipes Canyon fault
6/28/92
M=7.3
Mentone f.z.
SAT
BFFZ
Santa Ana thrust
Santa Ana Valley
San Andreas fault-SB
Mentone f.z.
Mentone f.z.
BFFZ
Dollar Lake fault
San Gorgonio B.
Wilson Creek B.
Yucaipa Ridge B.
Mill Creek fault
Pinto Mtn. fault
Morongo Valley fault
San Jacinto fault
Mission Creek fault
Wilson Creek f.
Crafton Hills fault zone
34°00'
Morongo Block
San Andreas fault-CV
Banning fault
fault
inferred
N
10 km
117°15'
San Gorgonio Pass fault zone
Banning fault
116°30'

Figure 5

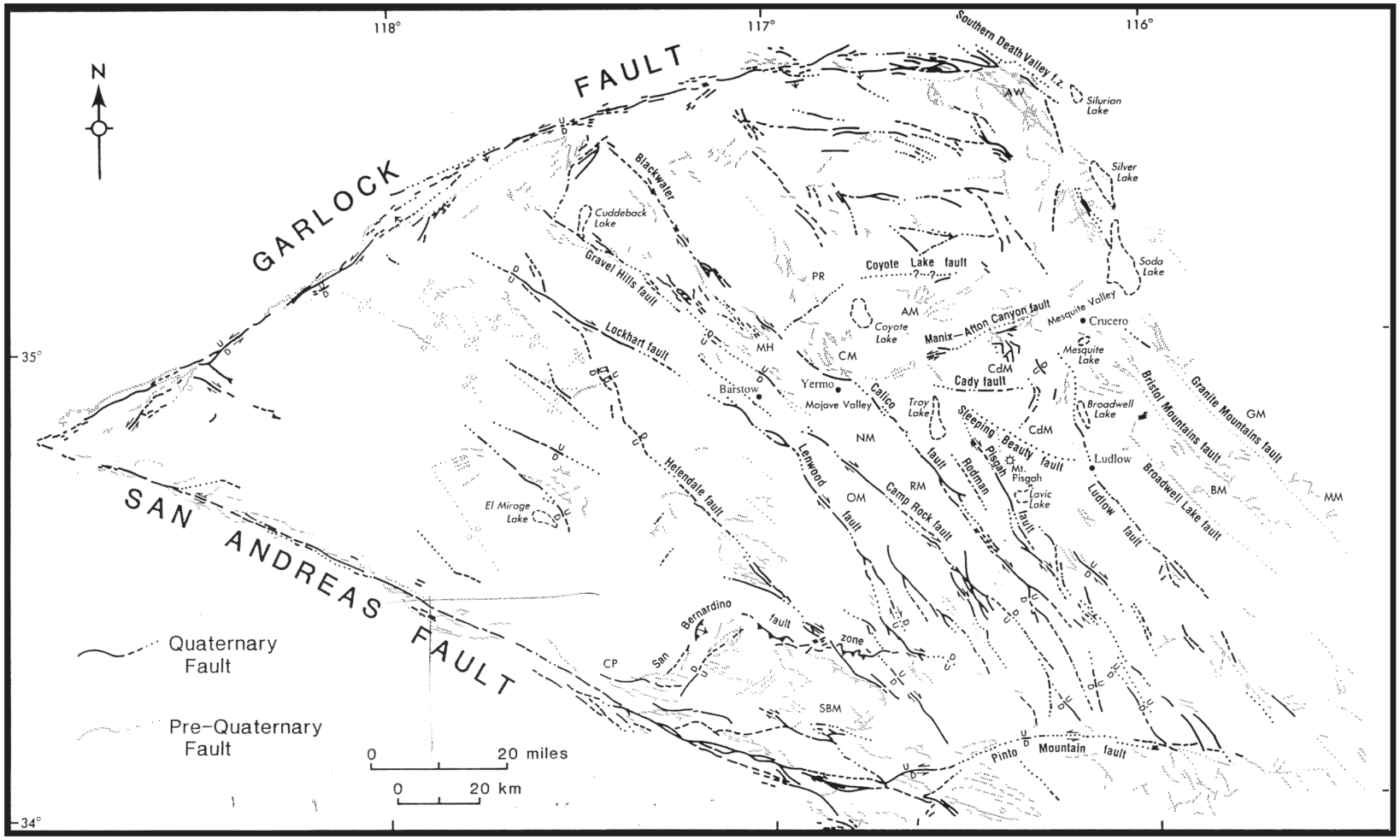
118°
117°
116°
35°
34°
N
GARLOCK FAULT
SAN ANDREAS FAULT
Southern Death Valley f.z.
Silurian Lake
Silver Lake
Soda Lake
Blackwater
Cuddeback Lake
Gravel Hills fault
Lockhart fault
Coyote Lake fault
Coyote Lake
Manix—Afton Canyon fault
Mesquite Valley
Crucero
Mesquite Lake
Cady fault
Barstow
Yermo
Mojave Valley
Calico
Troy Lake
Sleeping Beauty fault
Broadwell Lake
Bristol Mountains fault
Granite Mountains fault
Ludlow
Broadwell Lake fault
Ludlow fault
Pisgah
Mt. Pisgah
Lavic Lake
Rodman fault
Camp Rock fault
Lenwood fault
Helendale fault
El Mirage Lake
San Bernardino fault zone
Pinto Mountain fault
PR
AM
MH
CM
CdM
NM
RM
OM
CP
SBM
GM
BM
MM
Quaternary Fault
Pre-Quaternary Fault
0 20 miles
0 20 km

Figure 6

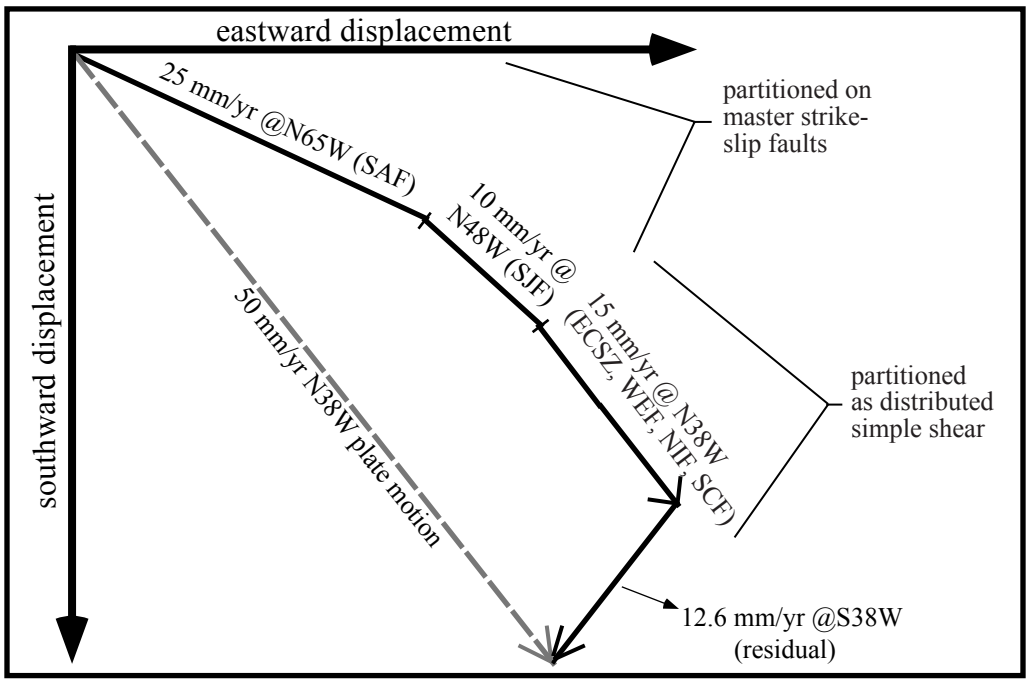
eastward displacement
southward displacement
25 mm/yr @N65W (SAF)
10 mm/yr @ N48W (SJF)
15 mm/yr @ N38W (ECSZ, WEF, NIF, SCF)
50 mm/yr N38W plate motion
partitioned on master strike-slip faults
partitioned as distributed simple shear
12.6 mm/yr @S38W (residual)

Figure 7

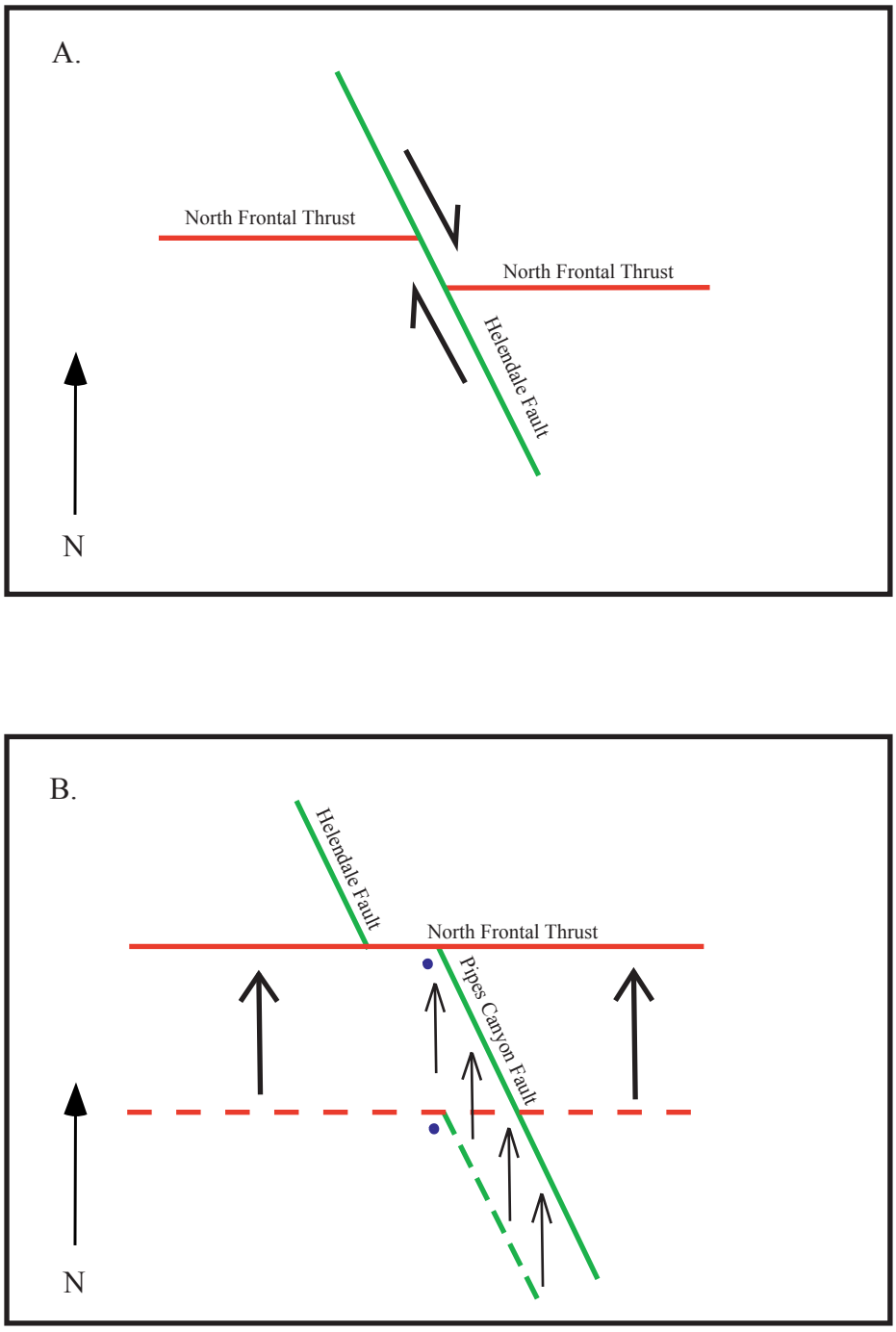
A.
North Frontal Thrust
North Frontal Thrust
Helendale Fault
N
B.
Helendale Fault
North Frontal Thrust
Pipes Canyon Fault
N

Figure 8

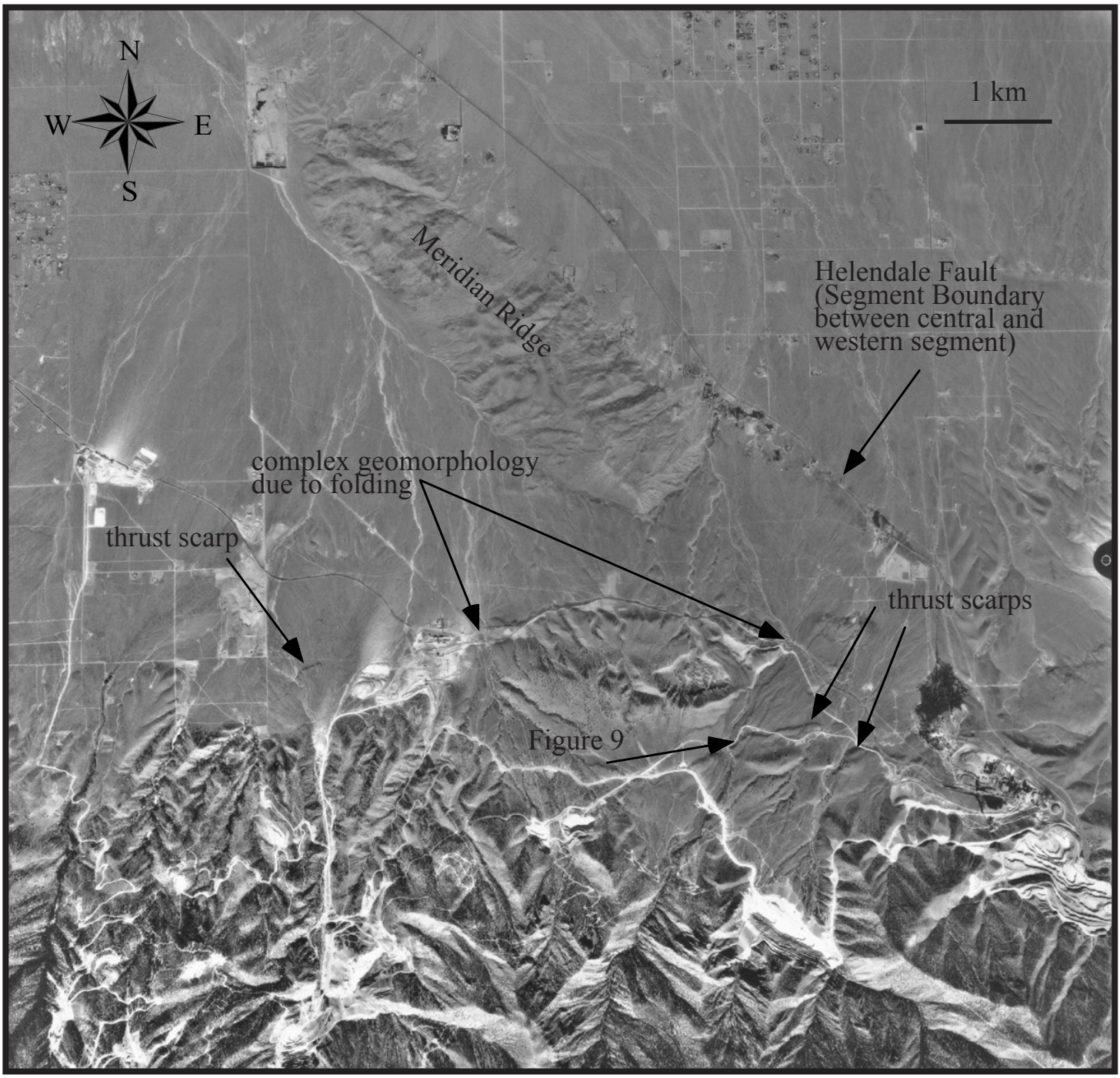
N
W
E
S
1 km
Meridian Ridge
Helendale Fault
(Segment Boundary
between central and
western segment)
complex geomorphology
due to folding
thrust scarp
thrust scarps
Figure 9

Figure 9

Figure 10

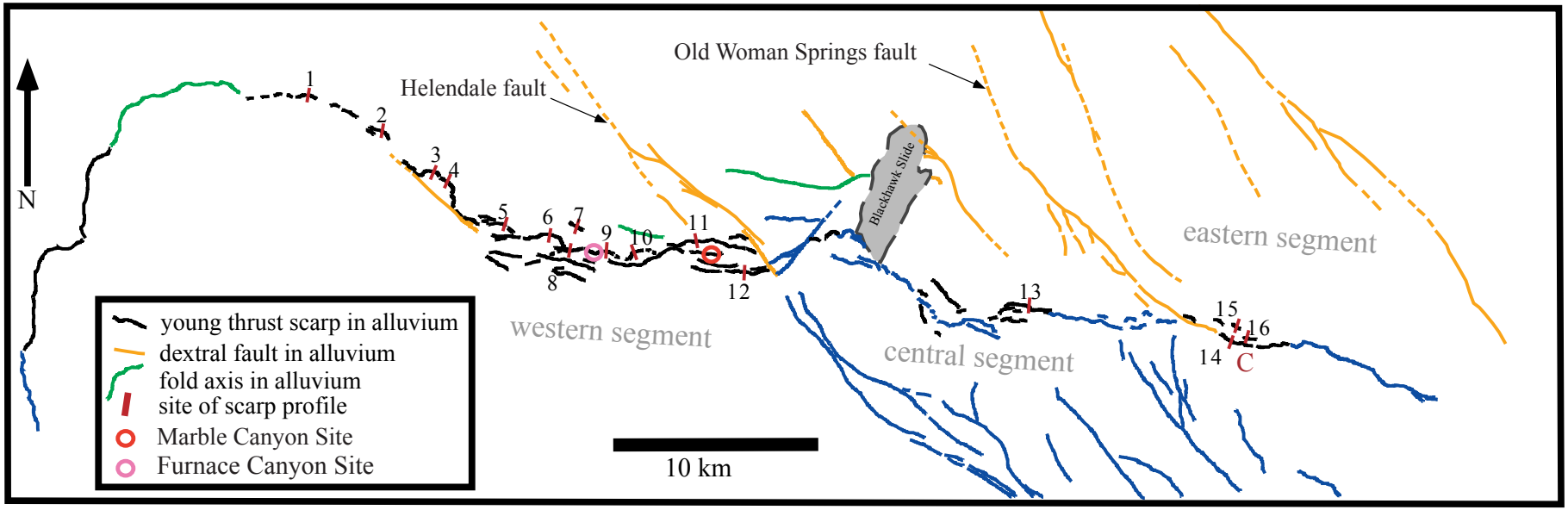
N
Helendale fault
Old Woman Springs fault
Blackhawk Slide
western segment
central segment
eastern segment
1
2
3
4
5
6
7
8
9
10
11
12
13
14
15
16
C
young thrust scarp in alluvium
dextral fault in alluvium
fold axis in alluvium
site of scarp profile
Marble Canyon Site
Furnace Canyon Site
10 km

Figure 11

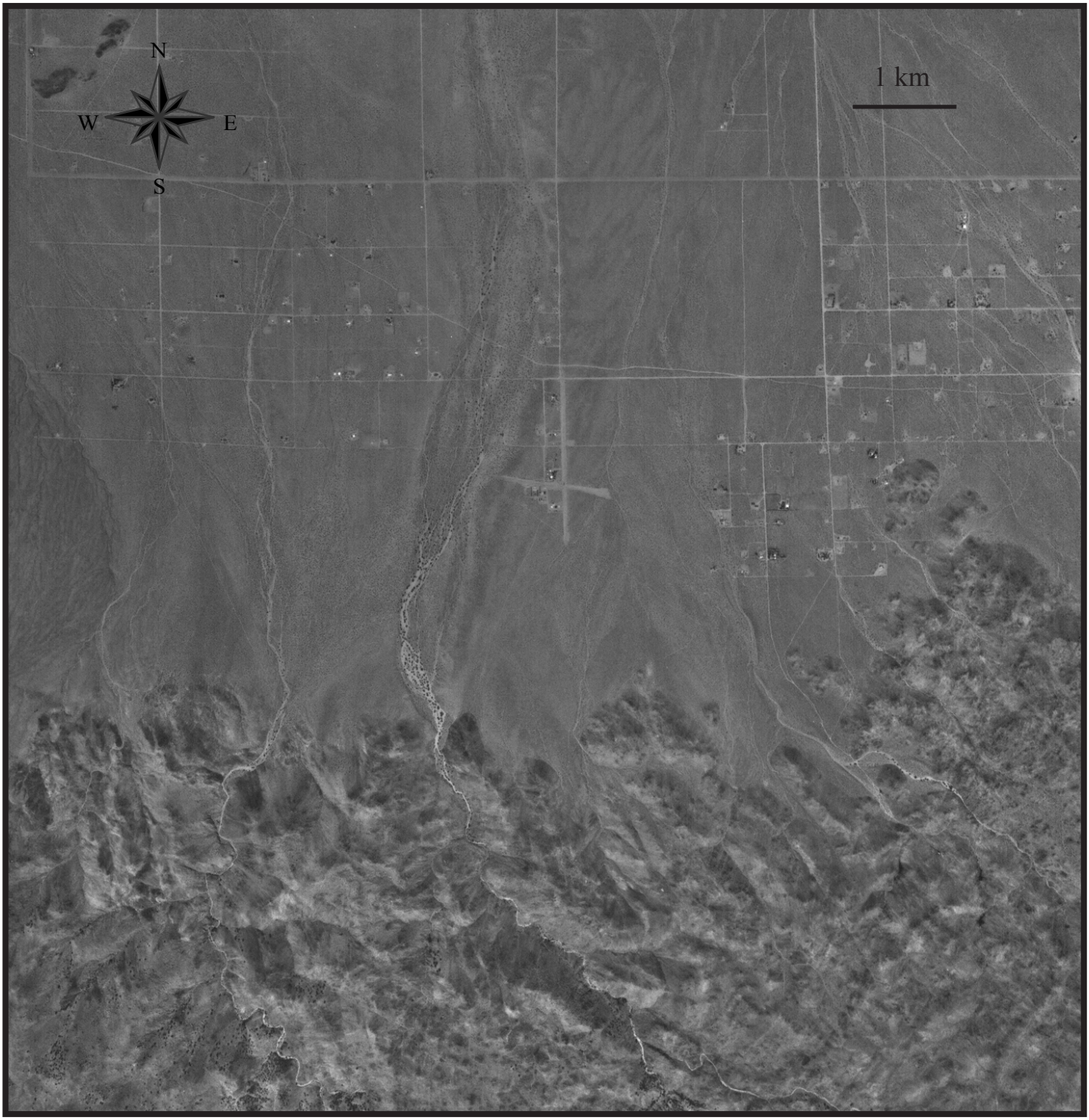

Figure 12

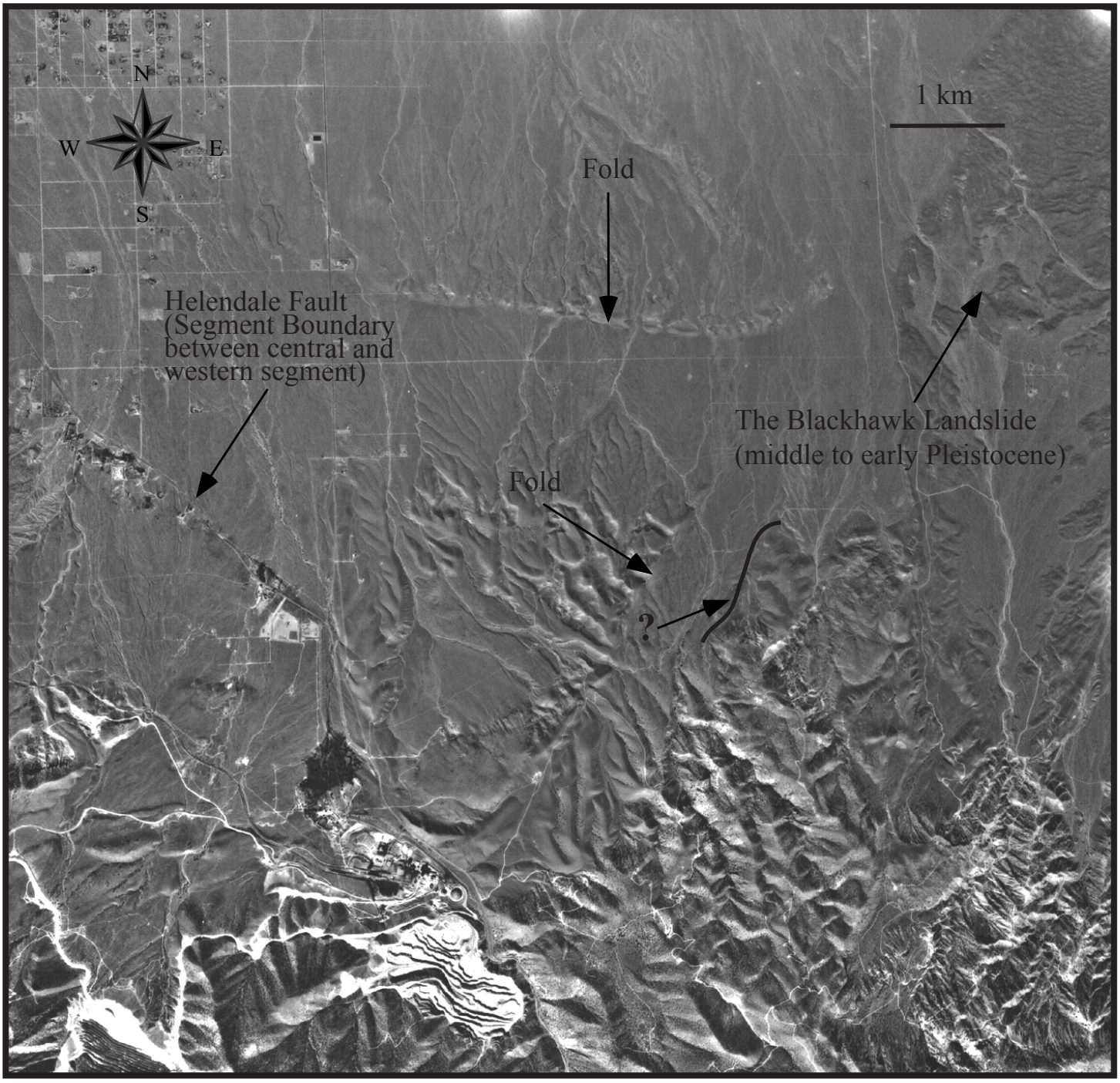
N
W
E
S
1 km
Fold
Helendale Fault
(Segment Boundary
between central and
western segment)
The Blackhawk Landslide
(middle to early Pleistocene)
Fold
?

Chapter 2: Paleoseismic Site Selection

2.1 Site Requirements

To further constrain interactions of these fault systems, we must establish the recent rupture history of the NFTS using paleoseismology. Most locations along the fault do not preserve an adequate record of young deformation. Thus, the first step is to identify candidate sites for paleoseismic investigation using detailed geomorphic analysis. Candidate sites must fit specific criteria in regards to age of sediment, proximity to an active drainage, and scarp size. For example, tall Pleistocene scarps (e.g. Figure 9) do not preserve evidence of the timing of the most recent (late Pleistocene or Holocene) rupture activity; recent events simply increase the separation of old horizons. Instead, ideal sites tend to occur at small scarps in young alluvium or at locations where faulted alluvium has been repeatedly buried.

We illustrate the evolutionary steps required of optimal excavation sites in block diagrams that detail a progression of erosional, depositional, and tectonic events (Figure 2). A simple alluvial environment, consisting of a modern channel and older depositional surface, is first offset by a single rupture event (panels A/B). The event produces a thrust scarp and colluvial wedge, as the hanging wall is pushed forward and collapses. The active channel then erodes through the scarp, thus maintaining its altitude above base level. In this case, the age of unit B (offset during the event) would place a maximum limit on the event age, while the age of unit A (overlies the eroded fault trace) would represent a minimum age. A second faulting event occurs in panel C. The preexisting colluvial wedge is offset and contributes to a higher prism of younger of colluvium. Because they are recycled material, these wedges do not constrain the timing of the event.

In time, more deposition occurs and the active channel widens its incision. New layer C buries the offset layer A, so that layer C constrains a minimum age and layer A constrains a maximum age of the second event. In the final stage a third event has broken layer C. Incision and renewed deposition of layer D provides the onlapping relationship required to bracket the age of this event. This erosion and deposition have not, however, completely covered or buried the offset layer C, so that a small scarp remains in the canyon. Through this series of erosional and depositional events, a chronosequence of fault ruptures has been preserved. But this record can only be accessed in the younger deposits of the incised canyon and active drainage, where a fault scarp may or may not be present. The higher, older scarp, which has experienced a prolonged depositional hiatus, is instead of little paleoseismic use. To identify candidate excavation sites along the 80-km long NFTS, we have compared field observations to this idealized scenario. The overarching requirement for young sites significantly limited the length of the fault that deserved consideration.

An additional consideration in selecting candidate excavation sites is local structural setting. One thing that must be avoided is close proximity of thrust scarps to strands of the ECSZ. Strike-slip fault ruptures commonly incorporate or terminate at off-fault secondary convergent or divergent deformation (e.g. Sieh et al., 1993). Evidence of recent thrusting near the ECSZ could thus be induced and not representative of the NFTS seismic cycle. It may also be possible for dextral motion on the ECSZ to induce rupture of a small strand of the NFTS (Figure 1, B). For example, if the Helendale fault ruptured, convergent strain would be transferred into the area east of the fault. The resulting stress

build-up could induce rupture of a small patch of the pre-existing weak NFTS as an aftershock. We wish to distinguish such coupled strike-slip/thrust events from independent thrust events. Eventually, we would like to constrain the rupture histories for all segments of the NFTS, but only the western segment is immune from ruptures induced by the ECSZ. The western segment is also the longest intact segment of the NFTS, containing no visible strands of the ECSZ. Therefore, we start with the western segment as the first step in quantifying the paleoseismic history of the NFTS.

2.2 Methods

Evaluating the degree of recent thrust activity and the geomorphic evolution of potential sites required airphoto mapping and field characterization. Preliminary observations of the entire NFTS were completed using a high-powered stereoscope to analyze 1:30000 airphotos. In the spring of 2000, Dr. James Spotila did a general overview of the region, collecting height data and soil samples from thrust scarps along the range front. The height data, rubification, and clay content were analyzed to determine the locations of the youngest landforms (Spotila and Anderson, 2000). This led to the concentration of further investigations on the western segment. The investigation included measuring scarp heights and making 1:12000 geomorphic maps based on both airphoto and field observations. The geomorphic map of the Marble Canyon site was produced as part of this study and the geomorphic map of the Furnace Canyon site was produced prior by Dr. James Spotila. Areas containing multiple thrust scarps were noted and channels were identified that incised the prominent Pleistocene scarps. Evidence of deposition of young alluvium where the scarp had been eroded and

the fault was possibly buried was then investigated. Relative ages of alluvium and channel locations at the Marble Canyon site were delineated on the geomorphic maps using 1:12000 topographic maps as an underlay. Mapping of the geomorphology was based on the alluvial ages determined by soil development, exposure of boulders, and sediment grain sizes. Scarp locations, channel locations and relative scarp heights within the younger alluvium were then used to determine areas that were candidate sites for paleoseismic excavation.

2.3 Observations

The analysis of airphotos and fieldwork led to the observation of three discrete segments along the NFTS (Figure 10). The landscape of the eastern segment appears subdued with the most poorly developed tectonic features and highest degree of soil development (Spotila and Anderson, 2000; Eppes et al., 2002). The relief of the bedrock escarpment associated with the NFTS tapers to zero in the eastern portion of the segment and there is no apparent evidence for thrust scarps or folds from the range front basin-ward. There are however, multiple strands of the ECSZ with recent historical seismicity proximal to the eastern segment (Sieh et al., 1993). The boundary between the eastern and central segments corresponds to the Old Woman Springs fault but is better defined as a transition into a zone where thrust scarps and folding become evident. Within the central segment, strands of the ECSZ occur in the footwall and hangingwall of the NFTS. Large folds and isolated scarps associated with the NFTS were located within the footwall. The Helendale fault serves as a boundary between the western and central segments. In the western segment, bedrock relief is greatest and there are numerous

discontinuous thrust scarps breaking late-Pleistocene fanglomerate with moderate soil development (Figures 8 and 14). However, visible traces of laterally offset faults did not occur within the segment. Pleistocene fault scarps occur along greater than 2/3 of the range front west of the Helendale Fault, whereas less than 1/3 of the range front contains scarps along segments to the east of the Helendale Fault. Therefore, due to the lack of evidence for recent thrust motion in the central and eastern segments and the dominance of thrust scarps in the western segment, the western segment became the focus of our investigation.

The boundary between the western and central segments may correspond to a change in structural setting directly related to the Helendale fault or the boundary may be defined based on a change in sediment provenance (Eppes et al., 2002; Spotila and Anderson, 2000). There is a possibility that the boundary between the central and western segments is directly related to the Helendale fault. Numerous discontinuous scarps with moderate soil development and sharp morphologies break fanglomerate to the west of the Helendale Fault, whereas to the east the scarps display a more subdued morphology with a greater degree of soil development (Spotila and Anderson, 2000). Folds are also found within both segments, dominating the landscape in the central segment. However, in the western segment the folds are eroded and associated with complex geomorphology. An alternate idea, associated with the changing surficial morphology, delineates a boundary west of the Helendale fault perpendicular to the bedrock escarpment and is based on sediment provenance. Granite-dominated sediments are found to the west of the boundary and limestone-dominated sediments are found to the east, within a central portion of the NFTS (Eppes et al., 2002) (Figure 8). Figure 15

illustrates landform evolution controlled by sediment type. The granite-derived sediments are easily eroded, therefore folds are not preserved and the core faults are exposed. However, the limestone-derived sediments develop a resistant petrocalcic horizon that preserves both the folds and fault scarps. Through time the resistant petrocalcic horizon will erode and expose the core faults within the folds similar to within the granite system, possibly explaining the lack of folds within the granite-dominated segments (Eppes et al., 2002).

A closer look at the western segment (Figure 16) reveals a concentration of young-looking discontinuous thrust scarps with sharp morphologies possibly late Pleistocene in age. Entrenched alluvial fans appear to be more incised toward the range front rather than basin-ward to the north, possibly indicating recent tilting and there is also a plentiful supply of sediment from the bedrock escarpment to the channel networks. These observations led to the identification of two promising sites (Marble Canyon [B, Figure 16] and Furnace Canyon [A, Figure 17]). In Figure 16, (C) denotes a large east-west trending Pleistocene scarp and (D) shows the continuation of the scarp east of an active channel. The box (B) outlines the area in which the old Pleistocene scarp has been eroded by the channel (E) and younger alluvium has been deposited. Figure 17 contains a large Pleistocene scarp (B and C) that has been eroded by active channel (D). The erosion of the scarp has been followed by the deposition of younger alluvium within the channel. The Marble Canyon and Furnace Canyon sites were both chosen as candidate locations for more detailed geomorphic investigation based on the removal of the Pleistocene scarps and deposition of young alluvium over the fault traces.

2.4 Site Selection

The detailed geomorphology maps from both sites (Marble Canyon and Furnace Canyon) were then used for comparison of the observed geomorphic setting to the idealized settings postulated in Figure 13. Figures 18 and 19 both reveal a large discontinuous thrust scarp that has been incised by a relatively young and active channel. The incised regions of the scarps have been replaced with the deposition of younger alluvium. The Furnace Canyon site is analogous to (panel C) in Figure 13, where a large Pleistocene scarp has formed from multiple tectonic events and the channel has eroded and deposited multiple layers over a broad width of the scarp. The site has no apparent ridge or surficial trace of the fault within the channel. Although the blanket of alluvium that buried the fault provides the advantage of constraining a minimum age, the lack of surficial evidence of the fault trace limits our ability to confidently choose an excavation location that would expose the fault.

The Marble Canyon site is analogous to (panel D) in Figure 13. Field observations revealed a small ridge, possibly a scarp, had formed in the deposits of young alluvium (Qa2, Figure 18) where the Pleistocene scarp had been removed. The subtle ridge was eroded at the base and we were unable to determine if it was an erosional feature or a scarp. Detailed field observations and comparisons to the idealized scenarios indicated the Marble Canyon site was the most promising candidate. The small ridge may indicate the surface location of the fault providing a visible confirmation of where to dig. The size of the trench required to expose the fault was also a consideration in determining the excavation site. The Furnace Canyon site had ~6-m of channel-fill that may bury the fault trace, whereas the Marble Canyon site had 0-1 m of possible fill,

therefore requiring a much smaller trench. Without burial of the fault trace at the Marble Canyon site we would not be able to constrain a minimum age of the most recent event. However, a maximum age, within the Holocene, would determine if the fault was active. Therefore we excavated at the Marble Canyon site.

Chapter 2: Figure Captions

Figure 13– Block diagrams illustrating the idealized geomorphic evolution of paleoseismic site along a thrust fault. A) Initial phase prior to deformation. B) First faulting event with development of a scarp, colluvial wedge, and incision of canyon. C) Second faulting event with continued erosion and deposition in canyon. D) Third faulting event with small scarp preserved in intermediate age alluvium of canyon. See text for additional details.

Figure 14–Photo of the bedrock escarpment of the western NFTS segment, taken looking south from the Mojave Desert. The escarpment has ~1 km relief. This area is located just west of the Helendale fault.

Figure 15–Eppes et al. (2002) model of topographic evolution. Scenario (A) illustrates the landscape maturation through repeated tectonic events and time. The horizons overlying the granite bedrock easily erode exposing the thrust fault, leaving no evidence of folding. Scenario (B) in limestone derived sediments develops a resistant petrocalcic horizon. The resistant horizon therefore preserves the fold and delays the exposure of the fault trace.

Figure 16–Airphoto close-up of Marble Canyon site within the western segment located just west of the Helendale Fault. Note the multiple discontinuous scarps with sharp prominent morphologies. Large box (A) represents the area of the 1:12000 geomorphic map (Figure 18). Box (B) illustrates the location of the paleoseismic excavation site. Scarps (C) and (D) point out the large Pleistocene thrust scarp to the west and to the east of channel (E). Channel

(E) has eroded the Pleistocene scarp and deposited younger alluvium over the fault trace.

Figure 17–Airphoto close-up of Furnace Canyon site within the western segment located just west of the Helendale Fault. This photo represents the area of the 1:12000 geomorphic map (Figure 19). Box (A) illustrates the location of the paleoseismic excavation site. Scarps (B) and (C) point out the large Pleistocene thrust scarp to the west and to the east of channel (D). Channel (D) has eroded the Pleistocene scarp and deposited younger alluvium over the fault trace.

Figure 18–1:12000 map of the Marble Canyon paleoseismic site. Four relative ages of alluvium are shown (Qa1-Qa4 [old]) based on mapping from 1:30000 airphotos magnified with a stereoscope. The fault scarp is shown as a heavy line, dashed where inferred and dotted where buried. (A) A very clear scarp traverses from west to east in the center region of the map. In the airphotos the scarp appears to diminish or become buried in the area within the box. (B) The box shows the location of the Marble Canyon Site. (C) This fault is buried at depth and may be responsible for the development of an asymmetrical fold just north of the inferred trace.

Figure 19–1:12000 map of the Furnace Canyon site in the area of multiple scarps within the western segment (Figure 10). The box represents the future paleoseismic trench site. Four relative ages of alluvium are shown (Qa1-Qa4 [old]) on the basis of soil development and degree of incision. The fault scarp is shown as a heavy line, dashed where inferred and dotted where buried. Two very clear

scarps occur at the north ends of Qa4 on west and Qa3 on east. The eastern scarp divides into two strands on the southwest, one being a rollover and the other a small subtle scarp inferred from airphotos. The NFTS becomes more complex to the east, where mining operations have disturbed the natural geomorphology.

Figure 13

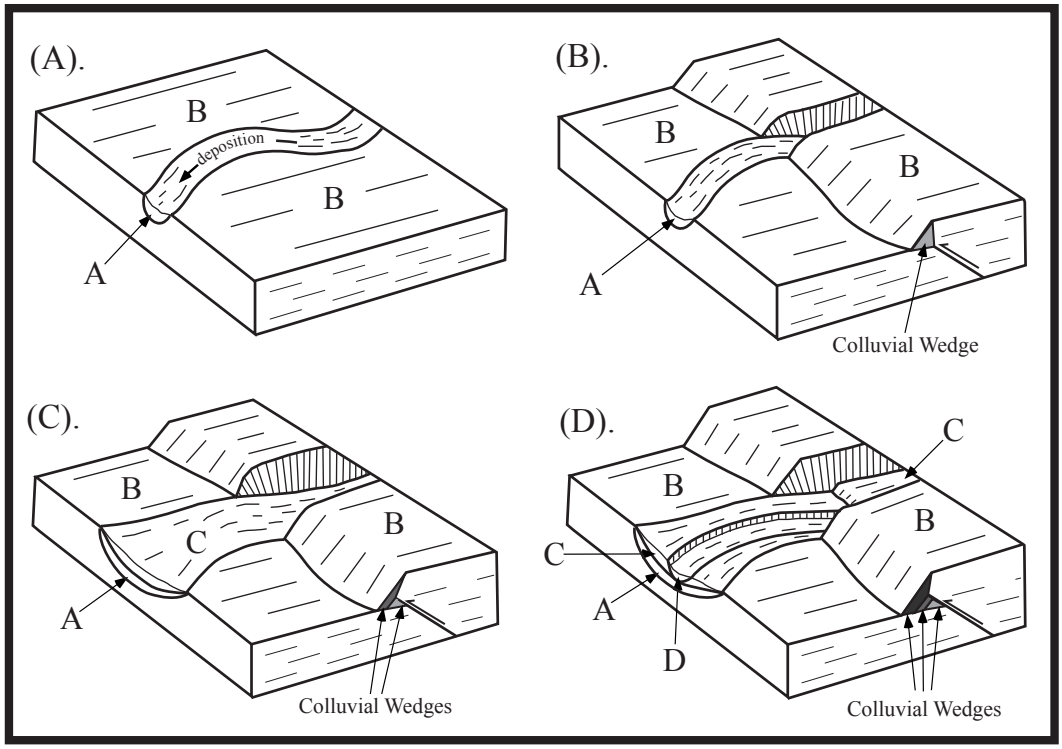
(A).
B
deposition
B
A
(B).
B
B
A
Colluvial Wedge
(C).
B
C
B
A
Colluvial Wedges
(D).
C
B
B
C
A
D
Colluvial Wedges

Figure 14

Figure 15

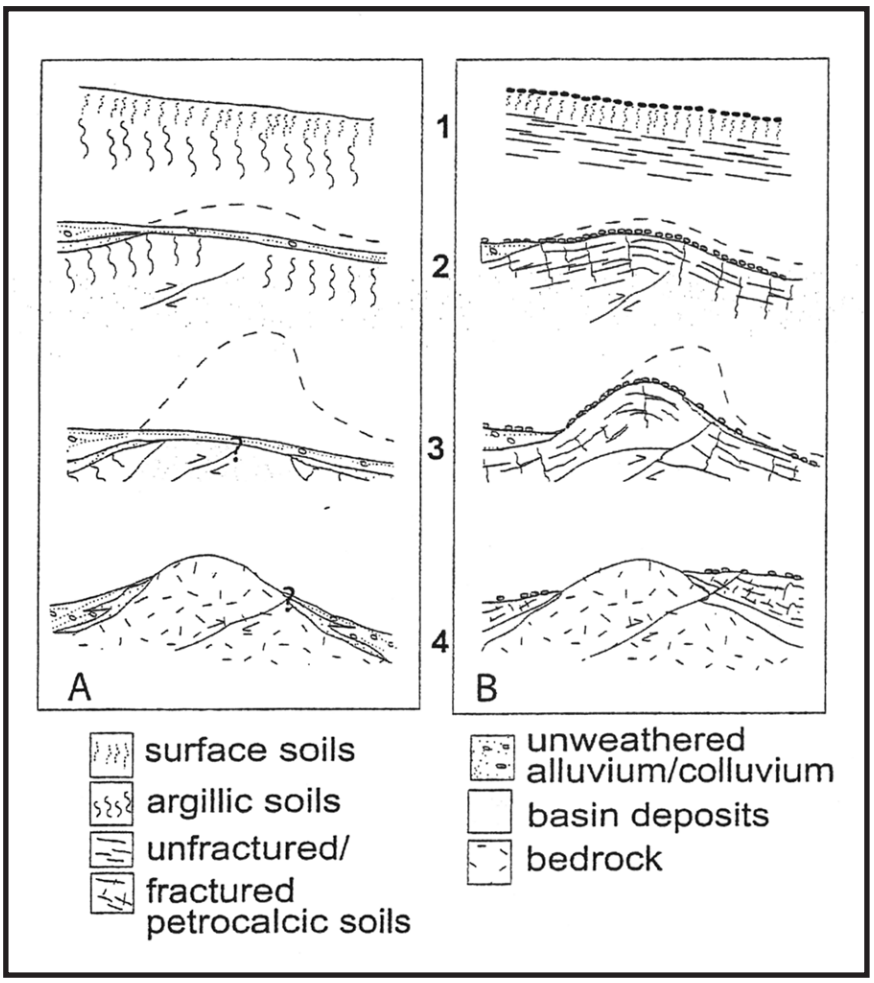
1
2
3
4
A
B
surface soils
argillic soils
unfractured/
fractured
petrocalcic soils
unweathered
alluvium/colluvium
basin deposits
bedrock

Figure 16

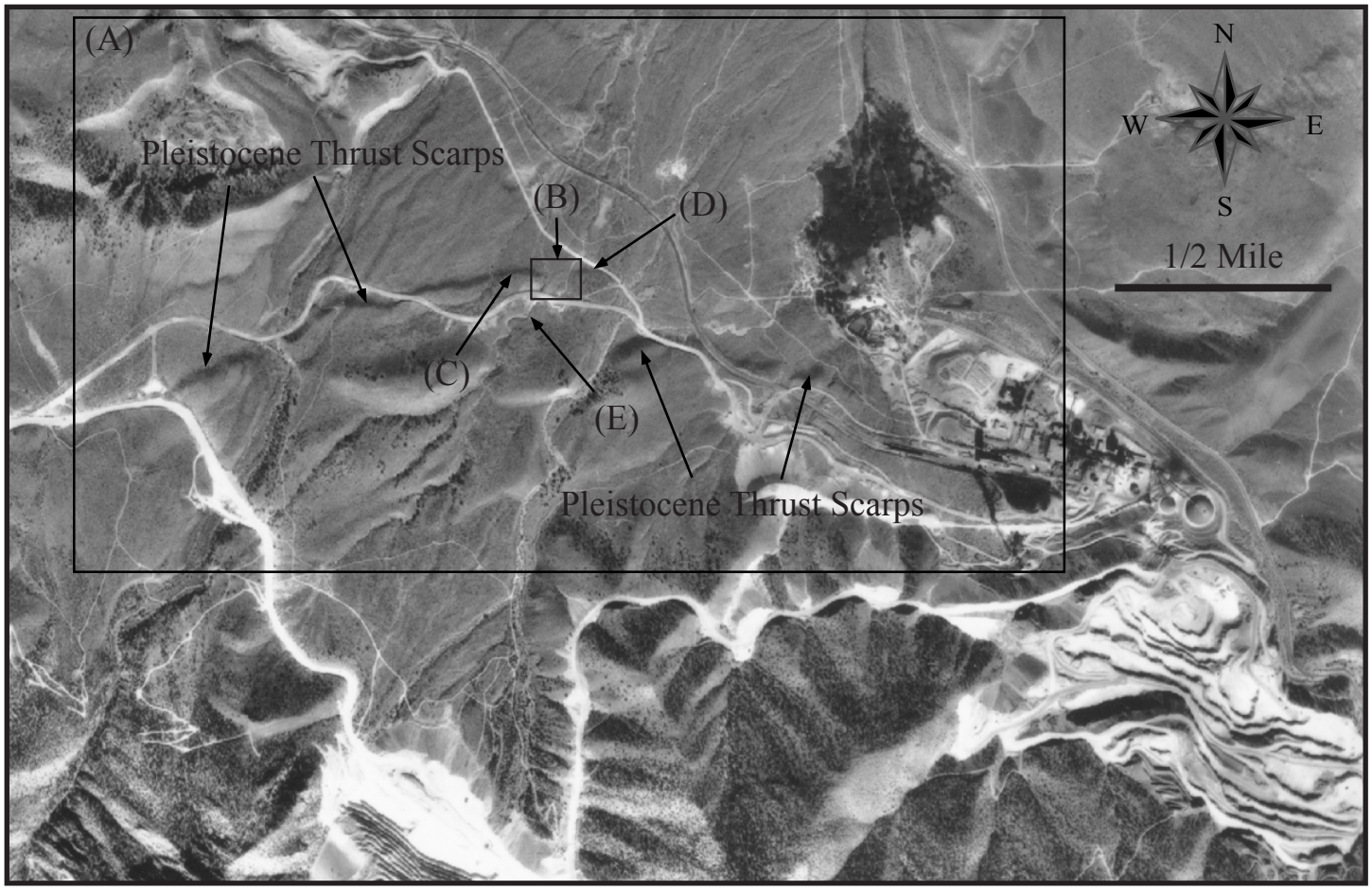
(A)
Pleistocene Thrust Scarps
(B)
(D)
(C)
(E)
Pleistocene Thrust Scarps
N
W
E
S
1/2 Mile

Figure 17

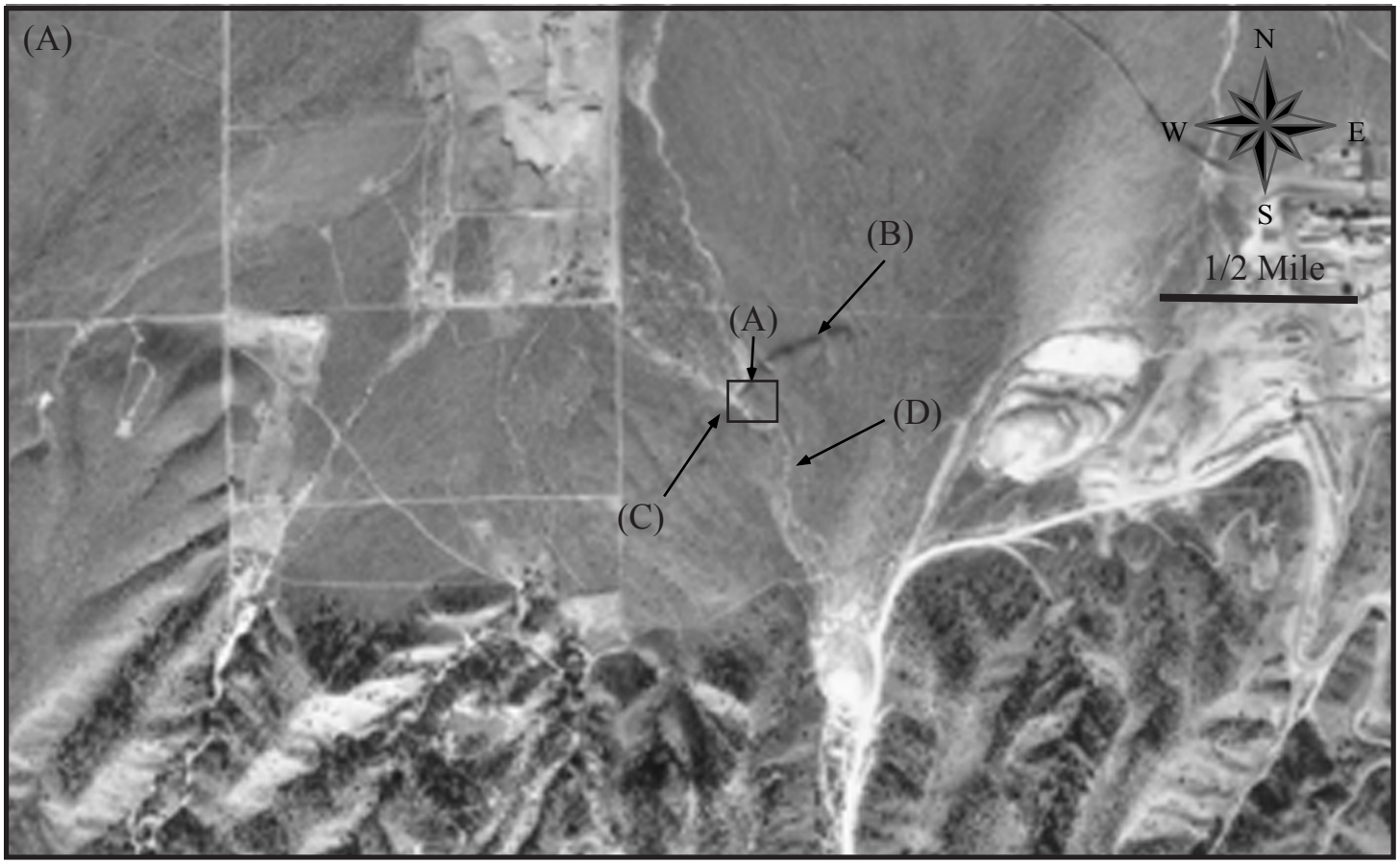

Figure 18

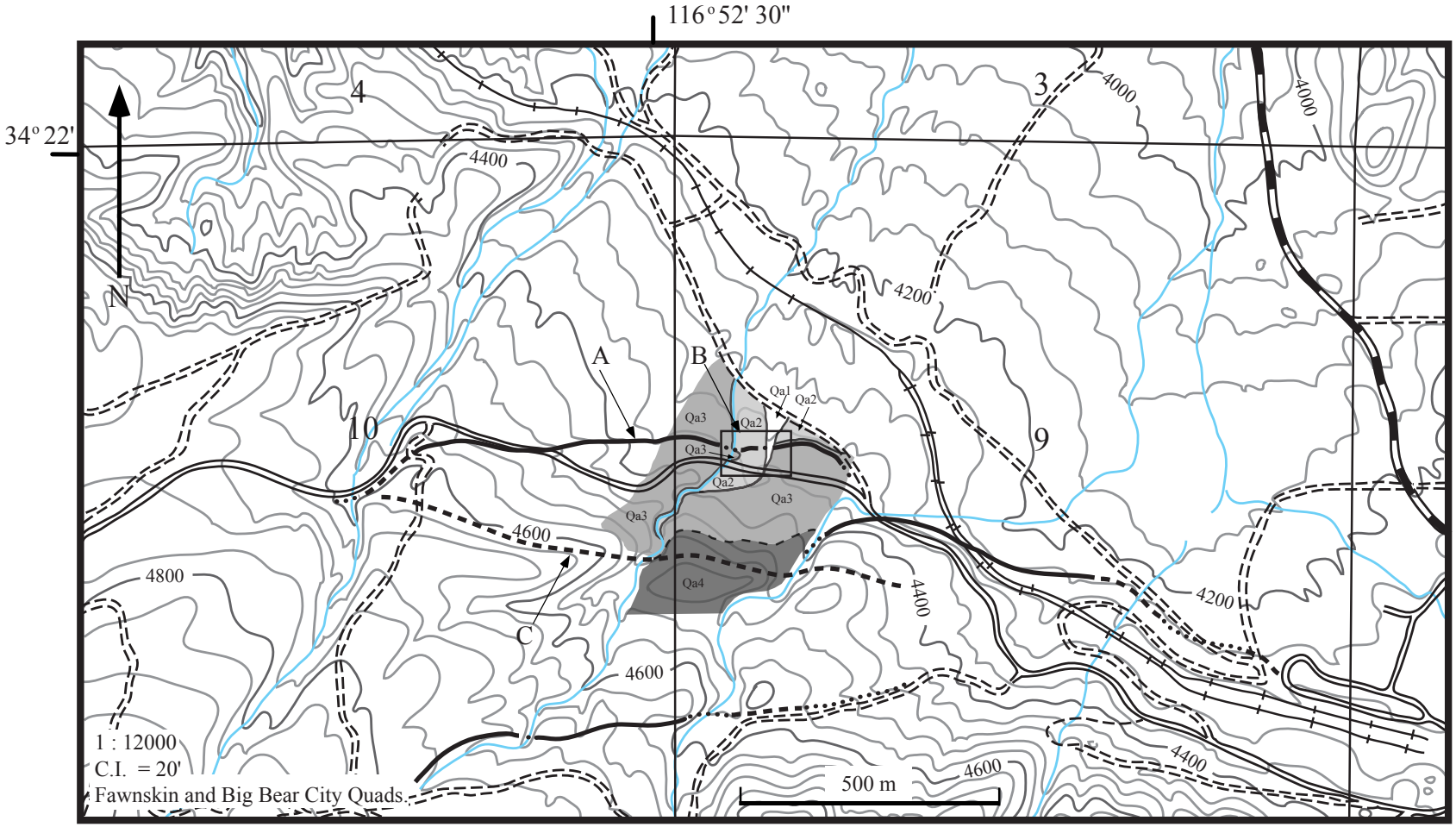
116° 52' 30"
34° 22'
N
4
3
10
9
A
B
C
4400
4000
4200
4600
4800
Qa1
Qa2
Qa3
Qa4
1 : 12000
C.I. = 20'
Fawnskin and Big Bear City Quads.
500 m

Figure 19

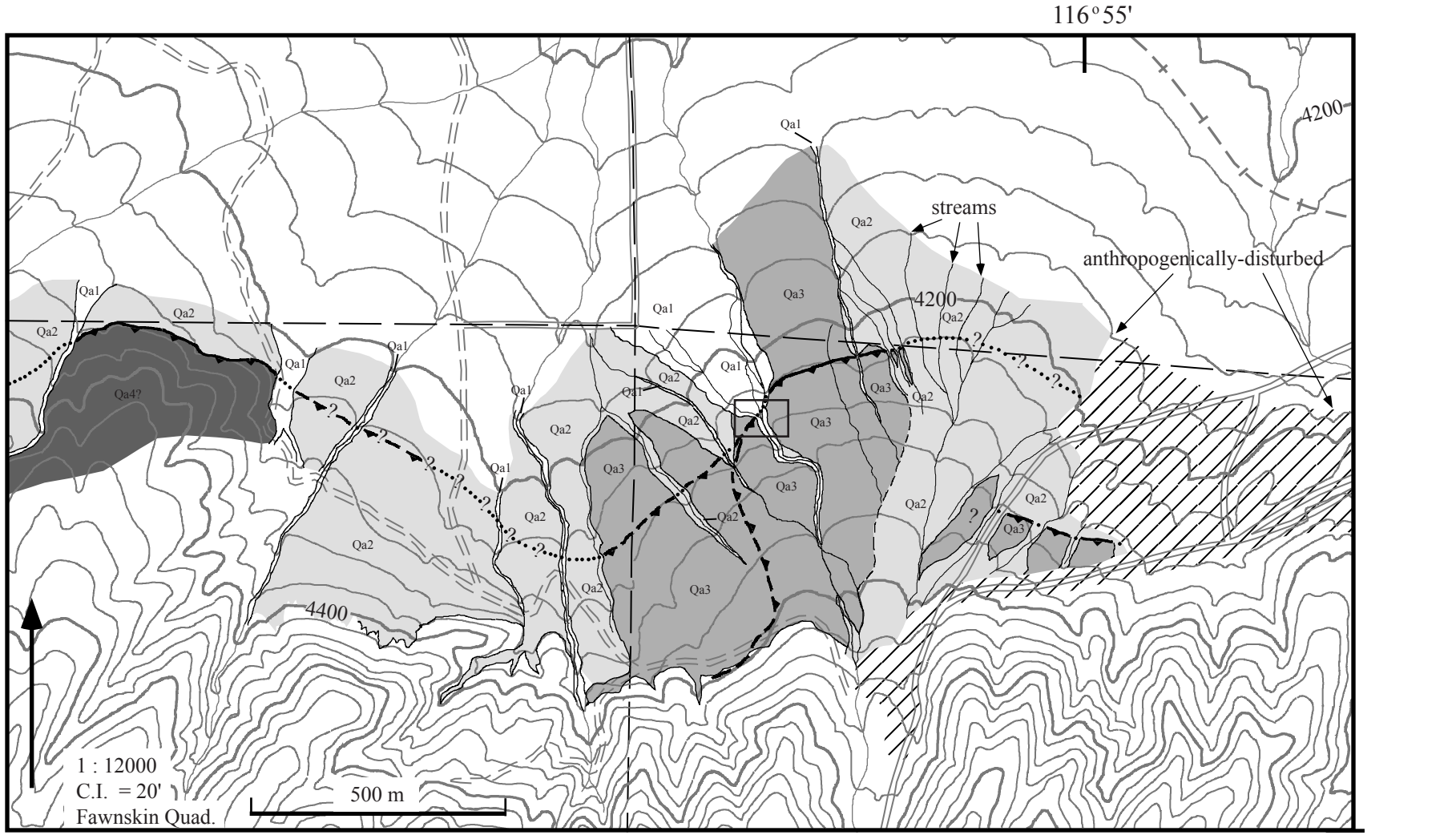
116° 55'
streams
anthropogenically-disturbed
4200
4400
Qa1
Qa2
Qa3
Qa4?
1 : 12000
C.I. = 20'
Fawnskin Quad.
500 m
34° 21.459'

Chapter 3: The Marble Canyon Site

3.1 Introduction

The Marble Canyon site provides an excellent opportunity to gather a first order constraint on the recent activity of the NFTS. Of the entire fault system, this site is the only one that has a potential fault scarp in Holocene (?) alluvium that is small enough to represent one event. The site provides an ideal location for paleoseismic investigation for several other reasons such as the small-scale size of the targeted landform (i.e. easy excavation), knowledge of where precisely to dig, and the unrestricted road and land access provided by the Mitsubishi Cement Corporation. The first step of our investigation at this site was to map onsite the detailed geomorphology of the alluvial deposits and fault scarps. A trench was then excavated, followed by detailed logging of the exposure and observation of the structure and stratigraphy.

3.2 Methods

A micro-geomorphic map of the area provides a detailed record of the geomorphic environment and refines the choice of where to excavate. A Leica TC-805 electronic total station was used to collect elevation points in order to create a detailed topographic map of the area with 50-cm contour intervals (Figure 20). A geospatially referenced base station (0 m; north, east, elevation) for the total station at coordinates 34°21.630’ N and 116°52.300’ W (based on GPS) was setup and marked with a stake. Three anchor points were surveyed and marked to provide spatial references for future surveys. The geomorphology, including relative age of alluvium, thrust scarps, and small-scale channels, were then mapped onto the topographic base. Relative redness of

soil, weathering and uplift of boulders, scarp heights, and channel incision were used to determine boundaries and mapable features.

Once mapped, the precise dimensions of the excavation could be selected. The excavation site was ~5 m wide (east-west) and ~20 m long (north-south), and proceeded to a depth of 3 ½ meters. Once the precise location was determined, a D-8 bulldozer (provided by Mitsubishi Cement Corporation) was used to excavate the site (Figure 21). A one-meter by one-meter square string grid was constructed over the trench face of to guide logging the trench. Vertical grid lines were tied to stakes at the surface and swung freely with weights tied to the ends to ensure vertical orientation. Horizontal lines were leveled using a laser eye-level and tied to stakes at their ends. Stratigraphy, soils, and the orientation and character of the fault were identified and fully described. Soil samples from each horizon and material for age dating were collected for analysis.

The trench wall was logged by hand at a scale of 1:10 on graph paper with one square equivalent to ~5 cm^2 (Figure 22). All contacts and clasts greater than 2 cm diameter were drawn precisely. Sand lenses, carbonate accumulations, and Fe-oxide accumulations were schematically represented by patterns. The purpose of the detailed log was to preserve an accurate record of the sedimentologic and deformation features observed. Dr. James Spotila and I logged the individual grid panels independently, which were later combined for verification. A photo log was used to aid in the reconstruction of the log and for an accurate record of observations.

The trench log was digitized and combined into one coherent diagram. Panels were scanned using Adobe Photoshop software and placed into an Adobe Illustrator environment for concatenation. Clasts smaller than ~5 cm were eliminated from the

digitized version of the log. Patterns were created to represent the smaller clasts and matrix material.

3.3 Detailed Geomorphic Characterization

The detailed geomorphic-topographic map illustrates the geomorphic setting of the Marble Canyon site (Figure 20). Four relative ages of alluvium were defined, which reveal the evolution of the site. The limestone-dominated alluvial deposits, derived from the bedrock escarpment, were deposited as alluvial fans with granite clasts the size of large boulders. Two apparent scarps of different deformation history cut the alluvium.

The oldest alluvium is designated Qa4. The Qa4 surface is comprised of large granite boulders ranging in size up to 80 cm in diameter surrounded by alluvium that is darker and more red than the surrounding units. Small channels erode this uplifted surface and in places there are colluvium deposits composed of Qa4 material (Figure 20). Qa4 is separated from the Qa3 by a large, sharp scarp (4.83 m high) of probable late Pleistocene age (Figures 23a and 24). The scarp is missing for ~100 m west of Qa4, but emerges further west (Figure 16). In this stretch, Qa4 has been eroded and replaced by younger alluvium (Qa3). This younger alluvium differs in character from Qa4. Qa3 is mostly limestone-derived and contains almost no large granite boulders. The overall grainsize of Qa3 is finer and more sorted. The difference in composition from Qa4 results from the mixed limestone-granite bedrock of the catchment, and that different sub-basins may have been the dominant source of sediment at different stages. The dashed line surfaces illustrate the Qa3 surface is incised by small channels (Figure 20). One of these is quite large. A stream has incised the Qa3-Qa4 contact and deposited Qa1

and Qa2. The Qa1 and Qa2 deposits represent modern age (<100 yrs) deposition, partly due to erosion of the road and drainage perturbation upstream (Figure 16). They consist of fine to medium unconsolidated sands, gray in color with no soil development.

The break in Qa4 and burial by Qa3 provides the young geomorphic setting required for good paleoseismic sites. Within Qa3 a small, micro-scale ridge occurs along strike of the scarp in Qa4. A topographic profile reveals that this ridge appears scarp-like in form and is 1.2 m high (Figure 23b and 25). It is subdued and rounded, however, due to erosion at the base. The map also shows how the feature trends more southwesterly than east-west like the main scarp (Figures 16 and 20). In places, young channels have cut into this feature. It also becomes smaller and more poorly defined to the southwest. It is thus unclear whether the alluvial ridge is a degraded scarp or purely erosional in origin.

The incision of the Pleistocene scarp and deposition of younger alluvium at the Marble Canyon site are analogous to the required geomorphic evolution defined in Figure 13. The alignment of the small ridge with the older scarps suggests that it is a younger scarp. If true, this micro-ridge would be an ideal location to excavate to identify the most recent rupture event. However, until excavated or imaged with a geophysical imaging technique, we could not be certain if deformation or erosion had produced it.

3.4 Excavation Results

The trench location (shaded gray, Figure 20) was chosen perpendicular to and across the small alluvial ridge. The exposure revealed well-defined alluvial layers and paleosols offset by a simple, low-angle fault plane dipping towards the south. Figure 26

is a photo of the west-wall of the trench, taken immediately following the removal of the bulldozer. We logged the exposure in detail (e.g. Figure 22), compiled the individual log sections, and produced a digitized version (Figure 27).

The gravel layers consist of poorly cemented, well-sorted, clast-supported channel deposits with marble clasts up to boulder size. The color of the layers ranges from gray to light brown, depending on clast color and ratio of marble clasts to CaCO3 sand matrix. Localized sand lenses, with original bedding intact, occur throughout the gravel layers. The depositional direction of the deposits was not perfectly perpendicular to the trench, and therefore thickness variations are common. This pinching and swelling is common in channelized alluvial environments. There has also been minor erosion of layers at the expense of young alluvium, such as the removal of part of FW2. In general, however, the stratigraphy is simple, with one nearly flat-lying layer on top of the other.

The degree of soil development in these layers is generally poor, although two paleosols appear prominent in the exposure (Figure 26). Soil horizons are labeled on the trench log and illustrated in a photograph (Figures 27 and 28), based on the observations and interpretations of M. Eppes (written comm., 2001) and our own field observations. The A-horizon is the loamy, organic or biologic layer, rich in organic material and heavily bioturbated. The Bw-horizon is a weakly developed illuvial layer with a sandy loam texture and subangular blocky soil structure with 30% gravel. The Bwk-horizon was a loamy sand texture with subangular blocky soil structure that was poorly cemented and matrix supported with 50% gravel. The matrix of the horizon was primarily composed of carbonate. The “k” denotes the accumulation of eluvial carbonate in all of the layers below the uppermost Bw-horizon. Three gravel layers are denoted as Ck-

horizons, because of the minimal evidence of carbonate accumulation, clay development, or soil structure. The clasts within the gravel layers are well rounded, well sorted, and clast supported with over 70% gravel and random sand lenses. The gravel layers are cemented, however they break apart easily with an awl. Two prominent calcic Bk horizons (Bkb and Bkb2) are present in the hangingwall and footwall of the trench. The two layers have a higher degree of soil development with an angular block texture and consist of angular to subangular gravel in a silt to sand-size matrix. They are poorly sorted and matrix supported, composed primarily of carbonate sand and clasts. Bkb is weakly developed and easily penetrated with an awl due to lack of cementation. Bkb2, however, is moderately cemented and hard to penetrate with the awl. The primary color of the layer is white, however water is unable to penetrate the more indurated horizon and therefore red oxidation films have developed at the top of the layer.

The paleosols (Bkb and Bkb2) clearly correlate across the fault (HW2 to FW2 and HW4 to FW4)(Figure 27 and 29). The entire stratigraphy of the footwall and hangingwall similarly define the offset along the fault. Thickness variations across the fault are because the depositional direction is not perpendicular to the fault and the slip direction may not be parallel to the trench. Layers also thicken in a downstream direction. One layer from the hangingwall is missing from the footwall. This may be because it has been eroded from the footwall by a channel that runs north of the scarp (Figure 20). In this case, the height of the apparent scarp would be greater than the actual offset of the layers. Given that layer FW5 is thicker than HW5, it is also possible that the correlative Bwk horizon was incorporated into colluvium of the footwall.

The uppermost layer in the trench does not appear to be offset. HF7 is where the active soil forming processes are taking place, heavily affected by bioturbation and eolian flux. Both layers are weakly developed and continuous across the length of the trench. This layer is thicker within the footwall, this may be due to overthrust and collapse of material associated with ground rupture. However, there is no clear colluvial wedge. A wedge could be unclear due to the gradational nature of the boundary between HF7 and FW5. Because this layer may be partly colluvial, dating its organic fraction would not have provided a meaningful age for a geologic event. This implies there is no overlying deposit that could provide a minimum age of the faulting. Exactly where the fault terminates is not clear. A secondary excavation of HW4, HW 5, FW5, and HF7 was completed by hand to search for the fault (Figure 30). However, as soil development decreased toward the top of the trench, the degree of cementation decreased, making the uppermost layers very loose and friable. If these layers had ruptured, the fault trace may not have been preserved in the loose sandy material. Although the uppermost gravel (G1, HW5/FW5) did not preserve the fault trace, it has clearly been offset (Figures 26 and 27). Because the layer is juxtaposed against itself, however, no clear break or color contrast is evident.

The single, prominent fault trace shows no evidence of secondary mineralization, preferred alignment of cobbles, or slickensides (Figure 29). This clean break suggests it was formed during one rupture event. Based on the correlation between HW 2 and FW 2 the observed offset is ~1.65 m of throw. The vertical separation of Bkb (HW4-FW4) is ~25% less than Bkb2 (HW2-FW2). This does not indicate more than one event, however, for there is no evidence of a colluvial wedge or a ground surface between the

paleosols. The difference in apparent separation is probably due to variations in layer thickness and orientation. The orientation of the fault, measured with a Brunton compass, is N85°W ± 1° with a true dip of 23° towards the south.

3.5 Age Constraints

An estimate of the maximum age for this rupture event can be constrained by dating the youngest faulted unit. Soil profile characterization can provide an age estimate associated with the soil development of the entire profile. The weak degree of soil development implies a fairly young age. The paleosols are stage I petrocalcic (K) horizons and the active soil (Bw + A) has minimal pedogenic clay and redness (10YR5/3). The development of the entire soil profile is estimated to have taken 20 Ka ± 10 Ka (Eppes, pers. comm.).

Accelerator mass spectrometry radiocarbon dating provides an additional age constraint. This technique offers precision of ±10 years (Sieh et al., 1989). Detrital charcoal was found in four locations in the excavation (Figure 27), but all contained less carbon than required for dating (~0.3 micrograms of carbon, or ~0.5 milligrams of charcoal, required). Instead a C-14 age was measured on a bulk sediment sample of a sand lens in the basal gravel layer of the hangingwall (Figure 27). The sediment was sieved to less than 180 microns and pretreated to remove non-detrital contaminants (roothairs and macrofossils were removed by hand; repeated acid washes dissolved all carbonate, fulvic acids, and humic acids) (Beta Analytic Inc., written communication, 2001). The remaining 4.2 g of sediment was combusted to yield 14 cc of CO2. The resulting radiocarbon age was 9630 ± 50 BP, which corrects to 9710 +/- 50 BP when the

carbon fractionation of the organic material is taken into consideration. The age can also be calibrated, based on a chronosequence established from tree rings and coral dating. The intercept for the Pretoria calibration (Talma and Vogel, 1993; Stuiver, M., et al., 1998) gives an age of 9220 BC (11220 yr BP) (Beta Analytical, written comm., 2001). The 1-sigma range in the calibrated age result is 9230-9180 BC. The 2-sigma error bars allow a greater age range, due to the nonlinear nature of the calibration curve (Figure 31). The error associated with the age estimates is related to the analytical precision and calibration accuracy, not the actual depositional age. We cannot quantify the uncertainty of whether all carbon within the sample was of the same age. However, given the lack of evidence for groundwater fluctuations, soil reworking, or vertical transfer of material and humic/fulvic acids, the age should be representative of the basal gravel layer.

3.6 Discussion

We have identified a small offset and scarp along a strand of the NFTS, which we interpret to have been created during one rupture event. By dating the depositional history of an offset layer, we established a maximum age for the event of 9220 BC. Given that the soil estimate and C-14 age overlap and the soil development and deposition of over 1 1/2 m of sediment predate the rupture, we are confident the observed rupture occurred within the Holocene (past 10 Ka). A minimum age for the rupture event could not be determined at this site. A second paleoseismic site is still needed within the western segment, not only to constrain the minimum age of the most recent event but also to expose multiple events and determine a recurrence interval. However, previous

suggestions that the fault is inactive are wrong (Sadler, 1982: Meisling and Weldon, 1989). This has several implications.

The amount of offset (1.7 m) is typical for ruptures that are 20-40 km long and M>7, based on empirical relationships (Wells and Coppersmith, 1994). Since active, the NFTS may also be playing a role in the recurrence of events along the San Andreas Fault to the south. The lack of historical seismicity along the segment of the San Andreas may be due to increased normal stresses associated with the NFTS. However, without knowing the recurrence interval for the NFTS, we cannot determine what stage of the seismic cycle it is in. Therefore we cannot determine the immediate influence of the NFTS on the San Andreas.

This also confirms that the two opposing fault systems (NFTS and ECSZ) are coactive. From comparison of the findings of this study to the four scenarios in the segmentation diagrams (Figure 1), we can only exclude scenario 4, because neither fault system is extinct (yet). Without the minimum age, we cannot compare the timing of the observed event to events on the ECSZ. Therefore we do not know if one fault triggers the rupture of the other or if the ECSZ behaves as a segment boundary. Without constraints on the central and eastern segments we also cannot rule out the possibility that the NFTS could rupture its entire length. Further investigation of the timing and rupture characteristics of all three segments of the NFTS is needed to develop a full understanding of the relationship between earthquake timing, magnitude, and the role of the ECSZ along the entire NFTS.

Chapter 3: Figure Captions

Figure 20–Detailed geomorphic map indicating four relative ages of alluvium (Qa1-Qa4 [old]). A prominent Pleistocene scarp occurs in the Qa4 alluvium east of the active drainage. A subtle ridge on the west of the drainage in younger Qa3 was interpreted as a possible scarp, until verified by later excavation (box denotes trench) and GPR profile (along blue dots).

Figure 21–(A) D-8 bulldozer provided by Mitsubishi Cement Corporation prior to dig. (B) D-8 bulldozer within trench. The trench was ~3 ½ m deep and took ~30 minutes to excavate.

Figure 22–Example of detailed hand-drawn log of the west wall of trench at Marble Canyon site. A 1-m by 1-m square string grid was placed over the west wall of the trench. The square panels were then logged in detail at a scale of 1:10; each square equivalent to ~5 cm^3. All clasts over 2 cm were drawn spatially accurate. Bedding, sand lenses, and areas of oxidation were artistically represented and locations where material was collected were clearly marked.

Figure 23-(A) Profile of the Pleistocene scarp on the east side of the active channel (Figure 20). (B) Profile of small ridge, interpreted as a younger fault scarp. The location of the line is denoted by blue dots in Figure 20.

Figure 24–Photo of Pleistocene scarp face. The upper surface of the scarp is Qa4 alluvium, with large granite boulders and darker and slightly redder soil than the surrounding units that has been uplifted and eroded. The scarp defines the boundary between the Qa4 and Qa3. Qa3 below the scarp is limestone dominated with rare granite clasts.

Figure 25–Photo of excavation site prior to the dig. The active channel that has cut through the Pleistocene scarps is in the foreground. The person is standing at the small ridge. The ridge is subdued and rounded due to erosion.

Figure 26–West wall of the trench, immediately following the removal of the bulldozer. Arrows indicate relative motion. HW2 and HW3 correlate to FW2 and FW3, respectively.

Figure 27-Digitized trench log of the west wall exposure at the Marble Canyon site. Scale is indicated by the 1-m grid overlaid on the log. Heavy lines were drawn to denote all boundaries of the trench (top and bottom of the trench, stratigraphic layers, and fault traces), dashed lines were used when the boundaries were not clear or needed to be inferred. A slash pattern was used for some portions of the trench where the material was disagregated and collapsed or was removed to form a ledge. Color indicates three paleosol layers in the hangingwall (HW2, HW4, and HW6) and two corresponding layers in the footwall (FW2, FW4). Coarse gravel units are located between the paleosols with original bedding intact. HF7 is continuous over the entire exposure and represents the region of modern soil processes. It is not clear how far the fault cuts, as the region at location 2 consists of disagregated material in which no fault can be observed. A bulk sample was taken from location 1 for radiocarbon dating.

Figure 28-Soil profile on the southern end of the excavation. Two prominent carbonate-rich paleosols (Bkb and Bkb2) with angular to subangular clasts that are

matrix supported separate gravel layers that are clast supported with rounded clasts.

Figure 29-Close-up photo of the fault exposure on the west wall of the Marble Canyon trench. The bar indicates 1.65 m of throw associated with the offset of the white petrocalcic horizon (Bkb2).

Figure 30-Secondary excavation. The dashed line represents the area excavated by hand. This excavation extended the west wall ~4 feet further west from the original wall. The disagregated material did not preserve the trace of the fault.

Figure 31-Calibration chart for AMS C-14 dating. Fluctuations of C-13/C-12 ratios in the atmosphere can cause fluctuations in the calibration curve. The intercept for this calibration indicated an age of 9220 BC (9230-9180 BC, 1 sigma range; or 9140-9250 BC and 8980-8930 BC, 2 sigma range) (Beta Analytical, written comm., 2001). Therefore the age from the bulk sample indicates deposition of the basal gravel layer to be ~1 ka pre-Holocene.

Figure 20

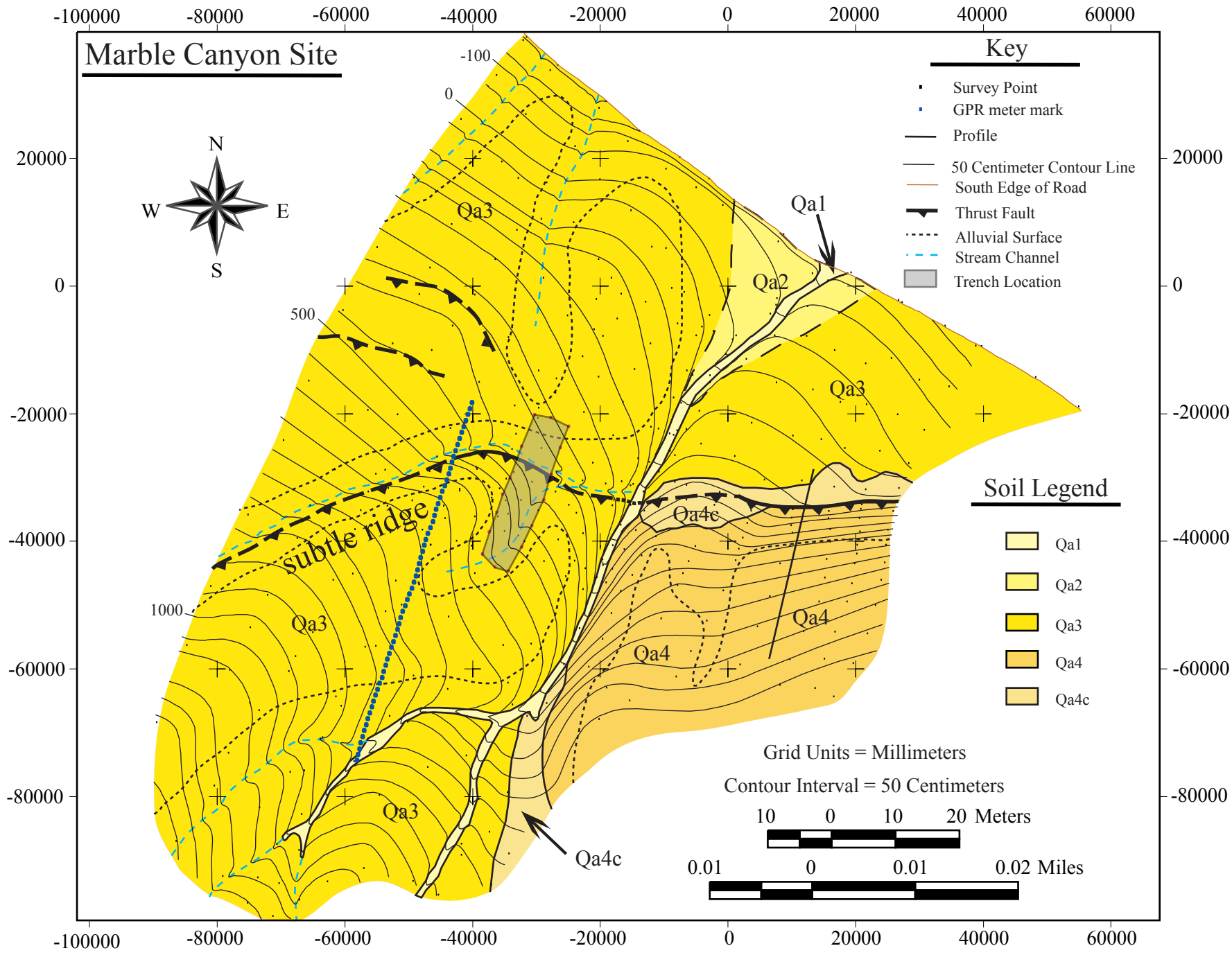
Marble Canyon Site
Key
Survey Point
GPR meter mark
Profile
50 Centimeter Contour Line
South Edge of Road
Thrust Fault
Alluvial Surface
Stream Channel
Trench Location
N
W
E
S
-100000
-80000
-60000
-40000
-20000
0
20000
40000
60000
20000
0
-20000
-40000
-60000
-80000
-100
0
500
1000
Qa1
Qa2
Qa3
Qa4
Qa4c
subtle ridge
Soil Legend
Qa1
Qa2
Qa3
Qa4
Qa4c
Grid Units = Millimeters
Contour Interval = 50 Centimeters
10 0 10 20 Meters
0.01 0 0.01 0.02 Miles

Figure 21

Figure 22

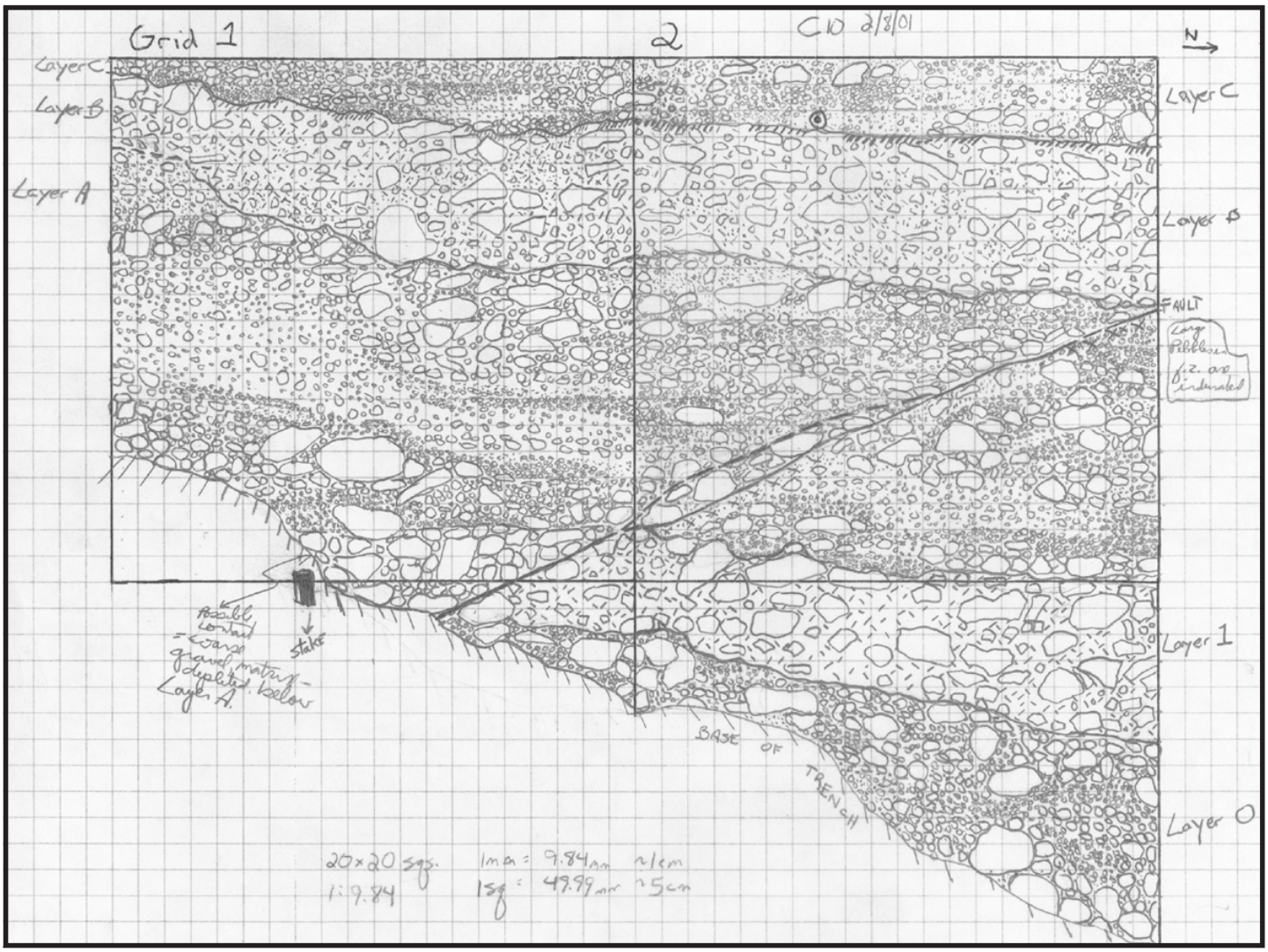
Grid 1
2
CW 2/8/01
N
Layer C
Layer B
Layer A
Layer C
Layer B
FAULT
Large Pebbles (i.e. are indurated)
Possible contact - coarse gravel material - depleted below Layer A
stake
Layer 1
BASE OF TRENCH
Layer 0
20×20 sqs.
1:9.84
1 sq = 9.84 mm ≈ 1 cm
1 sq = 49.99 mm ≈ 5 cm

Figure 23

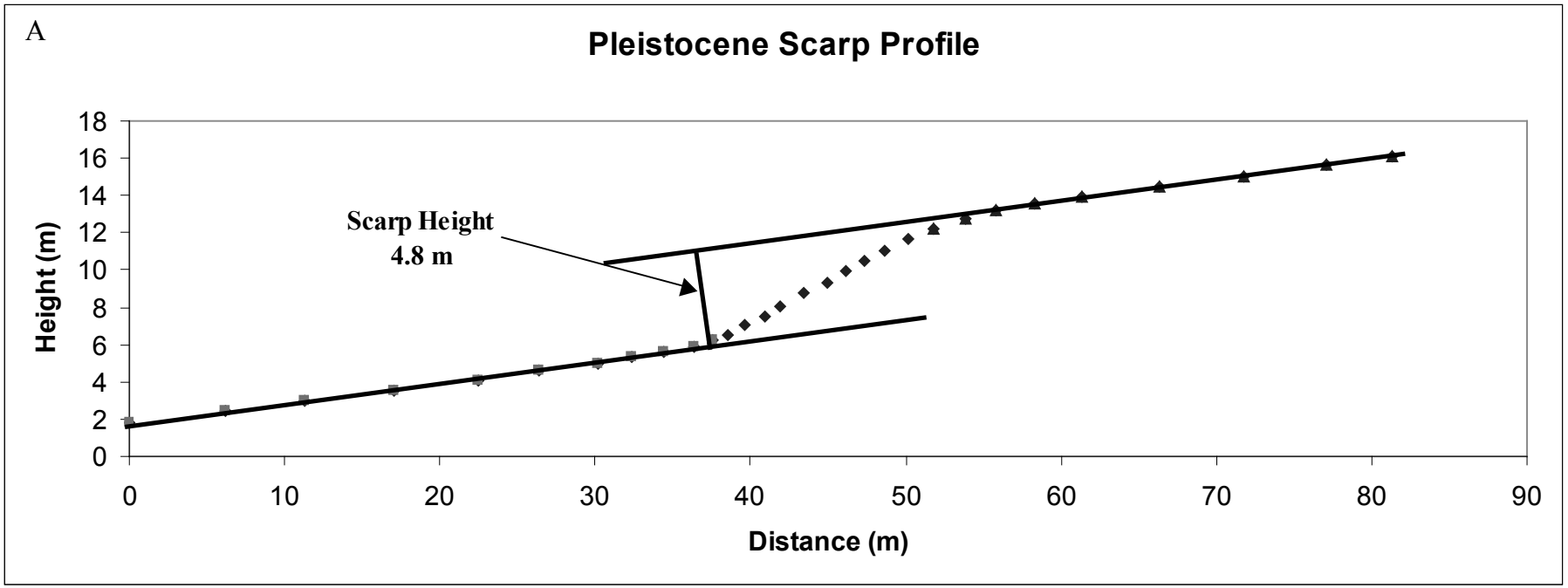
A
Pleistocene Scarp Profile
Scarp Height
4.8 m
Height (m)
Distance (m)
0
2
4
6
8
10
12
14
16
18
0
10
20
30
40
50
60
70
80
90

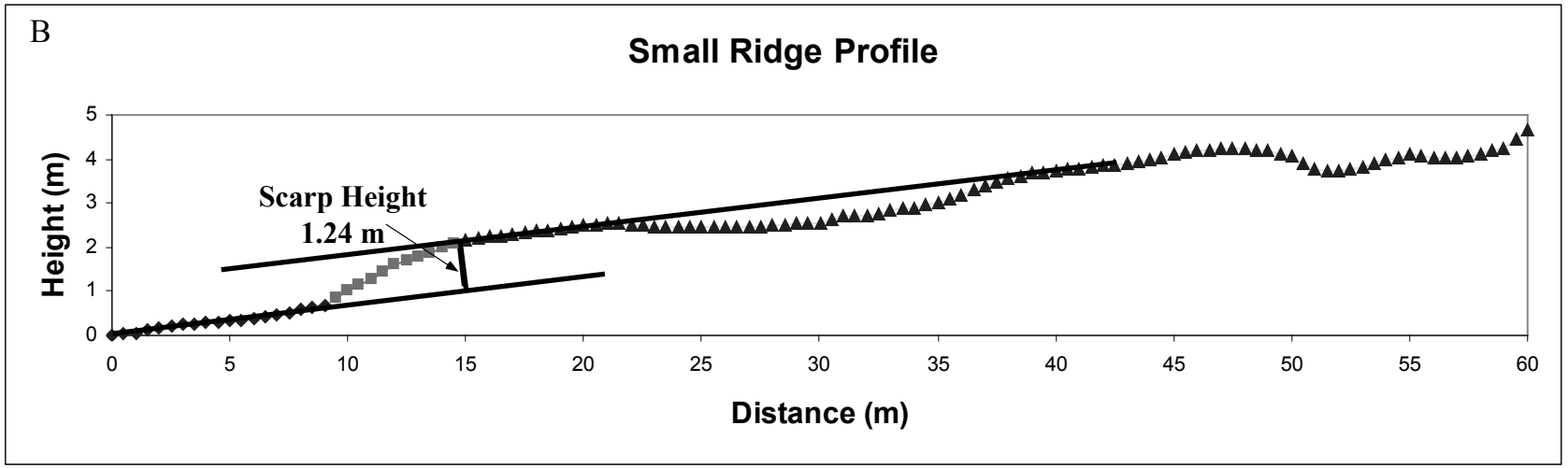
B
Small Ridge Profile
Scarp Height
1.24 m
Height (m)
Distance (m)
0
1
2
3
4
5
0
5
10
15
20
25
30
35
40
45
50
55
60

Figure 24

Figure 25

Figure 26

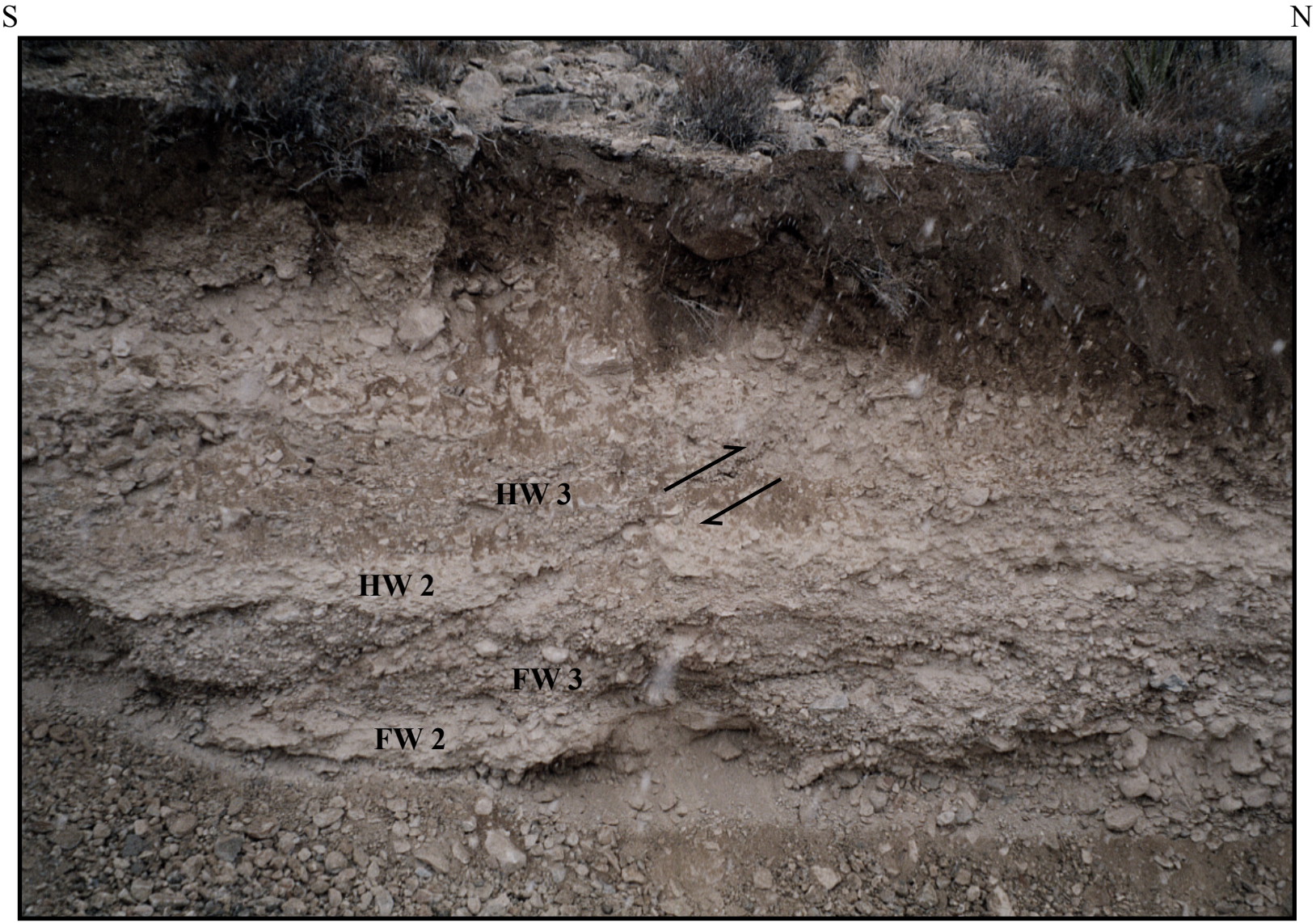

Figure 27

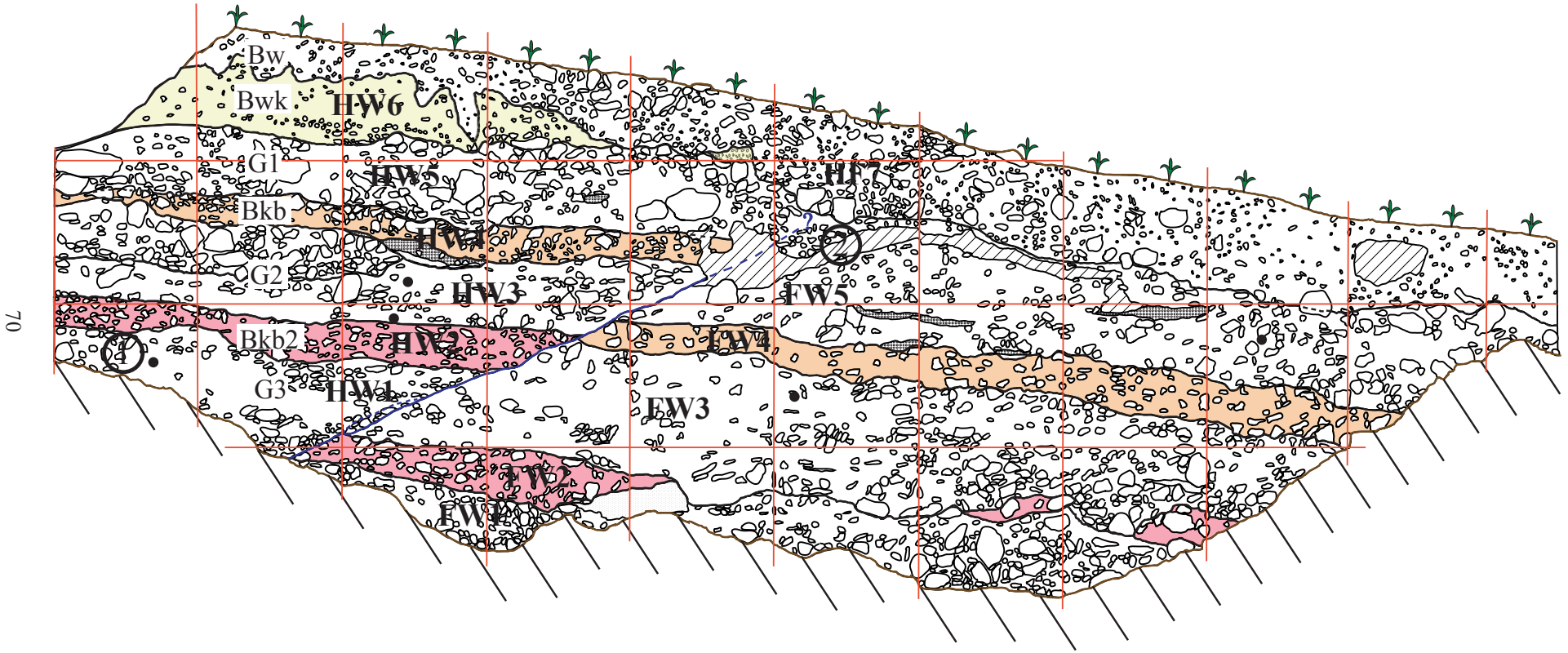
Bw
Bwk
HW6
G1
HW5
HF1
Bkb
HW4
G2
HW3
FW5
70
Bkb2
HW2
FW4
G3
HW1
FW3
FW2
FW1

Figure 28

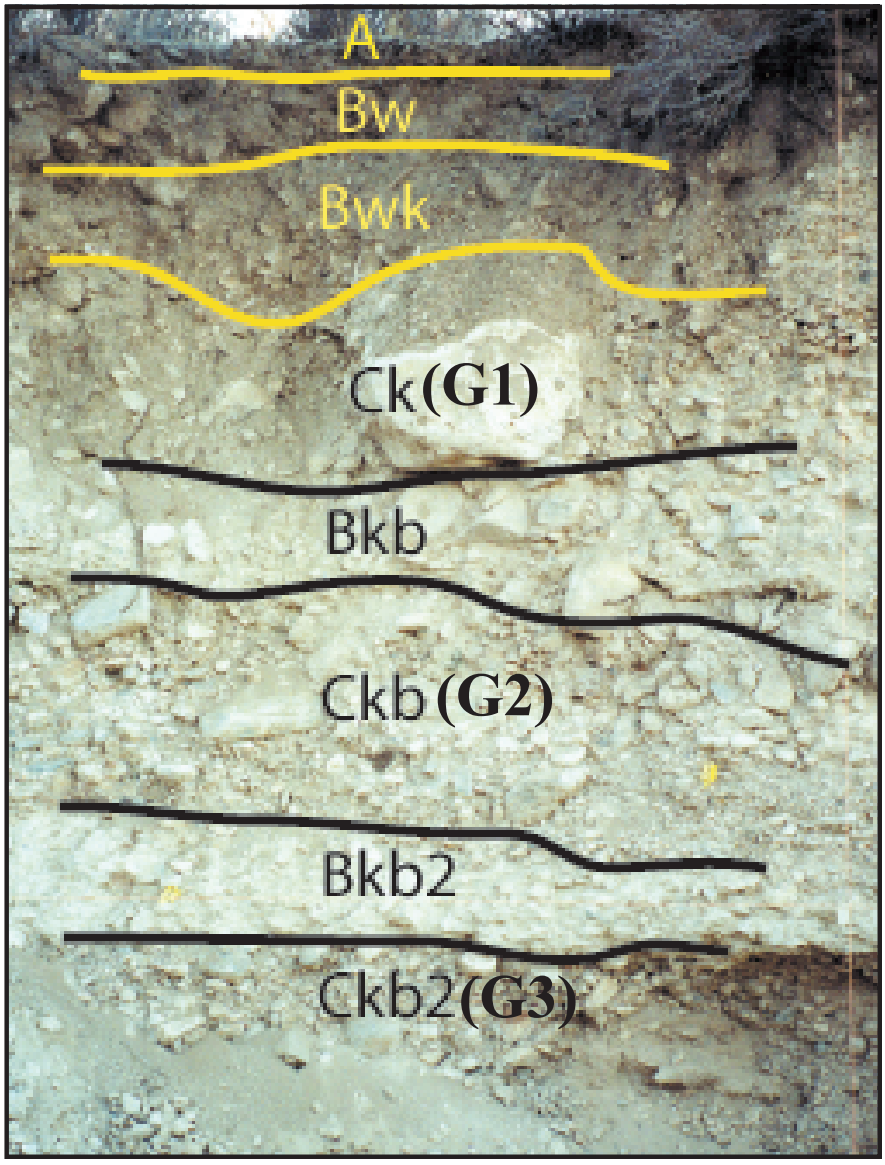

Figure 29

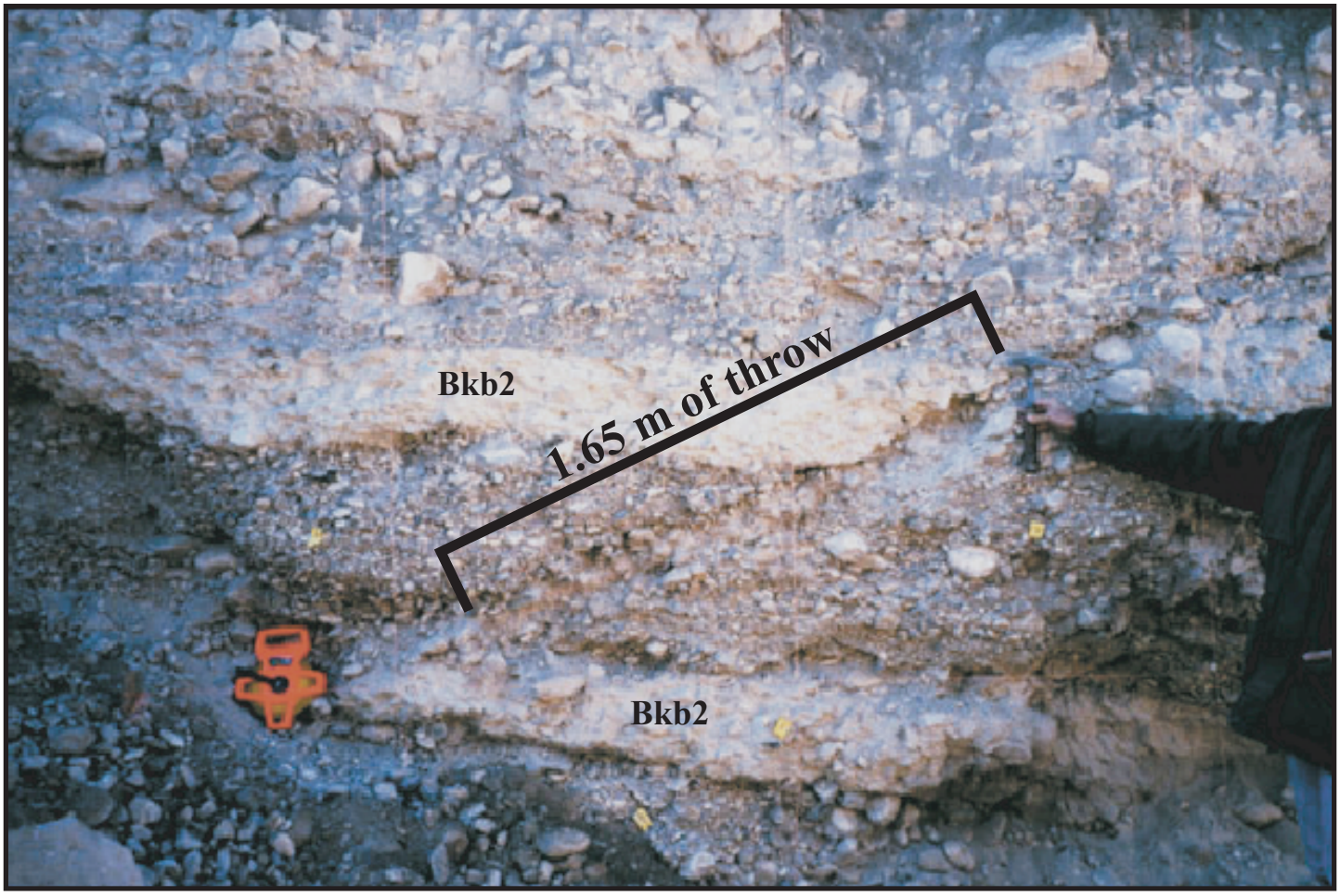

Figure 30

Figure 31

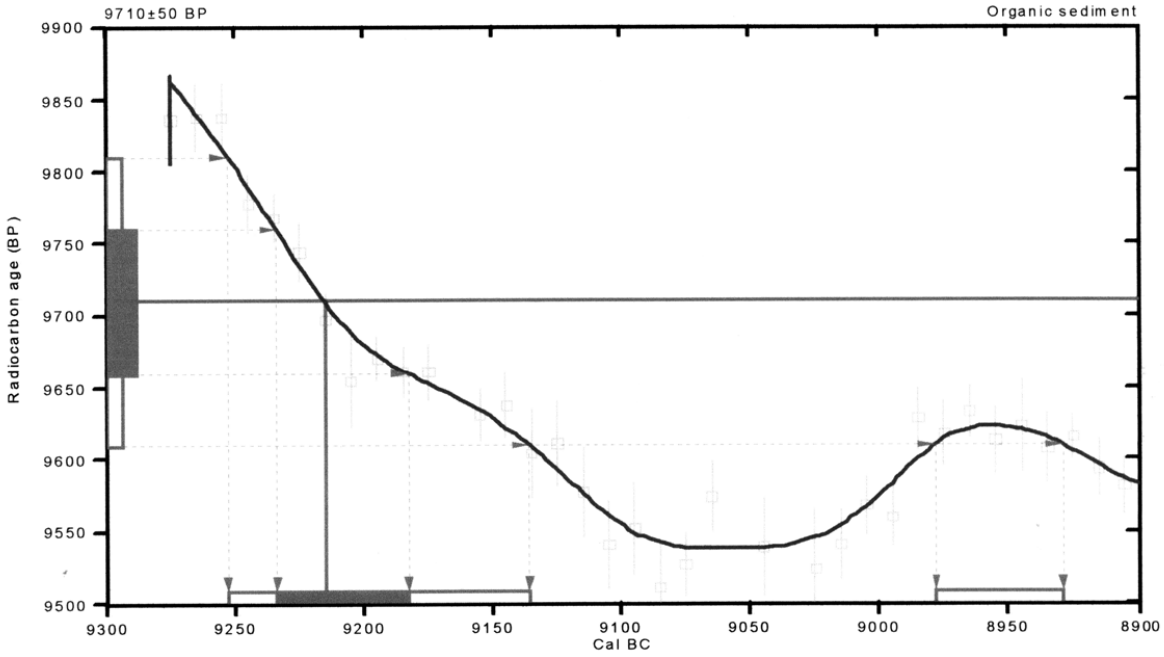
9710±50 BP
Organic sediment
Radiocarbon age (BP)
9900
9850
9800
9750
9700
9650
9600
9550
9500
9300
9250
9200
9150
9100
9050
9000
8950
8900
Cal BC

Chapter 4: Ground-Penetrating Radar and The Furnace Canyon Site

4.1 Introduction

In order to understand the seismogenic potential of the NFTS, we must completely constrain the most recent rupture history. The trench at the Marble Canyon site provided a maximum age of the most recent earthquake. However, we were not able to observe multiple events or determine a minimum age for the latest rupture. Therefore, we need a second site. Furnace Canyon is located ~9 kilometers to the west of the Marble Canyon site within the western segment of the NFTS (Figure 32). Therefore we should be able to expose the same event as observed at Marble Canyon. Due to the interpreted post-seismic age of the overlying alluvium, we hope to be able to establish a minimum age. We have yet to excavate, however in this study we implement geomorphic and geophysical means to precharacterize the site for future investigation.

The first step in precharacterizing the site was to perform a geomorphic analysis. The observation of 1:30000 airphotos revealed a large Pleistocene scarp (~6 m high) (Figure 32). A large drainage has incised an area through the southwest extremity of the scarp ~20 m wide. The incision has been infilled with young alluvium almost to the level of the Pleistocene scarp (~6 m). A Leica TC-805 electronic total station was used to collect elevation points in order to create a detailed topographic map of the area with 1-m contour intervals (Figure 33). The detailed mapping of the topography and field observations revealed there was no apparent scarp within the young alluvium. The thorough burial of the fault trace will possibly provide an intact overlying layer from which we can obtain a minimum age. The site was determined to correspond with Panel C of the geomorphic evolution scenarios (Figure 13). However, the intact overlying layer

also prevented determination of the exact location of the fault trace. The greater thickness of the infill deposits than at the Marble Canyon site also made it impossible to determine the excavation depth required. The risk associated with not being able to expose the fault initially prevented us from excavating at this site.

In order to reduce the risk associated with excavating at the Furnace Canyon site we need to utilize methods to image the subsurface prior to excavation. Delineating the structural and sedimentologic geometry and relationships of the shallow subsurface prior to excavation requires geophysical exploration. Ground-penetrating radar (GPR) is a geophysical technique used for high-resolution imagery of the subsurface, ranging from a few meters to 10's of meters in depth (Davis and Annan, 1989). The technique uses radio waves reflected from the subsurface to image changes in electrical properties of features such as bedding planes or fault planes (Davis and Annan, 1989; Corbeanu et al., 2001). It is analogous to seismic reflection methods, in that different frequencies result in varying resolution and depth penetration in different geologic settings (Reynolds, 1997). As a result, GPR is useful for a diverse array of geological problems (Annan and Davis, 1976; Stewart and Unterberger, 1976; Jezek et al., 1985; Fisher et al., 1989; Hammond and Sprenke, 1991; Davis and Annan, 1989), and can thus image fault-offset layers and occasionally fault planes themselves (Wyatt and Temples, 1996; Jun Cai et al., 1996). This, along with its low cost and easy application make GPR a valuable tool for nondestructive precharacterization of paleoseismic sites. We have used GPR to image the geometry of stratigraphy and faults and to constrain the precise locations of faults, where visible surface evidence of faulting is inconclusive in order to specifically precharacterize the Furnace canyon site for excavation.

GPR was used first at the Marble Canyon site (Figure 20) to establish a control. Previous studies on faults with vertical and dip-slip components of motion in desert environments are rare. Thus, we were unsure of the ability of GPR to image the stratigraphy, offsets, and fault planes in the Mojave Desert. After determining that GPR was useful at the Marble Canyon site, we then used it at Furnace Canyon to precharacterize the site.

4.2 Imaging the Shallow Subsurface using GPR

Because of the high velocity and frequency of radio waves, GPR is ideally suited for imaging stratigraphic features at shallow depths. Reflections are produced by boundaries between units with contrasting electrical properties such as grain size distribution (sorting, clay content), porosity, and water content (Knight and Nur, 1987; Davis and Annan, 1989; Annan et al., 1991). They can thus produce detailed images of recent stratigraphy, capable of resolving shallow faults and vertical offsets. Wyatt and Temples (1996) detected small scale channels and offset marker beds in unconsolidated sediments of the Atlantic Coastal Plain, demonstrating the value of GPR for delineating faults from offset stratigraphy. Cai et al. (1996) successfully used GPR as a reconnaissance tool for recognizing previously unknown strike-slip fault branches and determining trench locations in the San Francisco Bay region. Fault offsets and geometry and paleoearthquakes have also been constrained along other faults around the world using GPR (Yetton and Nobes, 1998; Camelbeeck and Meghraoui, 1998; Dehls et al., 2000; Meghraoui et al., 2000; and Chow, 2001). However, none of these have focused on shallowly dipping faults in arid alluvial environments. Whether GPR profiling can

resolve faults or offset reflectors in complex, channelized, coarse-grained stratigraphy is uncertain. The high conductivity salts common to desert soils can produce high electrical conductivity when damp, resulting in rapid attenuation of radio waves, preventing GPR use. On the other hand, seasonal dry conditions and low clay content of such an environment may be ideal for GPR. The GPR method provides precise targets for trench locations and improved likelihood of extracting paleoseismic data, if conditions are such that the subsurface structure can be resolved.

We used a pulseEKKO 100 GPR system manufactured by Sensors and Software Inc. to characterize the subsurface of candidate excavation sites. The GPR profiles were acquired perpendicular to the Pleistocene scarps within the younger alluvium. Multiple lines were acquired at both sites using 50, 100, and 200 MHz transmitter frequencies in order to determine the method with the best capability to image the fault (Appendix). All lines were acquired along the same path at the Marble Canyon site (Figure 20) and multiple paths were acquired at the Furnace Canyon site (Figure 33).

Profiles were acquired using transmitter frequencies centered on 50, 100, and 200 MHz, corresponding to wavelengths of ~2, ~1, and ~0.5 m. Excellent penetration was achieved, with maximum signal depth of ~18, ~14, and ~8 m respectively. Of these the 100 MHz surveys yielded the most coherent reflection patterns at both sites. Profiles were also collected using a common-offset geometry with 1-m antennae separation and 0.25-m station spacing for 100 MHz, scaled for other frequencies (Appendix). Pulser voltage was 400 volts and 64 to 256 pulses were stacked per trace. Each trace was collected with stationary transmitter and receiving antennae to avoid reflection smearing associated with movement over rough terrain and vegetation. Velocity was determined

from common midpoint profiles performed at each site, analogous to seismic reflection methods (Reynolds, 1997). Reflection travel times were converted to depth using this velocity. Additional data processing was performed using seismic software. Static topographic corrections were made using elevation data collected with a total station. An exponential gain was applied to increase reflection amplitude as a function of depth and counter the effects of wave attenuation (Fisher et al., 1992). Using a mild trace mix enhanced lateral continuity of reflections and a frequency filter was applied to reduce noise. We have also muted direct (non-reflection) radar waves from the air and ground (approximately the first 30 nanoseconds of each trace).

4.3 Results

The cross-fault GPR profiles contribute to the characterization of both sites. Coherent reflectors that are roughly parallel to the surface can be seen in both profiles (Figures 34 and 35), indicating that GPR is able to resolve complex channelized stratigraphy in an alluvial fan setting. Evidence for faulting is also apparent in the profiles.

The GPR profile at the Marble Canyon site was 60 m long and traversed roughly parallel to the drainage and perpendicular to the small ridge (Figure 20). The line crossed the small fault scarp in order to determine if the fault or offset stratigraphy could be imaged. Multiple CMP's were collected, centered at the 20-m and 45-m marks, using different frequencies to establish velocity variation with depth (Appendix). The CMP velocity analysis concluded a soil velocity of approximately 0.124 (0.118 to 0.127) m/ns at all depths. The 100 MHz GPR-profile (Figure 34) illuminated a strong south-dipping

reflector. The reflector dips ~23° south and can be traced to a subsurface depth of >9 m. We know the uppermost stratigraphy is offset 1.6 m, but we cannot tell if the GPR resolves this, or if deeper layers are offset more than the upper layers. However the south dipping reflector is analogous in orientation to exposures of the fault and matches its location in the trench and hence GPR is capable of predicting where to excavate.

The structures imaged with GPR at the Furnace Canyon site (Figure 33) were less obvious for interpretation. The GPR profile consisted of a 52-m long line within the active channel shown in Figures 32 and 33. The velocity analysis was centered at 15 m and concluded an average soil velocity of approximately 0.110 (0.104 m/ns to 0.117) m/ns. A strong north dipping reflector (A in Figure 6) is interpreted as a buttress unconformity, representing the contact between the erosional channel wall and the overlying channel deposits. Reflectors represented by B, C, and D in Figure 6 are interpreted as multiple fault strands. C and D clearly offset a strong stratigraphic reflector at ~6 m subsurface but cannot be traced with much confidence into the upper 3-m. Interpreted fault plane B (identified by offset beds) appears to offset shallow stratigraphy up to the muted region and is traceable to a maximum subsurface depth of ~7 m. The profile clearly indicates the northern ~8 m of the line to be the optimal location for excavation, slightly northwest of the Pleistocene scarps. The multiple strands could represent multiple events over a range in time that can be dated to constrain a recurrence interval for the fault. To sample these multiple strands will require an excavation 5-8 m deep.

4.4 Conclusions

The surveys of the Marble Canyon and Furnace Canyon sites demonstrate the ability of GPR as a collaborative and predictive tool for paleoseismic investigations. Multiple stream channels can be tested with this inexpensive and nondestructive method in order to determine candidate sites for investigation. Exposure of the fault plane at Marble Canyon allowed us to calibrate the acquisition method and determine imaging capabilities in the Mojave desert environment. Using GPR collaboratively with geomorphic observations at the Marble Canyon site, we were able to determine the utility of the high-resolution imaging technique as a predictive tool performed prior to an excavation. At the Furnace Canyon site, the initial geomorphic analysis was unable to determine the exact location of the fault trace in the young surface alluvium, presumably due to deposition after the most recent earthquake. This limited our ability to determine the optimal site for investigation. GPR reduced the ambiguity associated with geomorphic limitations by providing a high-resolution image of the subsurface. The scale of resolution and maximum depth of penetration are very similar at both sites and continue deeper than trenching capabilities. In this study, GPR was not only proven invaluable in its ability to locate an ambiguous fault, but also in its ability to locate multiple strands that otherwise may have been unrecognized. As a result, we now know where to excavate and in future work we can possibly determine a recurrence interval and constrain a minimum age for the most recent event of the NFTS.

Chapter 4: Figure Captions

Figure 32–(A). Tectonic map of southern California, showing the location of our case study along the northern San Bernardino mountains. ECsz = Eastern California shear zone, GF = Garlock Fault, HF = Helendale fault, SAF = San Andreas fault, SBM =San Bernardino Mountains, SJF = San Jacinto fault, SM-CF Sierra Madre-Cucamonga fault, wTR = western Transverse Ranges. (B) Aerial photograph of the central part of the North Frontal thrust system. Exact locations of the Marble Canyon and Furnace Canyon sites are shown.

Figure 33–Detailed topographic map of the Furnace Canyon site. A prominent Pleistocene scarp occurs southwest and northeast of the active drainage. Young material within the drainage is over 6 m deep with no surface evidence of rupture. Contours are drawn at 1 m intervals and location of GPR profiles are denoted with large dots.

Figure 34–100-MHz GPR cross-fault profile of the Marble Canyon site (location shown in Figure 20). Arrows indicate the location of the fault plane reflector and the relative motion associated with the fault. Note the top of the profile has been topographically corrected, indicating the projection of the fault corresponds to the surficial scarp and to the fault in the parallel trench (Figure 26).

Figure 35–100-MHz GPR profile of the Furnace Canyon site (Figure 32). Strong reflection A corresponds to a buttress unconformity between the channel walls and the channel-fill. Interpreted lines B, C, and D indicate the location of suggested fault plane reflectors. C and D clearly offset horizontal layers at depth, but do not appear to rupture the upper 4 m of the profile. Line B

appears to be comprised of two strands, traceable to the muted layer. The surface projection of B is likely the region to focus future paleoseismic investigation.

Figure 32

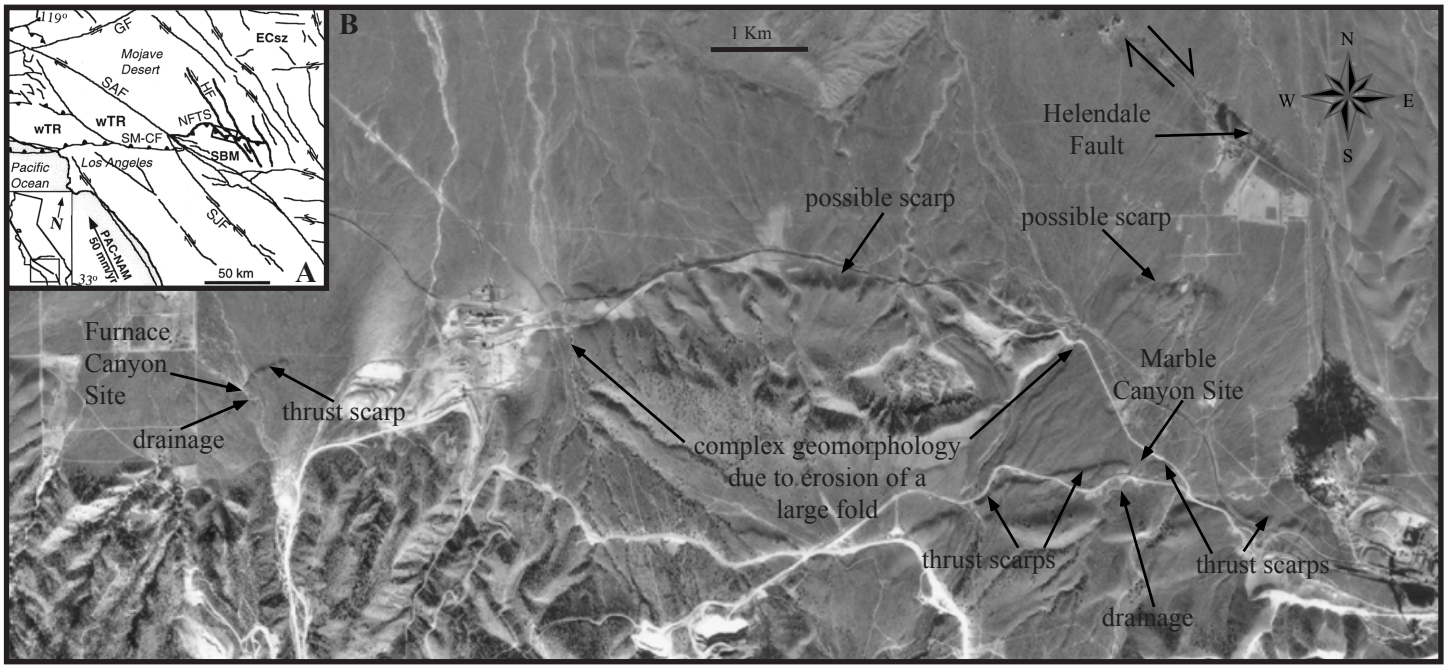
B
1 Km
N
W
E
S
Helendale
Fault
possible scarp
possible scarp
Furnace
Canyon
Site
drainage
thrust scarp
complex geomorphology
due to erosion of a
large fold
Marble
Canyon Site
thrust scarps
thrust scarps
drainage
119°
GF
ECsz
Mojave
Desert
SAF
HF
wTR
wTR
NFTS
SM-CF
SBM
Pacific
Ocean
Los Angeles
SJF
N
PAC-NAM
50 mm/yr
33°
50 km
A

Figure 33

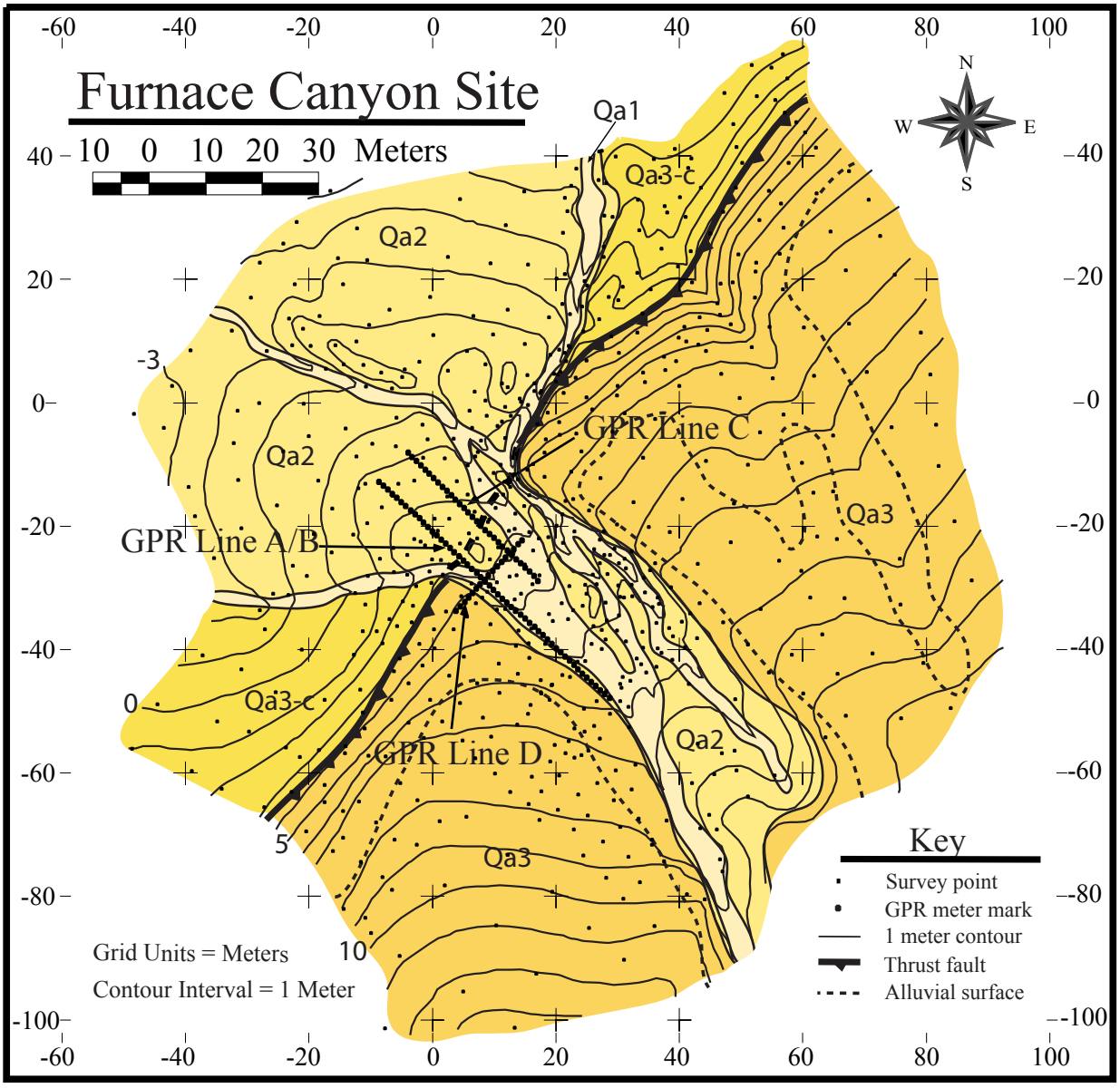
Furnace Canyon Site
10 0 10 20 30 Meters
N
W
E
S
Qa1
Qa3-c
Qa2
GPR Line C
Qa3
GPR Line A/B
Qa2
Qa3-c
GPR Line D
Qa2
Qa3
Grid Units = Meters
Contour Interval = 1 Meter
Key
Survey point
GPR meter mark
1 meter contour
Thrust fault
Alluvial surface

Figure 34

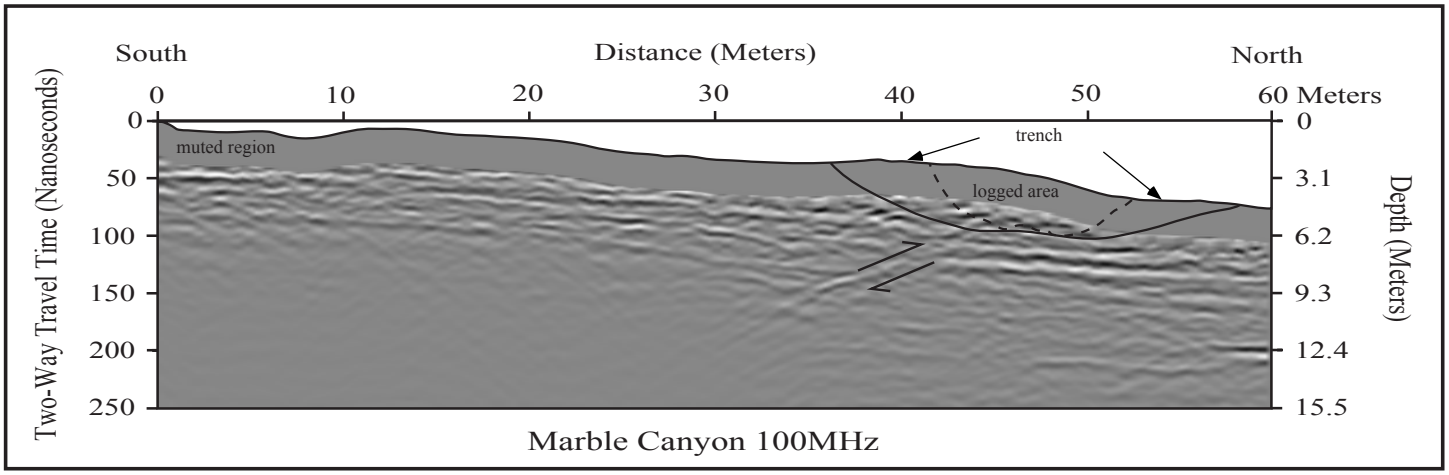
South
Distance (Meters)
North
0
10
20
30
40
50
60 Meters
0
50
100
150
200
250
Two-Way Travel Time (Nanoseconds)
muted region
trench
logged area
0
3.1
6.2
9.3
12.4
15.5
Depth (Meters)
Marble Canyon 100MHz

Figure 35

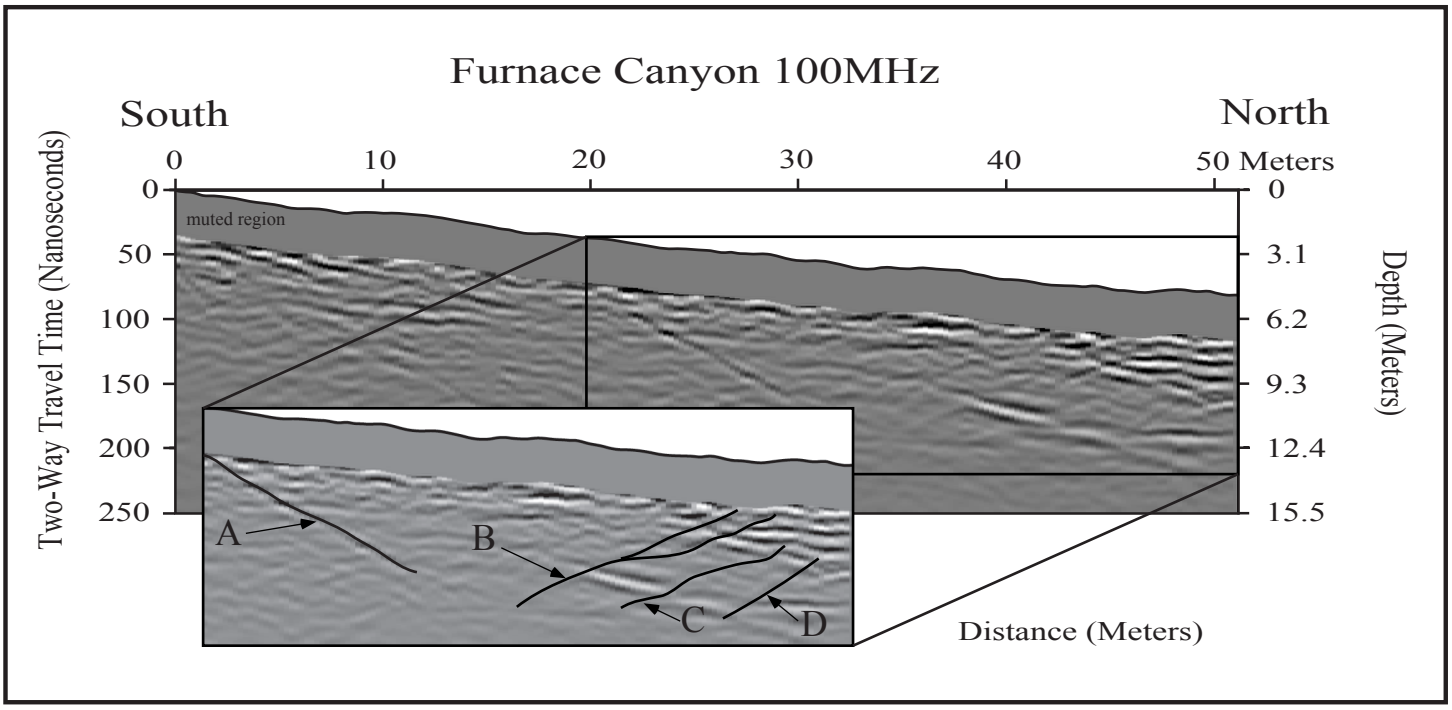
Furnace Canyon 100MHz
South
North
0
10
20
30
40
50 Meters
0
50
100
150
200
250
Two-Way Travel Time (Nanoseconds)
muted region
0
3.1
6.2
9.3
12.4
15.5
Depth (Meters)
A
B
C
D
Distance (Meters)

Chapter 5: Conclusions

5.1 Paleoseismology of the North Frontal Thrust System

It has been suggested the North Frontal Thrust System has decreased in activity by an order of magnitude or has even become extinct in the late Pleistocene or Holocene. Investigations have attempted to constrain the most recent rupture history of the thrust, however none have indicated Holocene activity. This study constrains the most recent rupture history by utilizing basic geomorphic site characterizations and a paleoseismic excavation.

By developing a basic understanding of geomorphic processes, we were able to relate idealized scenarios to actual field settings. The geomorphic environment necessary for a successful paleoseismic excavation is unique. Continuous deposition and minimal erosion must accompany tectonic events in a manner allowing the constraint of the timing of ruptures. Observation of airphotos and detailed geomorphic mapping determined locations analogous to the idealized scenarios. We located two candidate sites, Marble Canyon and Furnace Canyon. Thick deposits of young channel alluvium bury the fault trace at the Furnace Canyon site with no evidence of surface rupture. Minimum and Maximum age constraints would certainly be possible at this site, however we are unable to determine exactly where to excavate. Alternatively, the Marble Canyon site was small scale and had a small ridge (possibly a scarp) ~1 m high. Field observations and detailed geomorphic mapping suggested the small ridge was a scarp, and indicated the exact location to excavate.

Excavation exposed the fault with a nice clean break and no evidence of secondary mineral deformation, slickensides, or preferred cobble alignments. These

characteristics of the fault implied the rupture was associated with only one event. It was a low angle thrust dipping 23° to the south and trending N85°W. Two paleosols were correlated across the rupture indicating ~1.65 m of throw and a bulk sample from a gravel layer in the hanging wall was sent for radiocarbon dating. Dating indicated a depositional age for the basal gravel layer of 9220 BC (11220 yr BP). The observed rupture offset an additional 1 ½ m of deposits above the dated horizon, indicating the timing of the event to be well within the Holocene. Therefore, the NFTS is active.

This finding has a major impact on our awareness of the local hazard associated with the NFTS. Damage associated with the M5.4 Big Bear event illustrates the importance of constraining the activity of the NFTS. If the 30-40 km length of the western segment were to rupture with 1.65 m of throw, the event would be capable of a M7 or greater. We constrained a maximum age, but no minimum age, and we did not observe multiple events, therefore we could not determine a recurrence interval. We were thus unable to determine at what stage of the seismic cycle the NFTS was in.

The active NFTS also has an effect on the San Andreas Fault, for as convergent stress builds in association with the NFTS, a normal stress is increased on the San Andreas. The increase in normal stress will extend the recurrence interval of the San Andreas. However, a rupture of the NFTS can immediately reduce the normal stress and the recurrence interval of the San Bernardino segment of the San Andreas.

5.2 Implications Associated with the Behavior of Intersecting Faults

Four scenarios were postulated for how the ECSZ and the NFTS may interact. We are only able to exclude one scenario at this time. Our investigations, plus recent

investigations and seismicity of the ECSZ has determined that neither system is extinct. Paleoseismic constraints are still needed in the central and eastern segments of the NFTS. We can no longer assume the ECSZ is the dominant tectonic source and responsible for the termination of activity associated with the NFTS. However, at this time, we cannot prove if the ECSZ behaves as a segment boundary or is responsible for termination of thrust activity within the central and eastern segments. We also cannot determine if the NFTS is capable of rupturing its entire length. Constraints on the rupture histories of the eastern and central segments of the NFTS and a comparison to the history of the ECSZ are required to fully understand the capabilities and relationship of the NFTS and ECSZ.

5.3 Geophysical Techniques as a Predictive Tool

Ground-penetrating radar is an effective technique to image the shallow subsurface at high resolutions. The images at the Marble Canyon site illustrated a sharp distinct fault plane reflector correlative to the fault exposed in the trench. Having calibrated the acquisition technique, GPR was then used at the Furnace Canyon site in order to determine where the fault was located within the ~6-m thick channel sediments. We interpreted three fault planes with vertically offset layers. The multiple fault planes may indicate multiple events and therefore it may be possible to constrain a recurrence interval. The images produced with GPR indicate exactly where to excavate, reducing the risk associated with a paleoseismic investigation. Therefore, GPR has proven to be an invaluable, inexpensive and nondestructive tool that can be utilized for precharacterization of candidate paleoseismic sites.

Appendix

Figure 36-50 MHz profile at the Marble Canyon site processed using seismic software (Figure 20). Static topographic corrections were made using elevation data collected with a total station. An exponential gain was applied to increase reflection amplitude, a mild trace mix enhanced lateral continuity of reflections and a frequency filter was applied to reduce noise. We have also muted direct (non-reflection) radar waves from the air and ground (approximately the first 30 nanoseconds of each trace).

Figure 37-200 MHz profile at the Marble Canyon site processed using seismic software (Figure 20). Static topographic corrections were made using elevation data collected with a total station. An exponential gain was applied to increase reflection amplitude, a mild trace mix enhanced lateral continuity of reflections and a frequency filter was applied to reduce noise. We have also muted direct (non-reflection) radar waves from the air and ground (approximately the first 30 nanoseconds of each trace).

Figure 38-Data acquired in Common-midpoint format with 50 MHz antennae for velocity analysis at the Marble Canyon site. This line was centered at the 20-m mark of the GPR line in Figure 20. The analysis of Layer F was used in conjunction with layers acquired with other frequencies to conclude an average soil velocity of approximately 0.124 (0.118 to 0.127) m/ns at all depths.

Figure 39-Data acquired in Common-midpoint format with 100 MHz antennae for velocity analysis at the Marble Canyon site. This line was centered at the 20-m mark of the GPR line in Figure 20. The analysis of Layers B, C, and D was

used in conjunction with layers acquired with other frequencies to conclude an average soil velocity of approximately 0.124 (0.118 to 0.127) m/ns at all depths.

Figure 40-Data acquired in Common-midpoint format with 200 MHz antennae for velocity analysis at the Marble Canyon site. This line was centered at the 20-m mark of the GPR line in Figure 20. The analysis of Layer E was used in conjunction with layers acquired with other frequencies to conclude an average soil velocity of approximately 0.124 (0.118 to 0.127) m/ns at all depths.

Figure 41-50 MHz profile at the Furnace Canyon site processed using seismic software, located along line A/B in Figure 33. Static topographic corrections were made using elevation data collected with a total station. An exponential gain was applied to increase reflection amplitude, a mild trace mix enhanced lateral continuity of reflections and a frequency filter was applied to reduce noise. We have also muted direct (non-reflection) radar waves from the air and ground (approximately the first 30 nanoseconds of each trace).

Figure 42-50 MHz profile at the Furnace Canyon site, unprocessed, located along line C in Figure 33.

Figure 43-100 MHz profile at the Furnace Canyon site, unprocessed, located along line C in Figure 33.

Figure 44-100 MHz profile at the Furnace Canyon site, unprocessed, located along line D in Figure 33.

Figure 45-Data acquired in Common-midpoint format with 100 MHz antennae for velocity analysis at the Furnace Canyon site. The velocity analysis was

centered at 15 m. The analysis of Layers A and B was used in conjunction with layers acquired with other frequencies to conclude an average soil velocity of approximately 0.110 (0.104 m/ns to 0.117) m/ns.

Figure 46-Data acquired in Common-midpoint format with 200 MHz antennae for velocity analysis at the Furnace Canyon site. The velocity analysis was centered at 15 m. The analysis of Layers C and D was used in conjunction with layers acquired with other frequencies to conclude an average soil velocity of approximately 0.110 (0.104 m/ns to 0.117) m/ns.

Figure 36

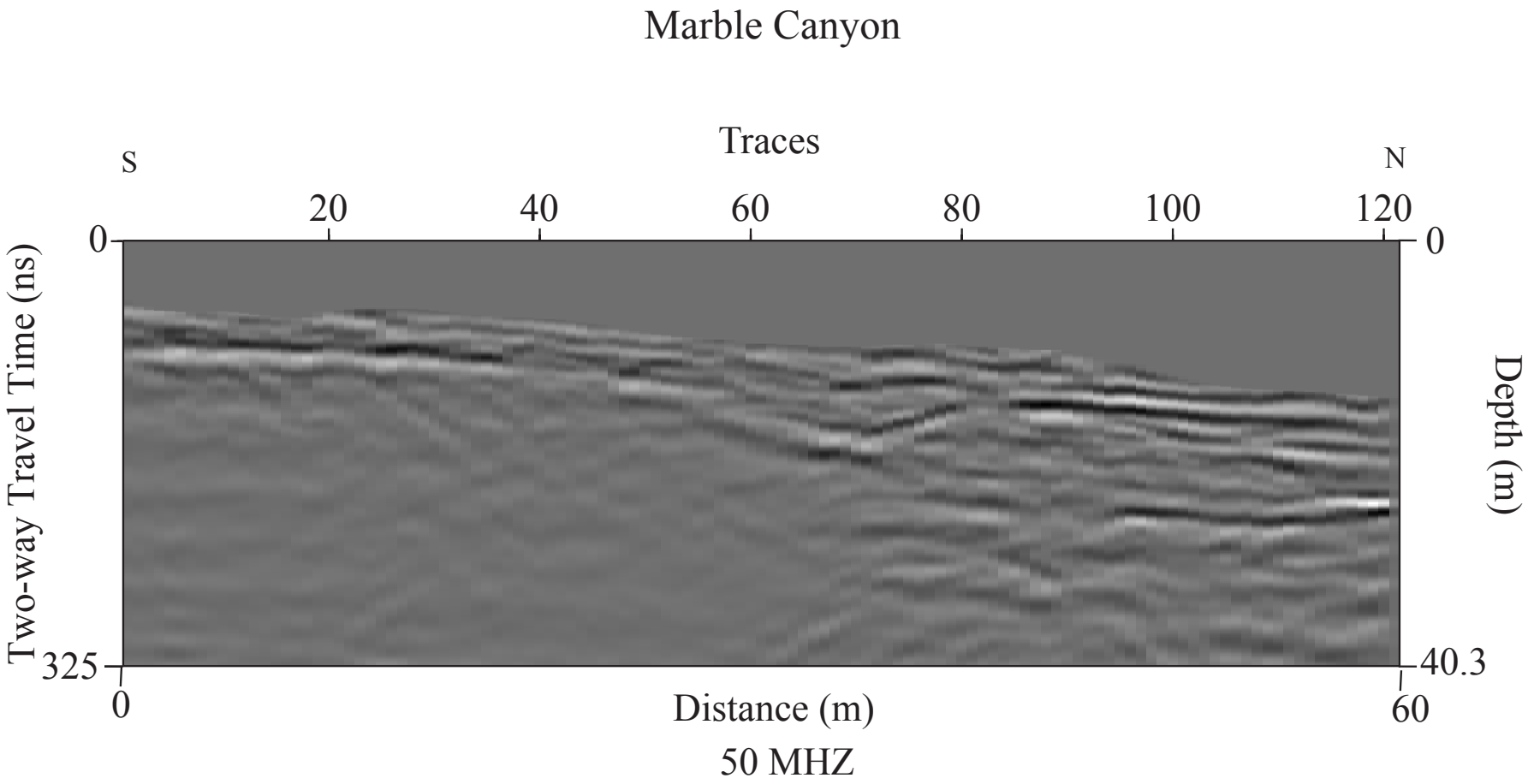
Marble Canyon
Traces
S
N
20
40
60
80
100
120
0
0
Two-way Travel Time (ns)
Depth (m)
325
40.3
0
Distance (m)
60
50 MHZ

Figure 37

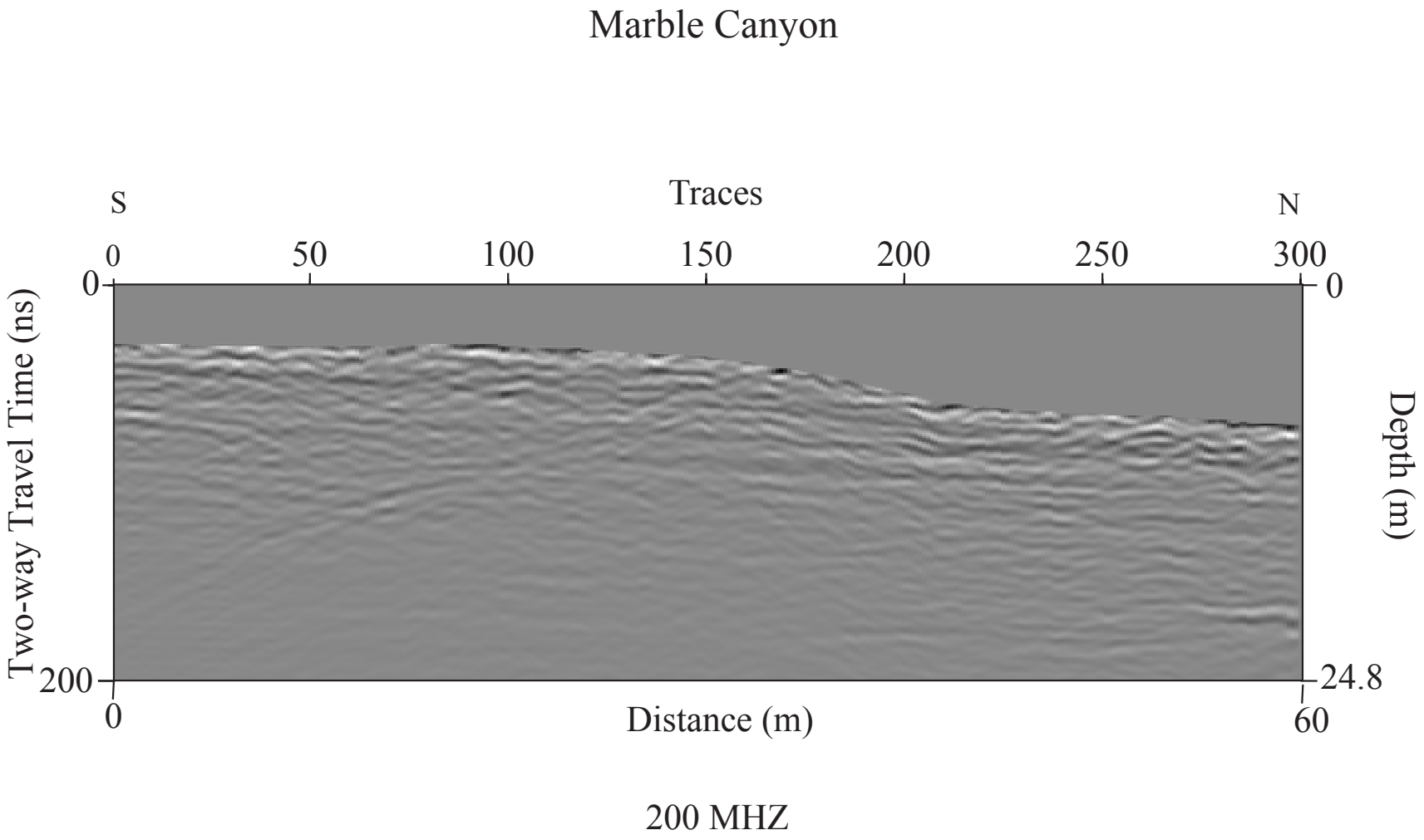
Marble Canyon
Traces
S
N
0
50
100
150
200
250
300
0
200
Two-way Travel Time (ns)
Depth (m)
0
24.8
Distance (m)
60
200 MHZ

Figure 38

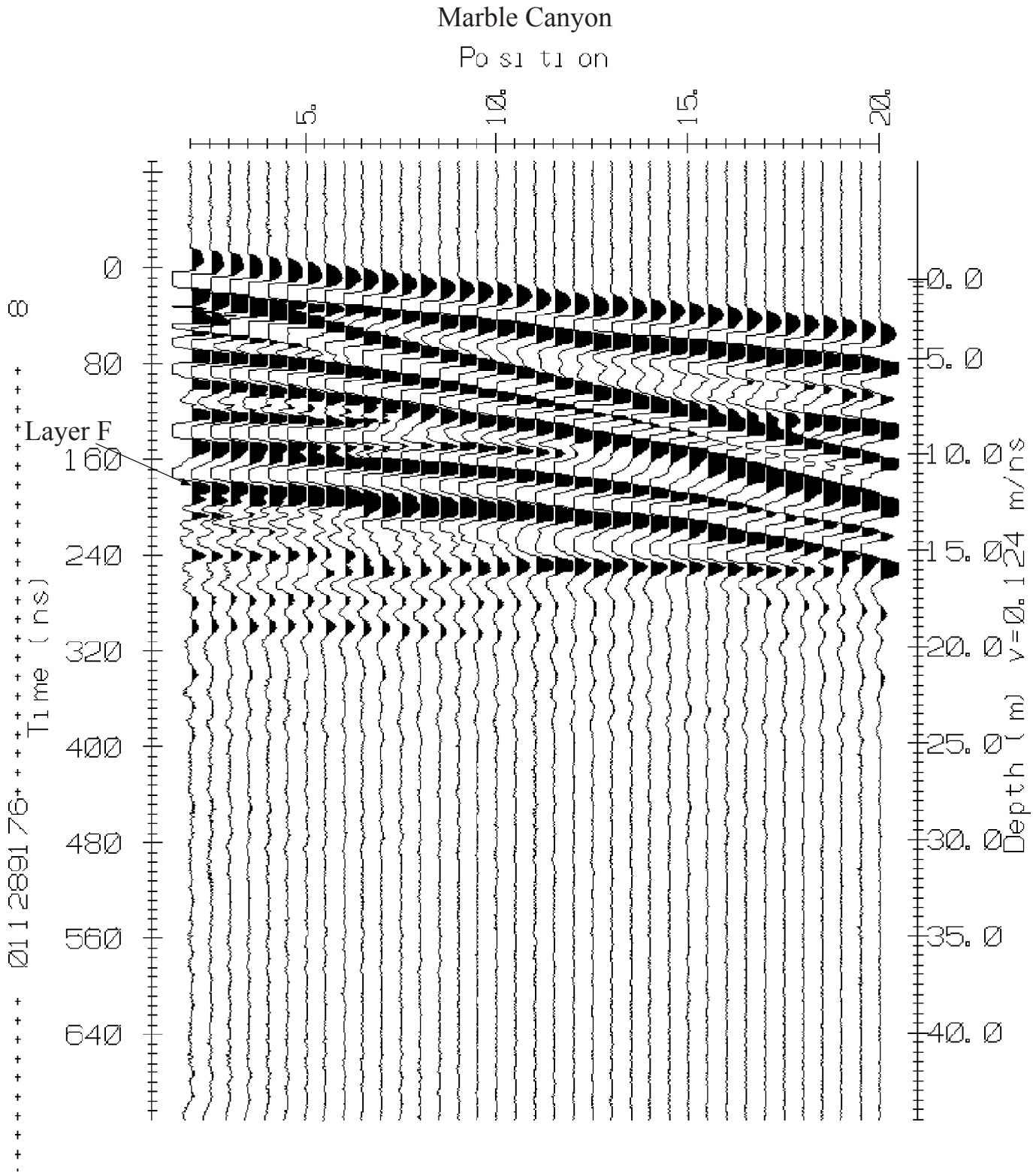

50 MHz CMP

Figure 39

Marble Canyon

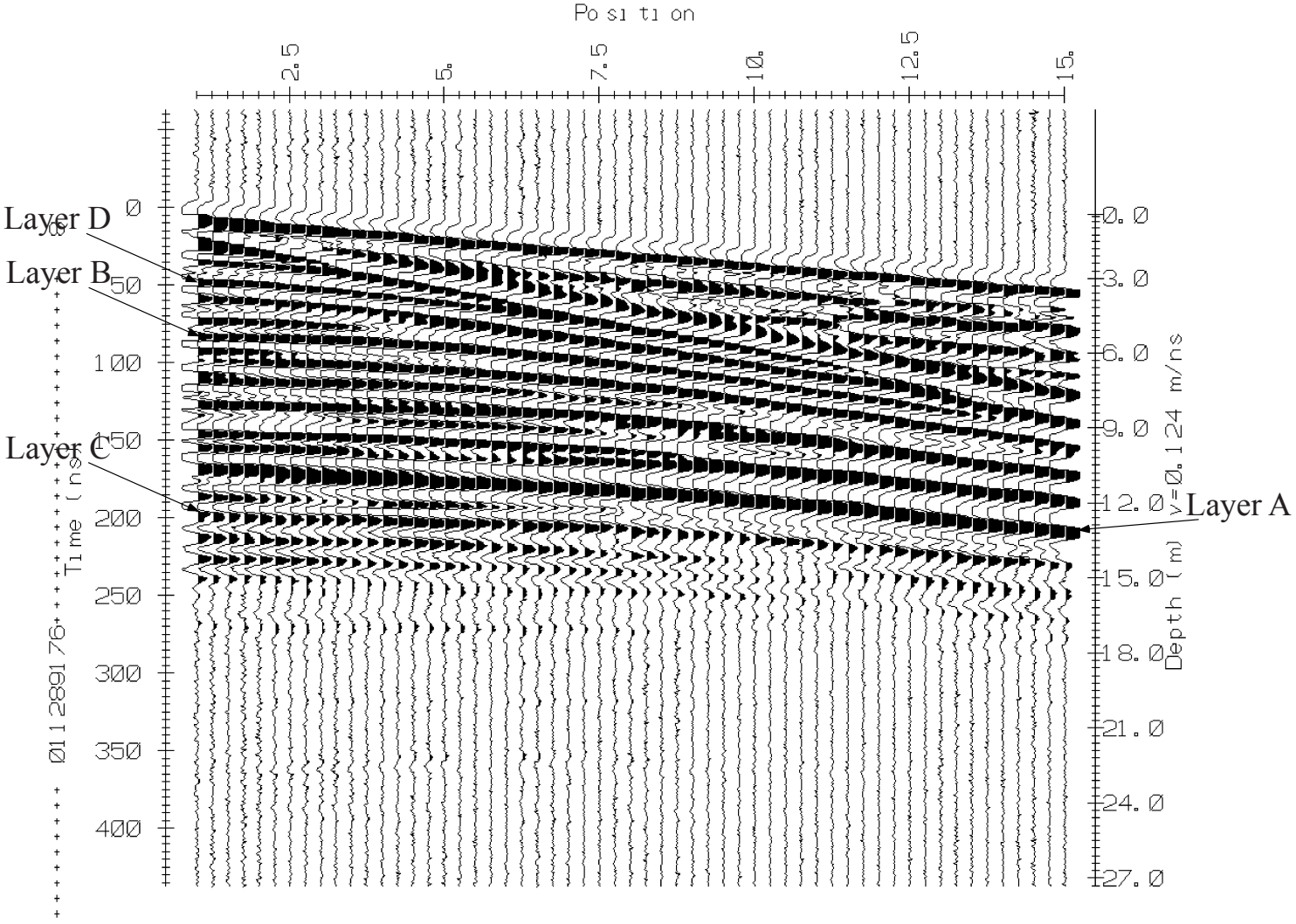

100 MHz CMP

Figure 40

Marble Canyon

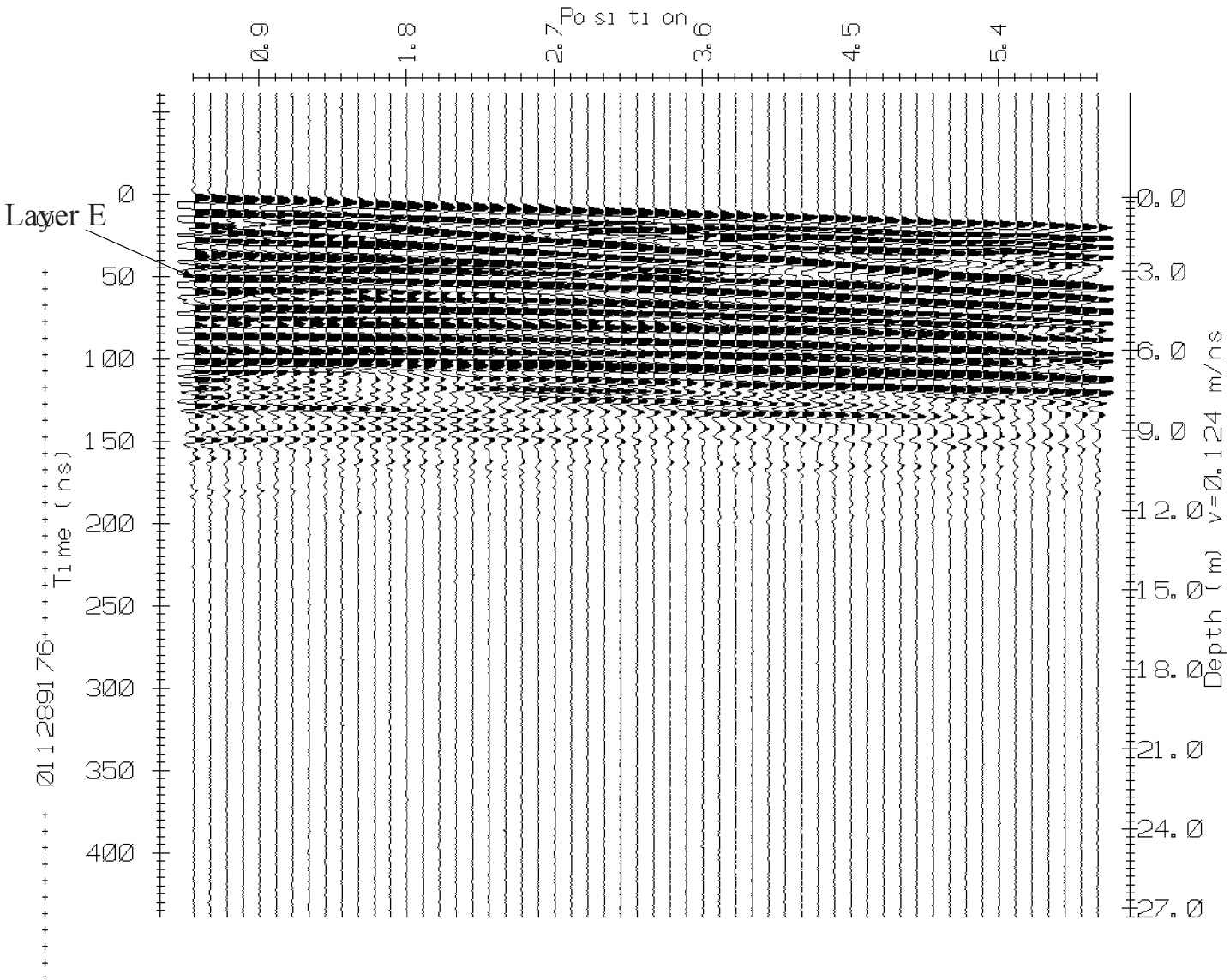

200 MHz CMP

Figure 41

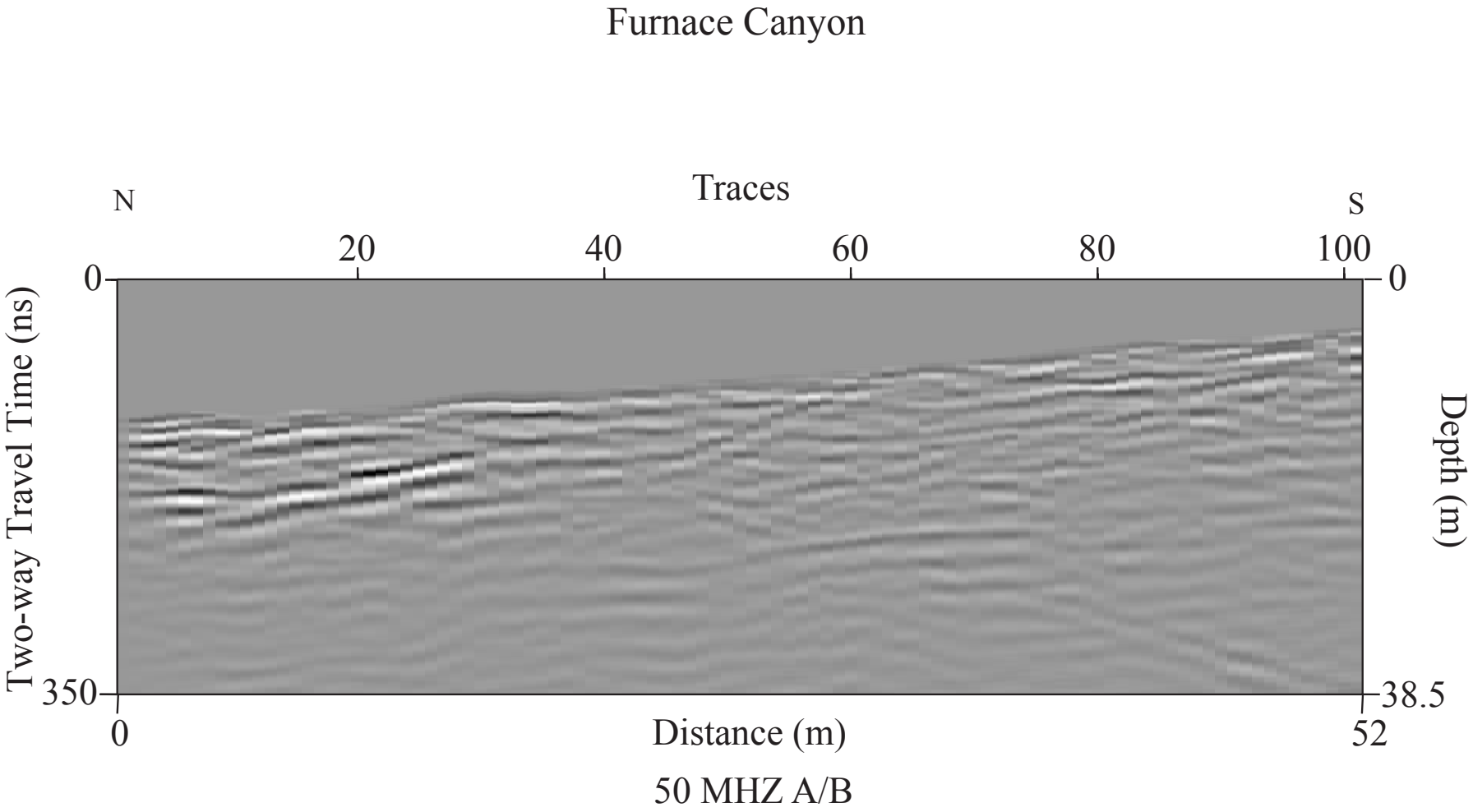
Furnace Canyon
Traces
N
S
20
40
60
80
100
0
0
Two-way Travel Time (ns)
Depth (m)
350
38.5
0
Distance (m)
52
50 MHZ A/B

Figure 42

Furnace Canyon

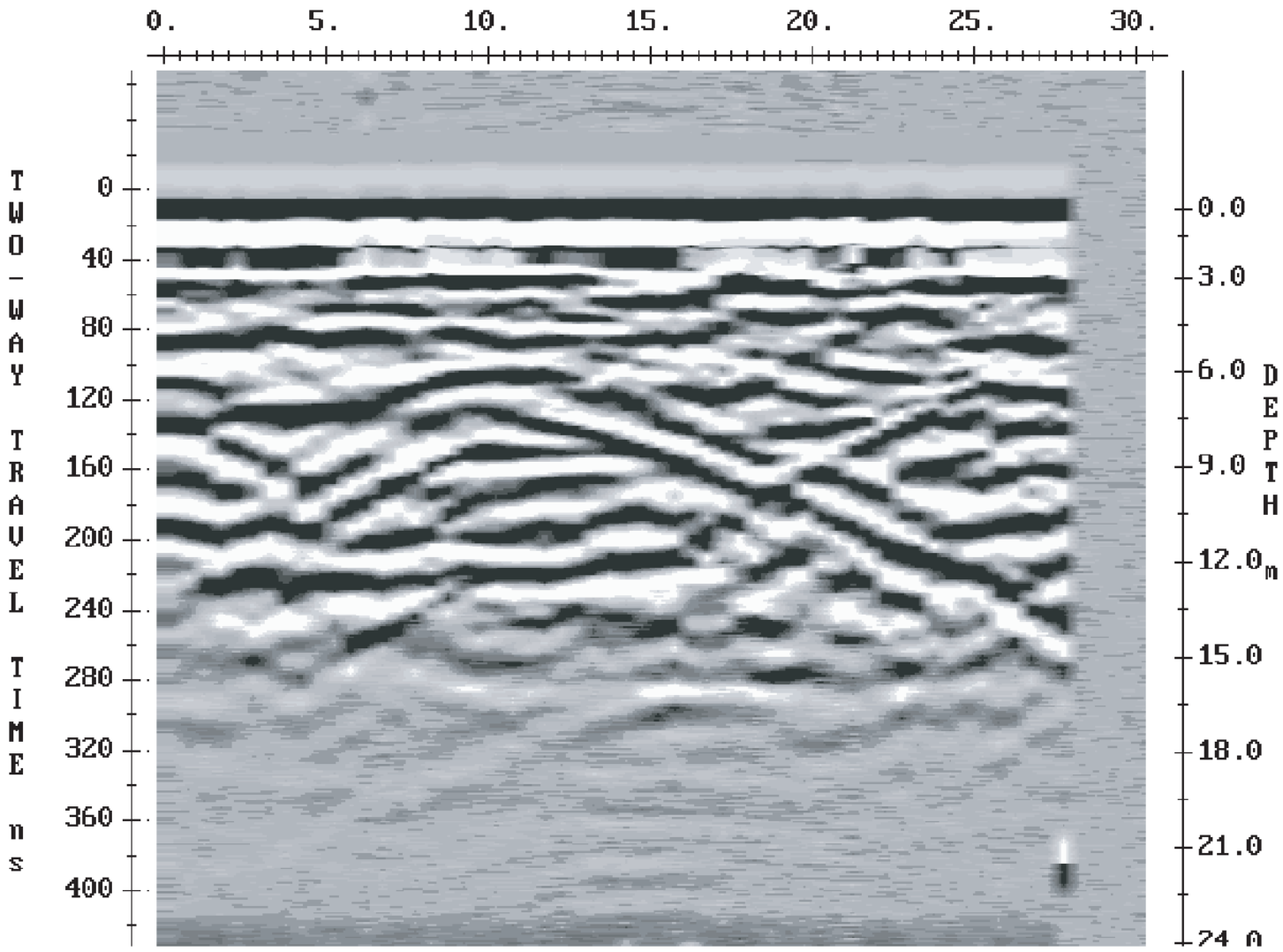

50 MHz - C - Color

Figure 43

Furnace Canyon

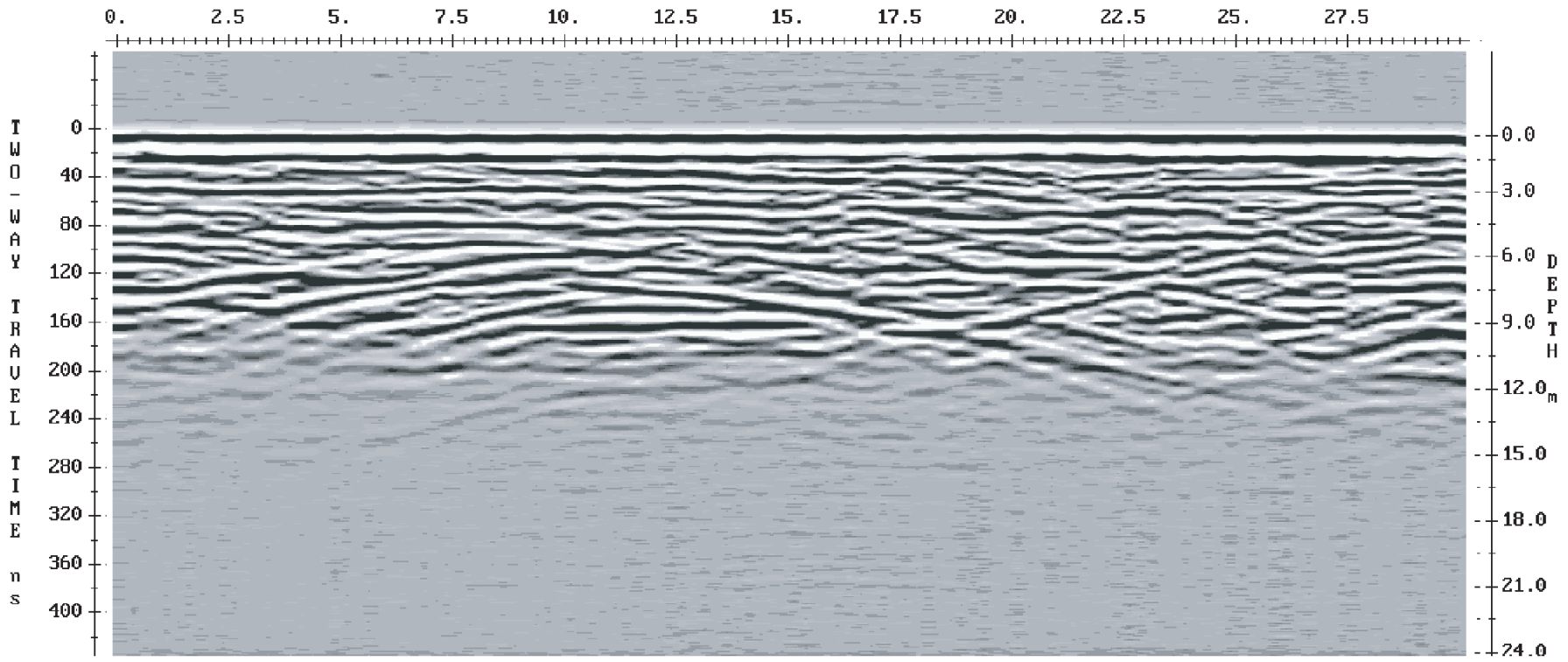

100 MHz - C - Color

Figure 44

Furnace Canyon

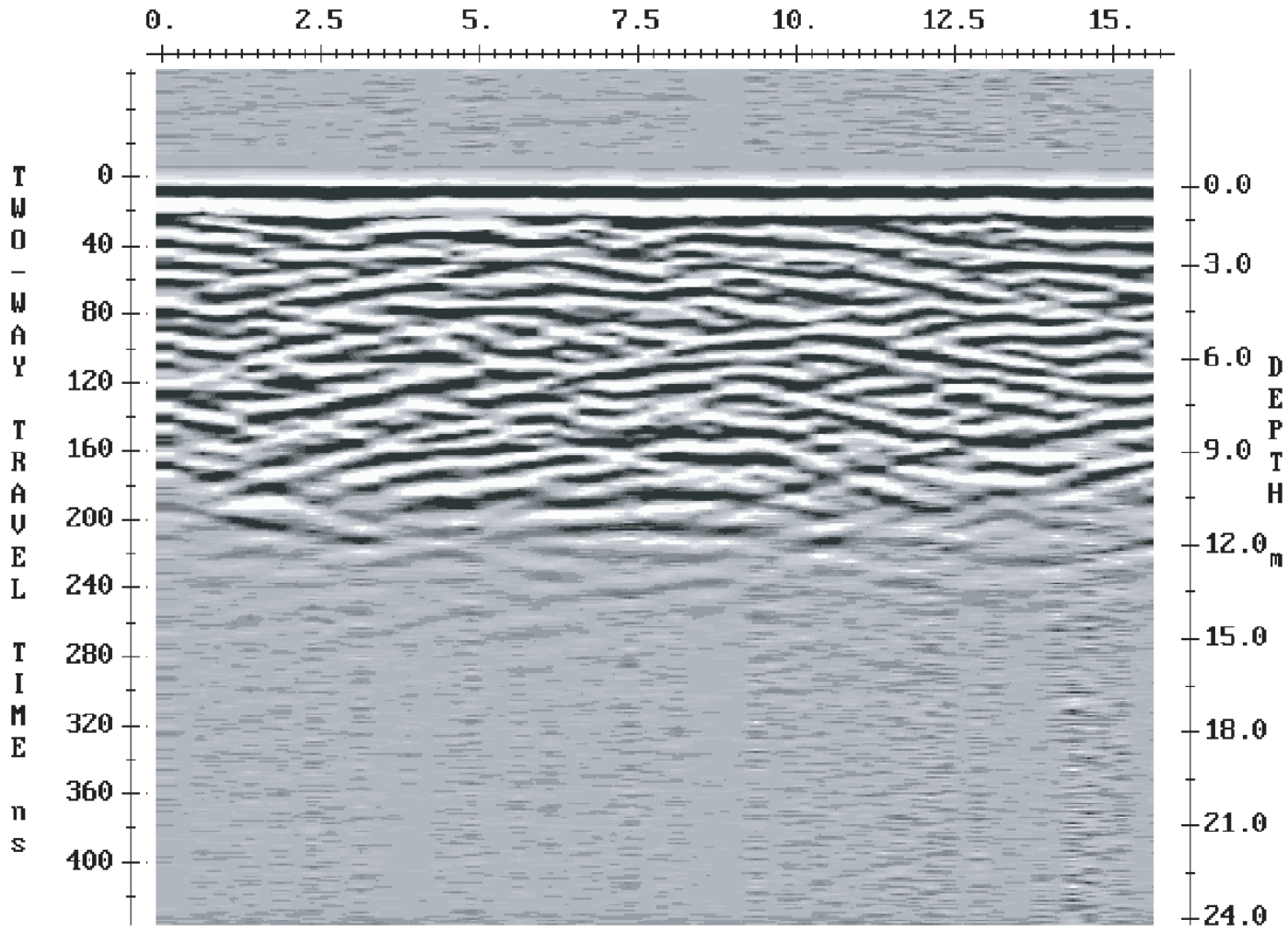

100 MHz - D - Color

Figure 45

Furnace Canyon

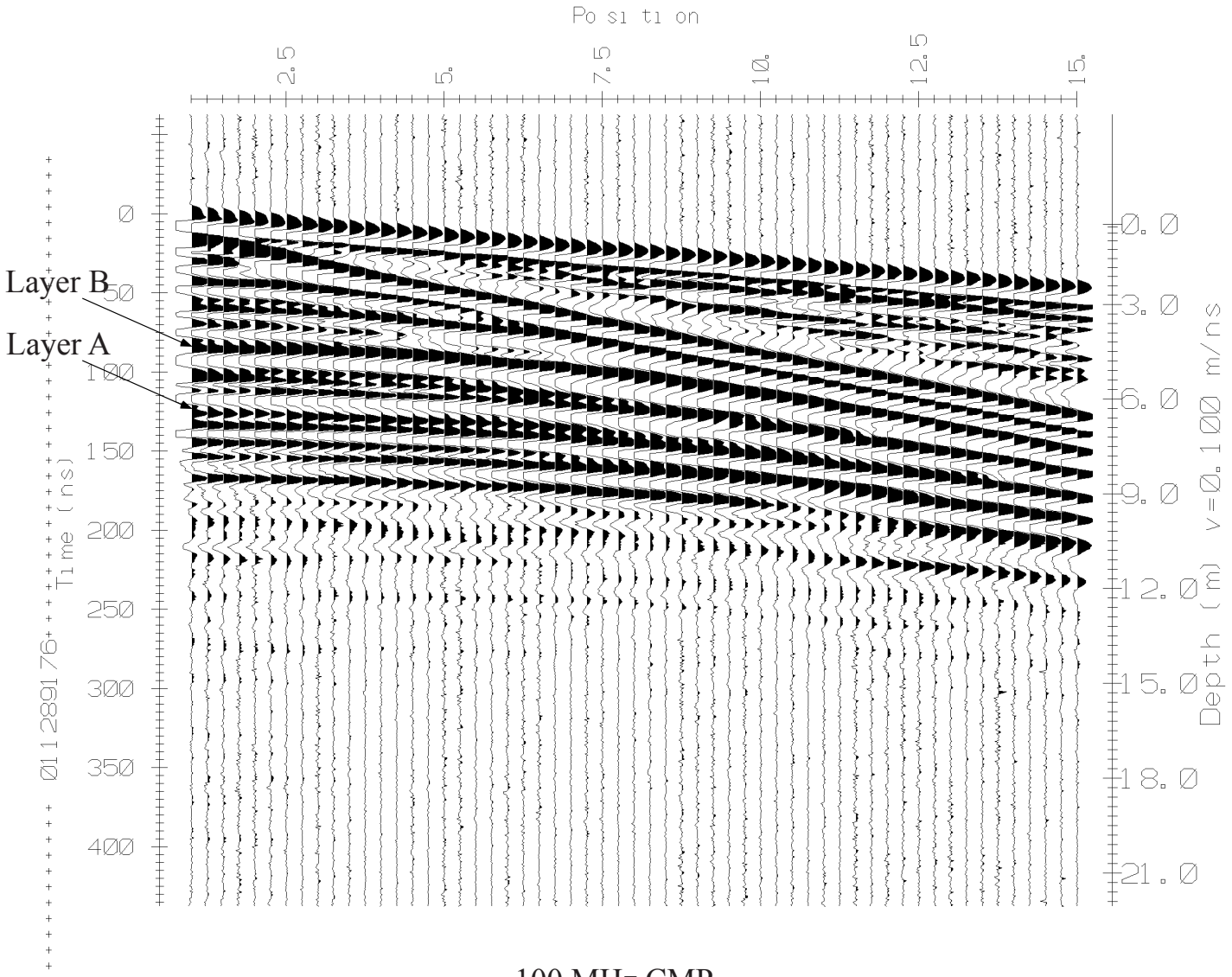

100 MHz CMP

Figure 46

Furnace Canyon

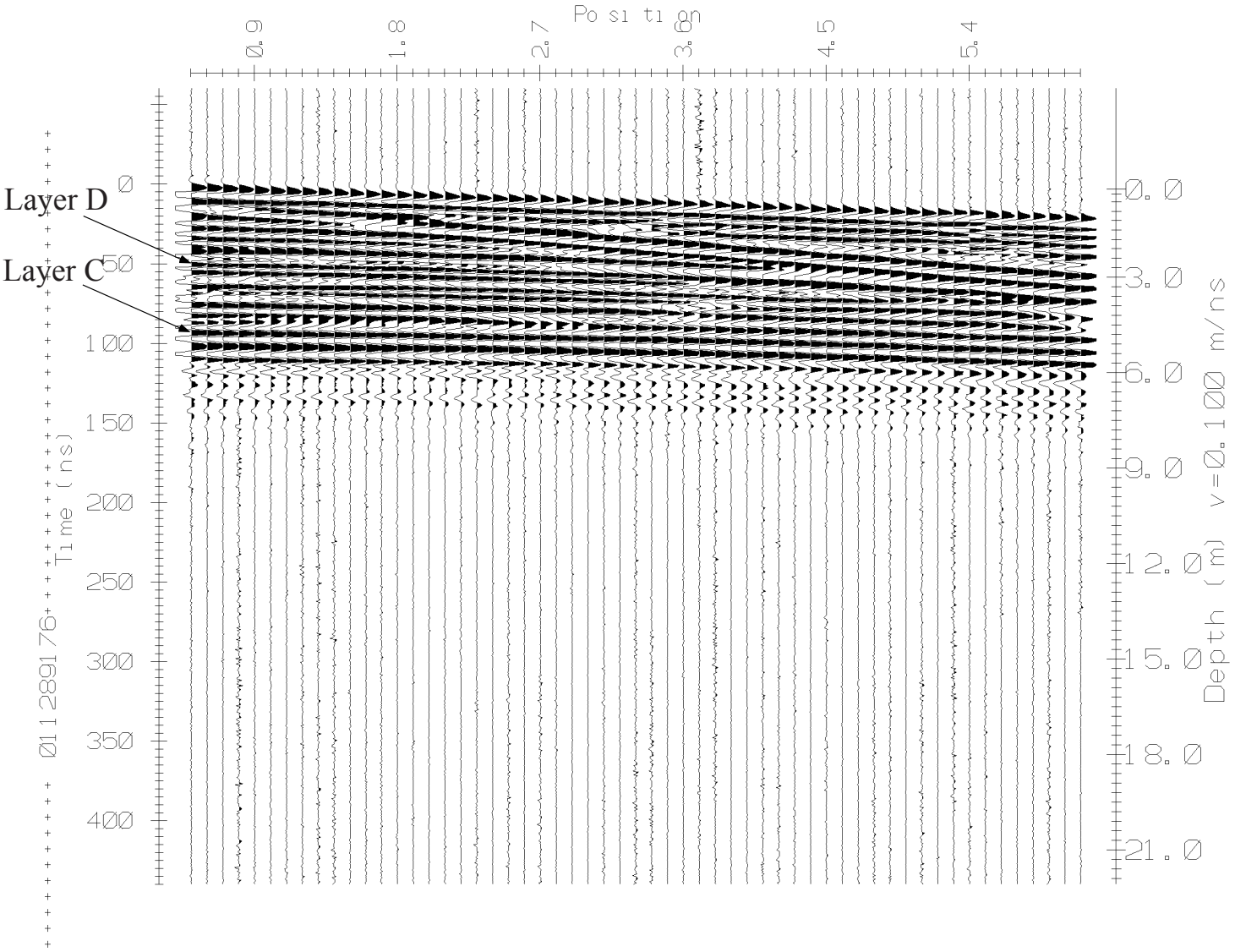

200 MHz CMP

References

Anderson, E. M., Dynamics of faulting and dyke formation, *Edinburgh, Oliver, and Boyd,* 191 p., 1951

Annan, A. P., and J. L. Davis, Impulse radar sounding in permafrost, *Radio Sci.,* 11, 383-394, 1976.

Annan, A. P., S. W. Cosway, and J. D. Redman, Water table detection with ground-penetrating radar, *(abs.): Society of Exploration Geophysicists Annual International Meeting and Exposition Program with Abstracts,* 494-497, 1991.

Atwater, Brian F., Evidence for great Holocene earthquakes along the outer coast of Washington State, *Science,* vol. 236, no. 4804*,* 942-944, 1987.

Barka, A. A., and K. Kadinsky-Cade, Strike-slip fault geometry in Turkey and its influence on earthquake activity, *Tectonics,* vol. 7, no. 3, 663-684, 1988

Bryan, K. A., and T. K. Rockwell, Holocene character of the Helendale fault zone. Lucerne Valley, Sna bernardino County, California, (abstracts with programs) *Geol. Soc. Am.,* 27, pp. 7, 1995.

Bryant, W. A., Eastern North Frontal fault zone, and related faults, southwestern San Bernardino County, *Fault Evaluation Report, FRE 182, CA. Div. Mines Geol.,* 1-20, 1986.

Bull, W. B., Tectonic geomorphology of the Mojave desert, *U. S. Geol. Survey Contract Report,* 14-08-001-G-394, Of. Eqs, Volc., and Eng., Menlo Park, CA, 188 p., 1977.

Cai, J., G. D. McMechan, and M. A. Fisher, Application of ground-penetrating radar to investigation of near-surface fault properties in the San Francisco Bay region, *Bulletin of the Seismological Society of America*. 86, 1459-1470, 1996.

Camelbeeck, T., and M. Meghraoui, Geological and geophysical evidence for large paleoearthquakes with surface faulting in the Roer Graben (northwest Europe), *Geophys. J. Int.,* 132, 347-362, 1998.

Corbeanu, R. M., K. Soegaard, R. B. Szerbiak, J. B. Thurmond, G. A. McMechan, D. Wang, S. Snelgrove, C. B. Forster, and A. Menitove, Detailed internal architecture of a fluvial channel sandstone determined from outcrop, cores, and 3-D ground-penetrating radar: Example from the middle Cretaceous Ferron Sandstone, east-central Utah, *AAPG Bulletin,* vol. 85, no. 9, 1583-1608, 2001.

Chow, J., J. Angelier, J. J. Hua, J. C. Lee, and R. Sun, Paleoseismic event and active faulting: from ground penetrating radar and high-resolution seismic reflection profiles across the Chihshang Fault, eastern Taiwan, *Tectonophysics,* 333, 241-259, 2001.

Davis, J. L., and A. P. Annan, Ground penetrating radar for high-resolution mapping of soil and rock stratigraphy, *Geophys. Prospect*. 37, 531-551, 1989.

Dehls, J. F., O. Olesen, L. Olsen, and L. H. Blikra, Neotectonic faulting in northern Norway; the Stuoragurra and Nordmannvikdalen postglacial faults, *Quaternary Science Reviews*, 19, 1447-1460, 2000.

Dibblee, T. W., Late Quaternary uplift of the San Bernardino Mountains on the San Andreas and related faults, in Crowell, J. C., ed., San Andreas fault in southern

California, *CA Division of Mines and Geology Special Report,* 118, 127-135, 1975.

Dokka, R. K., and Travis, C. J., Late Cenozoic strike-slip faulting in the Mojave desert, California, *Tectonics,* 9, 311-340, 1990.

Dolan, J. F., Sieh, K., Rockwell, T. K., Yeats, R. S., Shaw, J., Suppe, J., Huftile, G. J., and Gath, E. M., Prospects for larger or more frequent earthquakes in the Los Angeles metropolitan region, *Science,* 267, 199-205, 1995.

Du, Y., and A. Aydin, Is the San Andreas big bend responsible for the Landers earthquake and the eastern California shear zone?, *Geology,* vol. 24, no. 3, 219-222, 1996.

England, P., and J. Jackson, Active deformation of the continents, *Ann. Rev. Earth Planet. Sci.,* 17, 197-226, 1989.

Eppes, M. C., L. D. McFadden, J. Matti, and R. Powell, Influence of soil development on the geomorphic evolution of landscapes: An example from the Transverse Ranges of California, *Geology,* vol. 30, no. 3*,* 195-198, 2002.

Fiegl, K. L., Sergent, A., and D. Jacq, Estimation of an earthquake focal mechanism from a satellite radar interferogram: Application to the December 4, 1992 Landers aftershock, *Geophys. Res. Lett.,* 22, 1037-1040, 1995.

Fisher, E., G. A. McMechan, M. R. Gorman, A. P. R. Cooper, C. L. V. Aiken, M. E. Ander, and M. A. Zumberge, Determination of Bedrock Topography Beneath the Greenland Ice Sheet by Three-Dimensional Imaging of Radar Sounding Data, *J. Geophys. Res.,* vol. 94, no. B3, 2874-2882, 1989.

Fisher, E., G. A. McMechan, and A. P. Annan, Acquisition and processing of wide-aperture ground-penetrating radar data, *Geophysics,* vol. 57, no. 3*,* 495-504, 1992.

Fumal, T. E., Pezzopane, S. K., Weldon, R. J., and D. P. Schwartz, A 100-year recurrence interval for the San Andreas fault at Wrightwood, California, *Science,* 259, 199-203, 1993.

Grant, L. B., and K. Sieh, Paleoseismic evidence of clustered earthquakes of the San Andreas fault in the Carrizo Plain, California, *Journal of Geophysical Research,* vol. 99, nao. B4, 6819-6841, 1994.

Hammond, W. R., and K. F. Sprenke, Radar detection of subglacial sulfides, *Geophysics,* vol. 56, no. 6, 870-873, 1991.

Harris, R., and R. Simpson, Changes in static stress on southern California faults after the 1992 Landers earthquake, *Nature,* 360, 251-254, 1992.

Hecker, S., Fumal, T. E., Powers, T. J., Hamilton, J. C., Garvin, C. D., and D. P. Schwartz, Late Pleistocene-Holocene behavior of the Homestead Valley fault segment – 1992 Landers, CA surface rupture, *EOS AGU Fall Supplement*, 612, 1993.

Jackson, J., Fault death: a perspective from actively deforming regions, *Journal of Structural Geology,* 21, 1003-1010, 1999

Jacoby, G. C., Sheppard, P. R., and K. Sieh, Irregular recurrence of large earthquakes along the San Andreas fault: evidence from trees, *Science,* 241, 196-199, 1988.

Jezek, K. C., Radar measurements of borehole geometry on the Greenland and Antarctic ice sheets, *Geophysics,* vol. 50, 242-251, 1985.

Jaume, S., and L. Sykes, Changes in state of stress on the southern San Andreas fault resulting from the California earthquake sequence of April to June, 1992, *Science,* 258, 1325-1328, 1992.

Knight, R. J., and A. Nur, the dielectric constant of sandstones, 60kHz to 4MHz, *Geophysics,* vol. 52, 644-654, 1987.

Li, Y. –G., Henyey, T. L., and P. C. Leary, Seismic reflection constraints on the structure of the crust beneath the San Bernardino Mountains, Transverse Ranges, southern California, *Journal of Geophysical Research,* 97, 8817-8830, 1992.

McCalpin, J. P., Paleoseismology, *Academic Press Inc.,* San Diego, Calif., 588 p., 1996.

May, S. R., and C. A. Repenning, New evidence for the age of the Old Woman sandstone, Mojave Desert, California, in Sadler, P. M., and Kooser, M. A., eds., Late Cenozoic stratigraphy and structure of the San Bernardino Mountains, *Geol. Soc. Amer. Cordilleran Section Meeting Guidebook*, 6, 93-96, 1982.

Meghraoui, M., T. Camelbeeck, K. Vanneste, M. Brondeel, and D. Jongmans, Active faulting and paleoseismology along the Bree fault, lower Rhine graben, Belgium, *J. Geophys. Res.,* vol. 105, no. B6, 13,809-13,841, 2000.

Meisling, K. E., Neotectonics of the north frontal fault system of the San Bernardino Mountains: Cajon Pass to Lucerne Valley, California (Ph.D. thesis), Pasadena, CA, *California Institute of Technology*, 394 pp., 1984.

Meisling, K. E., and R. J. Weldon, Late Cenozoic tectonics of the northwestern San Bernardino Mountains, southern CA, *Geol. Soc. Amer. Bull*., 101, 106-128, 1989.

Miller, F. K., Reverse-fault system bounding the north side of the San Bernardino Mountains, in recent reverse faulting in the Transverse Ranges, California, *U. S. Geol. Surv. Prof. Pap.,* 1339, 83-95, 1987.

Nur, A., Hagai, R., and G. C. Beroza, The nature of the Landers-Mojave earthquake line, *Science,* vol. 261, 201-203, 1993.

Padgett, D. C., and T. K. Rockwell, Paleoseismology of the lenwood fault, san Bernardino County, California, *Mojave Desert: South Coast Geological society annual Fieldtrip Guidebook*, 222-238, 1994.

Peltzer, G., Crampe, F., Hensley, S., and P. Rosen, Transient strain accumulation and fault interaction in the eastern California shear zone, *Geology,* vol. 29, no. 11, 975-978, 2001.

Reynolds, J. M., An Introduction to Applied and Environmental Geophysics, *Reynolds Geo-Sciences Ltd, UK*, 796 pp., 1997.

Rockwell, T. K., Lindvall, s., Herzberg, D., Murbach, D., Dawson, T., and G. Berger, Paleoseismology of the Johnson Valley, Kickapoo, and Homestead Valley faults: clustering of earthquakes in the eastern California shear zone, *Bull. Seism. Soc. Amer.,* 90,1200-1236, 2000.

Rubin, C. M., and K. Sieh, Long dormancy, low slip rate, and similar slip-per-event for the Emerson fault, eastern California shear zone, *Journal of Geophysical Research Letters,* vol. 102, no. B7, 15,319-15,333, 1997.

Rubin, C. M., Systematic underestimation of earthquake magnitudes from large intracontinental reverse faults; historical ruptures break across segment boundaries, *Geology (Boulder),* vol.24, no.11, pp.989-992, 1996.

Rzonca, G. F., and D. W. Clark, Local geology, Kaiser Cement Corporation, Cushenbury facility, Lucerne Valley, California, *Geology and Mineral Wealth of the California Trnasverse Ranges,* South Coastal Geological Society, 676-679, 1982.

Sadler, P. M., Provenance and structure of late Cenozoic sediments in the northeast San Bernardino Mountains, in Cooper, J. D., ed., Geologic excursions in the Transverse Ranges, *Geol. Soc. Amer. Annual Meeting Guidebook,* Fullerton, California, California State University, 83-91, 1982.

Sauber, J., Thatcher, W., Solomon, S. C., and M. Lisowski, M., Geodetic slip rate for the eastern California shear zone and the recurrence time of Mojave desert earthquakes, *Nature,* 367, 264-266, 1994.

Savage, J. C., Lisowski, M., and W. H. Prescott., An apparent shear zone trending north-northwest across the Mojave desert into Owens Valley, eastern California, *Geophysical Research Letters,* vol. 17, no. 12, 2113-2116, 1990.

Schwartz, D. P. and K. J. Coppersmith, Fault behavior and characteristic earthquakes: Examples from the Wasatch and San Andreas fault zones, *J. Geophys. Res.,* 89, 5681-5698, 1984.

Shaw, J. H., and P. M. Shearer, An elusive blind-thrust fault beneath metropolitan Los Angeles, *Science,* 283, 1516-1518, 1999.

Sieh, K., and 19 others, Near-field investigations of the Landers Earthquake Sequence, April to July 1992, *Science,* 260, 171-176, 1993.

Sieh, K. E., M. Stuiver, and D. Brillinger, A more precise chronology of earthquakes produced by the San Andreas fault in Southern California, *J. Geophys. Res*., 94, 603-623, 1989.

Spotila, J. A., Farley, K. A., Yule, J. D., and P. W. Reiners, Near-field transpressive deformation along the San Andreas fault zone in southern California, based on exhumation constrained by (U-Th)/He dating, *Journal of Geophysical Research,* vol. 106, no. B12, 30,909-30,922, 2001.

Spotila, J. A., and K. E. Sieh, Architecture of transpressional thrust faulting in the San Bernardino Mountains, southern California, from deformation of a deeply weathered surface, *Tectonics,* vol. 19, no. 4*,* 589-615, 2000.

Spotila, J. A., and K. B. Anderson, Assessing the behavior and seismic hazard of complex thrust and strike slip faulting along the northern front of the San Bernardino Mountains, Southern California, *Geol. Soc. Amer. Abstracts with Programs,* vol 32, no. 7, p.242, 2000.

Spotila, J. A., Farley, K. A., and K. Sieh, Uplift and erosion of the San Bernardino Mountains, associated with transpression along the San Andreas fault, CA, as constrained by radiogenic helium thermochronometry, *Tectonics,* 17, 360-178, 1998.

Stein, R. S., King, G., and J. Lin, Change in failure stress on the southern San Andreas fault system caused by the 1992 magnitude = 7.4 Landers earthquake, *Science,* 258, 1328-1332, 1992.

Stewart, R. D., and R. R. Unterberger, Seeing through rock salt with radar, *Geophysics,* 41, 123-132, 1976.

Stock, J., and P. Molnar, Uncertainties and implications of the late Cretaceous and Tertiary position of North America relative to the Farallon, Kula, and Pacific plates. *Tectonics,* vol. 7, no. 6, 1339-1384, 1988.

Stuiver, M., INTCAL98 Radiocarbon age calibration, *Radiocarbon,* vol. 40, no. 3, 1041-1083, 1998.

Talma, A.S., and J. C. Vogel, A simplified approach to Calibrating C14 dates, *Radiocarbon,* vol. 35, no. 2, 317-322, 1993.

Weldon, R. J., and K. Sieh, Holocene rate of slip and tentative recurrence interval for large earthquakes on the San Andreas fault, Cajon Pass, southern California, *Geol. Soc. Amer. Bull.,* vol 96, 793-812, 1985.

Wells, D. L., and K. J. Coppersmith, New empirisal relationships among magnitude, rupture length, rupture width, rupture area, and surface displacement, *Bull. Seism. Soc. Amer.,* 84, 379-439, 1995.

Working Group on California Earthquake Probabilities, Seismic hazards in southern California: probable earthquakes, 1994-2024, *Bull. Seism. Soc. Amer.,* 85, 379-439, 1995.

Wyatt, D. E. and T. J. Temples, Ground-penetrating radar detection of small-scale channels, joints and faults in the unconsolidated sediments of the Atlantic Coastal Plain, *Environmental Geology*, 27*,* 219-225, 1996.

Yetton, M. D. and D. C. Nobes, Recent vertical offset and near-surface structure of the Alpine Fault in Westland, New Zealand, from ground penetrating radar profiling. *New Zealand Journal of Geology and Geophysics*. 41, 485-492, 1998.

VITA

Kevin B. Anderson

Work Experience

Geologist- September 2002 to present
ExxonMobil Exploration Company
P.O. Box 4778
Houston, Texas 77210

Education

Master of Science, Geology - August 2000 to August 2002
Virginia Polytechnic Institute and State University
Blacksburg, Virginia

Bachelor of Science, Geology - September 1994 to June 2000
Virginia Polytechnic Institute and State University
Blacksburg, Virginia

Publications

Anderson, K., Investigating the paleoseismic history and complex fault behavior of the Transverse Ranges and the eastern California shear zone, southern California, Dept. of Geological Sciences, Virginia Tech, Blacksburg, VA 24061, Abstracts for GSSRS, 2002.

Anderson, K. and J. Spotila, Investigating complex fault behavior at the intersection of the Transverse Ranges and the eastern California shear zone, southern California, Abstracts for AGU National Meeting, San Francisco, CA, 2001.

Anderson, K., The paleoseismic and neotectonic history of the North Frontal thrust system of the San Bernardino Mountains, southern California, Dept. of Geological Sciences, Virginia Tech, Blacksburg, VA 24061, Abstracts for GSSRS, 2001.

Anderson, K., and J. Spotila, The relationship of geologic structure to the Giles County seismic zone in southwest Virginia, based on fracture mapping in allochthonous Paleozoic strata, Abstracts for GSA Southeast Section Meeting, Raleigh, NC, 2001.

Spotila, J., and K. Anderson, Assessing the behavior and seismic hazard of complex thrust and strike-slip faulting along the northern front of the San Bernardino Mountains, southern California, Abstract for GSA National Meeting 2000, Reno, NV, 2000.